Simulation of polyolefins waste gasification for chemical recycling applications in Aspen Plus

Thesis report

Conrado Zamora Roman

To obtain the degree of Master's Science at the Delft University of Technology

Student number: 5122643

Duration: November 15th, 2020- October 15th, 2021

P&E: 3047

Supervisors:
Dr. ir. Wiebren de Jong
Dr. Hamid Gilvari
Dr. Luis Cutz

List of Acronyms

	Acronyms
BFB	Bubbling Fluidized Bed
CCE	Carbon Conversion Efficiency
CFB	Circulating Fluidized Bed
CFD	Computational Fluid Dynamics
CGE	Cold Gas Efficiency
CSTR	Continuously Stirred Tank Reactor
DFB	Dual Fluidized Bed
dp	Particle Diameter
ER	Equivalence Ratio
FV	Fluidization Velocity
GY	Product Gas Yield
HDPE	High Density Polyethylene
IHBFBSR	Indirectly Heated Bubbling Fluidized Bed Steam Reformer
LDPE	Low Density Polyethylene
LHV	Low Heating Value
MSW	Municipal Solid Waste
MAH	Monoaromatic Hydrocarbon
PAH	Polyaromatic Hydrocarbon
PET	Polyethylene Terephthalate
PFR	Plug Flow Reactor
PP	Polypropylene
PS	Polystyrene
PSD	Particle Size Distribution
PW	Polyolefins Waste
RDF	Refuse Derived Fuel
SF	Steam To Feedstock Ratio
TPM	Two-Phase Model
TY	Tar Yield

Abstract

The Dutch government program " A circular economy in the Netherlands by 2050" prioritizes the 100% recycling of plastics used in the country by 2050 to reduce the consumption of fossil resources and increase the value of the plastic waste, which is currently incinerated or exported in its majority [1]. This objective can be facilitated by including chemical recycling techniques to recover valuable chemicals such as syngas (H_2/CO) and monomers (ethylene/propylene) from plastic waste [2]. Among the chemical recycling techniques, gasification is a mature technology with the highest flexibility on the feedstock composition, allowing to treat complex mixtures as plastic waste [3]. In this framework, the project "Towards improved the circularity of polyolefin-based packaging" evaluates the technology readiness level of gasification for recycling a plastic waste mixture representative of the packaging sector (39.6% of the European plastics demand in 2019 [4]), to increase the knowledge of polyolefins waste (PW) gasification to contribute in closing the plastics loop [5].

The Process and Energy Department of TU Delft is part of this project and is responsible for gasifying a polyolefins waste mixture representative of the packaging sector (PW-DKR350) in a novel Indirectly Heated Bubbling Fluidized Bed Steam Reformer (IHBFBSR) [6]. This thesis focuses on developing a kinetic model of the IHBFBSR, which describes the bed hydrodynamics according to the two-phase theory (TPM) in Aspen plus as a complementary tool for the validation of the experimental work and narrow down the number of laboratory tests by identifying the gasification parameters (temperature, ER and SF ratios) that optimizes the following key performance indicators: carbon conversion efficiency (CCE), cold gas efficiency (CGE), product gas yield (GY) and tar yield (TY).

This document describes the development of the TPM-IHBFBSR model. It starts with a literature review of the most-used modelling approaches for carbonaceous materials. Next, it describes the upgrading strategies applied, according to the equilibrium and kinetic approaches, emphasizing in the hydrodynamic models and simulation settings. Through this part were identified the optimal gasification parameters: 680°C<T<800°C, ER=0.15 and SF=2. Finally, the comparison of the TPM-IHBFBSR model and its previous versions against two validation cases found in the literature, highlights the advantage of having developed an adaptable model to a particular PW mixture, making possible to continue improving it.

Acknowledgements

This work concludes two intense years following the master’s program in mechanical engineering, track energy and process. This experience challenged me since the first day in the academic field and taught me the importance of keeping my beloved ones closed during the pandemic, valuing every moment that I share with them. At the moment, I will be defending this work, our society is getting ready to return to “normality”, whatever we used to call normal, and I will be celebrating ten years since I started my preparation to become a process engineer ready to face it.

I want to thank Wiebren de Jong for giving me the opportunity to work in this project, I always want to participate in a project of social impact, and I cannot find myself in a better field than contributing, since my corner, in mitigating the pollution that we have done to our planet. In his research group, I had the opportunity to collaborate with Hamid and Luis, to excellent researchers and better people, who guided me along the last year in building the work that you will read next, every single word and plot in this document went through their analyses, and I cannot be more than satisfied with the work we have developed for the process simulation field.

I could not have been capable of dedicating me full time to this program without the economic support from the Consejo Nacional de Ciencia y Tecnología (CONACYT) and FUNED. Both institutions believed in my formation to contribute to the development of our country. I will not be capable of retributing the trust until I return to Mexico to apply the knowledge gained in these years.

My family, especially my parents Conrado and Santa, whom I have not seen since the beginning of the program due to the global situation, were the first motivators for this adventure and even in the most challenging moments, they have been there supporting and cheering me up to continue, there are not enough words to thank what they have done for me.

Finally, to my friends, the ones who stayed in Mexico and the new ones that I did along these years, TU Delft made me a better engineer, but it is next to you how I became a better person.

Table of Contents

1 Introduction

“Circular economy in The Netherlands by 2050” is the Dutch program that prioritizes the intelligent management of raw materials (minerals, fossils and metals), products and services. The initiative holds two clear objectives for the next three decades: reducing the consumption of primary raw materials up to 50% by 2030 and efficiently using and re-using raw materials without harmful emissions to the atmosphere by 2050 as Figure 1 shows [1].

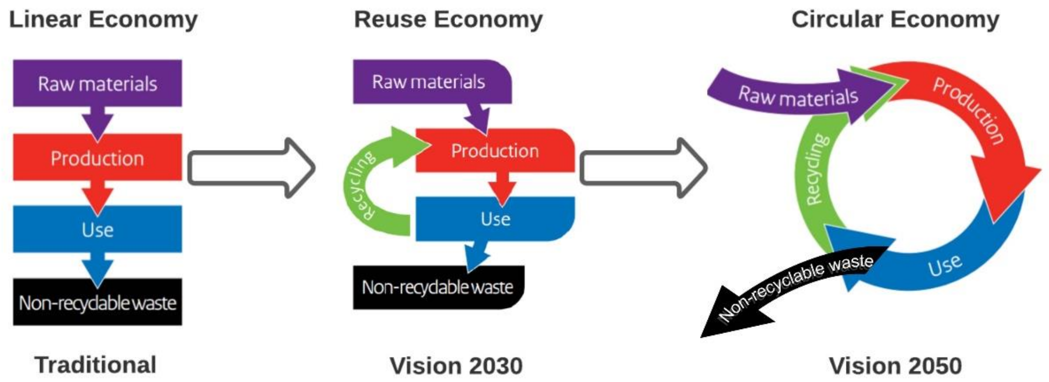

Figure 1. Evolution of economic strategy in the Netherlands from linear to circular model [1].

The circular economy program is divided into five categories: biomass, plastics, manufacturing industry, construction materials and consumer goods [1]. The plastics category is the central theme in this work.

Plastics are an integral part of our lifestyle, though their waste disposal has become one of the challenges of this century. They are fossil-based materials with a long-life duration that usually require elevated temperature and/or pressure conditions to degrade them [1]. The list of alternatives for proper plastic waste disposal is limited; thus, most of the time, they end up incinerated or buried, polluting our soil, air and water. To tackle this situation, exits international and local initiatives such as “Plastics 2030” by Plastics Europe [7], and “From Waste to Resources” by the Dutch Ministry of Infrastructure and Environment [8], which aim to add value to the plastic value chain via recycling or the usage of renewable biobased materials focus on packaging plastics.

In 2018, plastic production in Europe was 61.8 million tons (17% of the total global production) with the packaging industry being the most demanding sector with a share of up to 40% (Figure 2) [4]. The plastics most widely utilized in the packaging industry are the polyolefins high-density polyethylene (HDPE), low-density polyethylene (LDPE), polypropylene (PP), and polystyrene together with polyester and poly (ethylene terephthalate) (PET) [9].

Figure 2. European plastic demand by segment and polymer type in 2018 [4].

Based on this data, the Dutch initiative “Waste to Resources” prioritizes returning plastic packaging waste to its corresponding value chain instead of using them for energy recovery, whilst landfilling is only allowed if there is not a practical use for the waste. The initiative proposes different strategies divided into three stages: recycling, energy recovery, and landfilling to maximize up to 100% of the recycling stage. In 2018, the average percentage of recycled packaging plastic waste was 52% in the Netherlands (10% above the European average) [4].

The recycling stage follows a hierarchical order subdivided into mechanical and chemical recycling techniques. Mechanical recycling is the group of techniques focus on polymers reprocessing without affecting their chemical structure. Separating processes of plastic mixtures refer includes plastic classification and sorting based on particle size and material properties as density, color and dielectric constant. On the other hand, polymer reprocessing includes plastic washing, grinding and finally remelting to separate polymers from additives and contaminants. However, mechanical recycling becomes unaffordable after a few cycles due to collecting and sorting costs. Furthermore, the ratio of recycled versus the quantity of plastics that accomplish the end-user requirements is meager [9].

Chemical recycling is an alternative for complex mixtures of plastic waste that are not suitable for mechanical recycling [2]. This group of recycling techniques convert the polymers into monomers or other valuable chemical compounds (hydrogen, carbon monoxide). There are three chemical recycling techniques: depolymerization, cracking and gasification; being gasification the most suitable for plastic waste due to its flexibility to process the dropouts from the entire recycling procedure as well as the outputs from the other two techniques [9]. Additionally, some knowledge institutions as “The Knowledge Institute for Sustainable Packaging” (KIDV, Dutch acronym) include solvolysis (break down of the polymeric chain on the ether, ester and acid groups from polyesters and polyamides) as part of this group [10].

It is in this context where the project “Towards improved circularity of polyolefin-based packaging” was defined by a consortium of private and knowledge institutions with the aim to make feasible the whole recycling process of packaging polyolefins waste via new sorting technologies and chemical recycling in the Netherlands [5]. Figure 3 shows the different parts of the project where the chemical recycling section (shaded in green) evaluates pyrolysis and gasification technologies to identify the optimal operating conditions according to the feedstock composition to run laboratory and pilot plant tests in the further steps of the project.

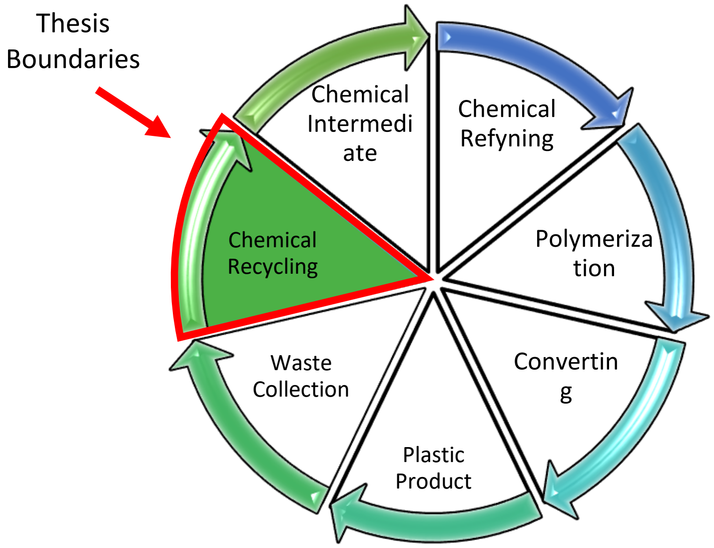

Figure 3. Steps of Circular Plastics Value Chain included in the scope of the project “Towards improved circularity of polyolefin- based packaging. The boundaries of this study are drawn in red [5].

1.1 Problem statement

The project “Towards improved circularity of polyolefin-based packaging” [5] aims to contribute to the targets set on the Dutch program “Circular economy in The Netherlands by 2050” to increase circularity in the plastic industry by 2050. This project recognizes the importance of chemical recycling techniques as gasification of packaging polyolefins waste to close the circle of plastics economy. Currently, there is a knowledge gap related to chemical recycling of polyolefins waste because of the limited number of studies done on plastic waste gasification focusing on varying the operating parameters on the product gas yield.

The main research question of this Thesis is: “which are the optimal operating conditions on polyolefins waste gasification to optimize the following key performance indicators (KPI)?”:

Maximize:

- Carbon Conversion Efficiency (CCE)
- Cold Gas Efficiency (CGE)
- Product Gas Yield (GY)

Minimize:

- Tar Yield (TY)

The main research question is divided in the following sub-questions to address specifically the role of gasification:

1) What is the optimal gasification temperature to maximize the CCE, CGE, and GY with the lowest TY?
2) What is the optimal ratio of the gasifying agents to maximize the CCE, CGE, GY with the lowest TY?
3) What is the optimal particle size diameter and distribution of the feedstock to maximize the CCE, CGE, GY, with the lowest TY?
4) What is the effect of the feedstock composition on the CCE, CGE, GY, and TY?

The results of this work will provide suggestions regarding the optimum operating range for the different gasification parameters of the Indirectly Heated Bubbling Fluidized Bed Steam Reformer (IHBFBSR) according to the polyolefins waste composition. The process simulation results will be used to narrow down the number of required laboratory tests in the experimental part of the project "Towards improved circularity of polyolefin-based packaging".

2 Literature Study

2.1 Gasification principles

Gasification is the combination of several thermochemical process (drying, pyrolysis, homogenous and heterogenous reforming reactions) to convert a carbonaceous material as coal, biomass or plastic waste, known as feedstock in this study, to a mixture of the following components [3]:

- **Product Gas:** Gas phase composed by the following fractions.
    - **Permanent gases:** mixture of carbon monoxide (CO), hydrogen (H_2), carbon dioxide (CO_2), methane (CH_4).
    - **Light Hydrocarbons:** traces of hydrocarbons (C2-C4). This fraction englobes the monomers of two of the major plastics (ethylene and propylene).
    - **Tar:** group of hydrocarbons contaminants heavier than benzene (>C6). The tar compounds are subdivided by their temperature of formation as follows [11]:
        - **Primary tar:** mixed oxygenates. Temperature range: 200-500 °C.
        - **Secondary tar:** mono aromatics hydrocarbons (MAH), heterocyclic ethers. Temperature range: 500-800°C.
        - **Tertiary tar:** polynucleic aromatic hydrocarbons (PAH). Temperature range: 800-1000°C.
    - **Inorganic pollutants:** depending on the feedstock composition, different percentages of hydrogen sulfide (H_2S), hydrogen chloride (HCl), ammonia (NH_3) and hydrogen cyanide (HCN).
- **Char:** solid carbonaceous material.
- **Ashes**: alkali and heavy metals as sodium/potassium and Nickel/Copper/Iron/Magnesium, respectively.

Gasification is mainly an endothermic process classified by the operating temperature range as moderate (800-1000°C) or high (900-1650°C) temperature [12]. The latter temperature range generates product gas with lower CO, H_2 and tar content because of the enhancement of the combustion and tar cracking reactions. Nevertheless, the high temperature promotes the formation of secondary and tertiary tar. Gasification can also be classified in terms of the gasifying agent type: air, oxygen (O_2), carbon dioxide (CO_2), steam (H_2O) or a mixture [13] [14].

The gasification process consists of the following reactions grouped in one of the four stages (Table 1): drying, pyrolysis, and homogenous/heterogeneous reactions. Notice that in the drying stage there is not a chemical reaction as it only describes the moisture remotion from the feedstock.

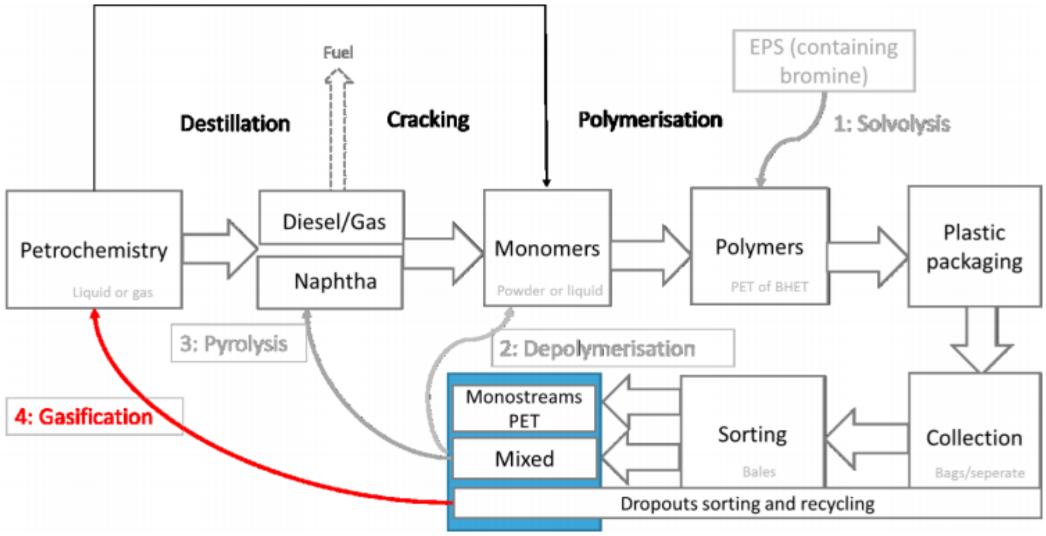

Figure 4. Schematic overview of gasification technique in the chemical recycling process [2].

Table 1. Main plastic waste gasification reactions [15].

Reactions group	**Reactions**	**ΔH (kJ/mol)**	**Description**
Drying (<150°C)	$H_2O\ (liq) \rightarrow H_2O\ (vap)$	41	Moisture Remotion
Pyrolysis (<700°C)	$fuel \rightarrow primary\ tar\ (CH_xO_y)$	-	Initial Devolatization
	$fuel \rightarrow CO, CO_2, CH_4, C_2H_4, H_2O$		
	$fuel \rightarrow C$		
Tar cracking (>700°C)	$primary\ tar \rightarrow secondary\ tar$	-	Primary Tar Cracking
	$primary\ tar \rightarrow CO, CO_2, CH_4, C_2H_4, H_2$		
	$secondary\ tar \rightarrow C, CO, H_2$	-	Secondary Tar Cracking
Homogenous gasification reactions (>700°C)	$H_2 + 0.5\ O_2 \rightarrow H_2O$	-248	H_2 Combustion
	$CO + 0.5\ O_2 \rightarrow CO_2$	-283	CO Combustion
	$CH_4 + H_2O \rightarrow CO + 3\ H_2$	206	Methane Reforming
	$CO + H_2O \rightarrow CO_2 + H_2$	-35	Water Gas Shift
Heterogenous gasification reactions (>700°C)	$C + O_2 \rightarrow CO_2$	-393	Carbon Oxidation
	$C + 0.5\ O_2 \rightarrow CO$	-123	Partial Oxidation
	$C + CO_2 \rightarrow 2\ CO$	171	Boudoard Equilibrium
	$C + H_2O \rightarrow CO + H_2$	136	Steam Reforming
	$C + 2\ H_2 \rightarrow CH_4$	-75	Methanation

The target of the gasification process is to convert the feedstock into a product gas with an elevated LHV (> 15 MJ/Nm^3 for steam gasification) and a low tar concentration (10 g/ Nm^3) [16]. The accomplishment of this target requires a continuous heat supply to the gasifier via autothermal or allothermal processes. The former is the combustion of a feedstock fraction inside the reaction zone, whereas the latter supplies heat from an external source by integrating a heat exchanger or using the bed material as a heat carrier. The allothermal process offers a better control of the heating rate, reducing the risk to increase the content of tertiary tar and char as well as to reduce the feedstock consumption to provide heat [14].

Pressure does not significantly affect the product gas yield as much as the temperature, gasifying agent type or feedstock composition, then most of the gasifiers operate at atmospheric pressure. However, some researchers have found that at pressure above 30 bar, methane and tar content tend to slightly increase, though neither of them is of interest for plastic gasification [14]. Therefore, this review only focuses on gasifiers operating at atmospheric pressure.

The general assessment of the gasifier performance uses the indicators: carbon conversion efficiency (CCE), cold gas efficiency (CGE), product gas yield (GY) and tar yield (TY) [17].

Carbon conversion efficiency quantifies how much carbon from the feedstock is in the product gas, equation (1):

$$CCE = MW * \frac{\sum \nu_i * Yi}{(100 - M\%) * \frac{C_{ad}}{100}} * \frac{F_{gas}}{F_{feed}} * 100 \tag{1}$$

Where:
ν_i = Number of carbon atoms in the organic compound.
Y_i = mol fraction of the organic compound (%).
M%= weight percentage of the moisture in the feedstock determined by the proximate analysis
C_{ad}= carbon content in the feedstock on mass dry basis.
F_{gas} = mol flow at the outlet of the gasifier in mol dry and ash free basis. (kgmol/h)
F_{feed} = mass flow of the feedstock in wet basis (kg/h).
MW = carbon molecular weight (12 kg/ kg mol).

Cold gas efficiency is the energetic ratio of the product gas (free of tar) to the feedstock based on the lower heating value as given in equation (2):

$$CGE = \frac{LHV_{gas}}{LHV_{feed}} * GY * 100 \tag{2}$$

$$LHV_{gas} = \sum LHV_i \, Y_i \tag{3}$$

Where:
LHV_{gas}= in MJ/Nm^3, Normal conditions are 0°C and 1 atm. It does not include the heating value of tar.
LHV_{feed} = low heating value of the feedstock in MJ/kg dry basis.
GY = product gas yield without tar (Nm^3/kg).

The **product gas yield** (equation (4)) indicates how much feedstock converts to any of the gas products instead of char/ashes. The indicator includes the tar fraction while the **tar yield (**equation (5)**)** quantifies the tar content in the product gas [16].

$$GY = \frac{Q_{gas}}{F_{feed}} \tag{4}$$

Where:
Q_{gas} = volumetric flow of product gas (Nm3/h)

$$TY = \frac{F_{tar}}{Q_{gas}} \tag{5}$$

Where:
F_{tar} = mass flow of tar (g/h)

2.1.1 Types of gasifiers

The gasifiers are mainly classified by their hydrodynamic behavior between the gasifying agent(s) and the feedstock as follows:

1) Fixed Bed: updraft, downdraft, horizontal draft.
2) Fluidized Bed: Bubbling (BFB), Circulating (CFB), Dual (DFB).
3) Entrained Flow (EF).

Besides the hydrodynamic regimen, gasifiers can be classified by the operating capacity: small (<10 MW), medium (10 to 100 MW), and large-scale (> 100 MW), respectively [13]. Despite the economic benefits from operating at large-scale [18], the medium-scale FB gasifiers are the more suitable for plastic waste gasification because of the following advantages:

- Fluidized bed gasifiers are more flexible against a varying feedstock composition and particle diameter than the fixed bed or entrained flow gasifiers [19].
- It offers a higher heating rate than the fixed bed gasifiers, assuring complete depolymerization and fast pyrolysis reactions [16].
- Provides enough residence time for tar cracking reactions without operating at high temperature (>1000°C) as an EF gasifier, reducing the risk of ash melting, sand particle attrition and spread the options for the shell material [12].
- Most of the available data in plastic waste gasification at laboratory and pilot scales has been obtained using BFB gasifiers [16].
- The tar content into the product gas in BFB and CFB gasifiers is lower than an updraft gasifier. However, the value can be up to 10 and 100 times higher than in a downdraft and EF gasifier, respectively [12].
- The risk of plastic agglomeration over the gasifier components is low due to the fluidizing velocity compared to fixed bed gasifiers [16].

FB gasifier characterizes by the type of bed material, an active material like dolomite or olivine to enhance tar cracking reactions [20] or an inert material like silica sand or corundum, which provides a uniform temperature distribution [20]. The bed material is well-mixed with the feedstock forming the bed zone continuously blowing up by the gasifying agent [21]. The bed material is well-mixed with the feedstock forming the bed zone under continuous blowing up by the gasifying agent [22]. The bed material properties make the FB gasifier practically insensitive to variations in the feedstock composition as Table 2 shows.

There are two well-known fluidized gasifier types differentiated by the fluidization velocity (FV): Bubbling Fluidized Bed (BFB) and Circulating Fluidized Bed (CFB) described in Figure 5.

Table 2. Relevant characteristics of FB gasifiers for biomass taken from Basu [22].

Parameter	FB Gasifier
Feedstock particle size (mm)	<6
Gas exit temperature (°C)	800-1000
Feedstock composition	Low rank for coal
tolerance	Excellent for biomass
Oxidant requirements	Moderate
Reaction zone temperature (°C)	800-1000
Steam Requirement	Moderate
Nature of ash produced	Dry
CGE (%)	75-90
Application	Medium size units
Problem areas	Carbon conversion

The BFB gasifier has two well-defined zones, the dense bed where drying, first pyrolysis, char gasification and homogenous reactions occur and the freeboard for purely homogenous reactions. The BFB operates at lower fluidization velocity than CFB to mitigate the restricted gas-solid interactions in the dense bed. The BFB gasifier provides a lower CCE (<90%) whilst the CFB reaches values higher than 95% [13]. However, the high FV in the CFB demands the inclusion of a recycling system for char and bed particles which are dragged outside of the gasifier by the product gas. Thus, the CFB requires a static height of bed material, increasing the size and operating complexity of the gasifier [22].

The Dual Fluidized Bed (DFB) gasifier is an alternative configuration developed by TU Wien that combines both models by two interconnected chambers. The gasification chamber provides a high residence time as a BFB, increasing the GY using steam as a gasifying agent, whereas the combustion chamber burns char to supply heat to the gasification section using the solids recirculation at high velocities as the CFB. The main benefits of this configuration are the increase of CCE and reduction of the equipment size in comparison to a CFB [21] [23].

Several updates have been proposed to update the TU Wien gasifier looking forward to increasing the CGE. One of the most known alternatives is the MILENA gasifier by TNO, which inverses the configuration of the combustion and gasification chambers getting a heat flow path inwards the gasification chamber. In this gasifier, the gasification reactions occur throughput the CFB riser, and once that the gasification products reach the top chamber, the solids are separated from the product gas, falling through the annular BFB combustion chamber where they burnt to heat the CFB riser [23].

Another allothermal FB gasifier model is the Indirectly Heated Bubbling Fluidized Bed Gasifier (IHBFBG), known as “Biomass heat pipe reformer” developed by TU Munich [24], (Figure 6a). The heat pipe reformer burns a portion of the feedstock or char in the combustion chamber to circulate steam or flue gas through the pipe to heat the pressurized gasification chamber (5 bar) [25]. The main advantages of the heat pipe reformer are:

- Reduction in the equipment dimensions by exchanging latent heat instead of sensible,
- Higher fluidizing velocity by inverting the configuration of the chambers as in the MILENA model
- Reduced mechanical damage of the equipment by substituting the particle heat carriers with a heating fluid.

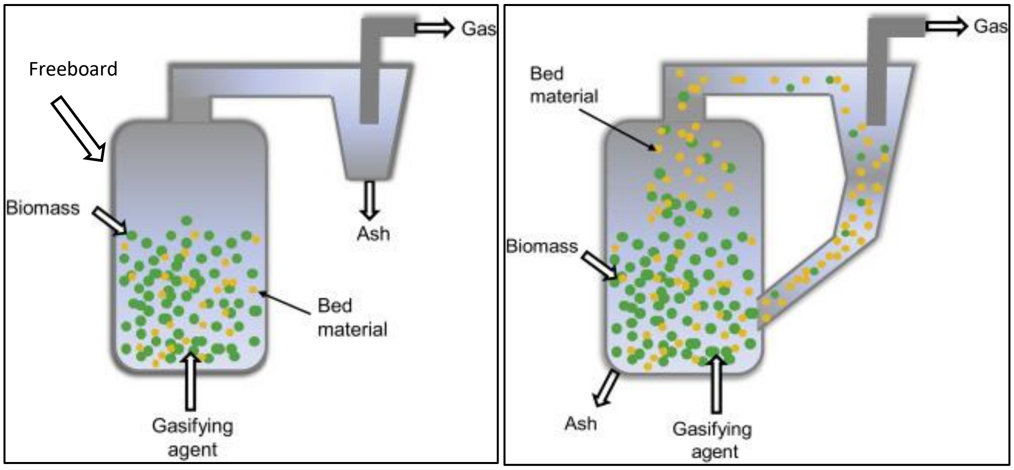

Figure 5. Sketch of a Bubbling Fluidized Bed Gasifier (left) and Circulating Fluidized Bed Gasifier (right) [26].

Lastly, the Indirectly Heated Bubbling Fluidized Bed Steam Reformer (IHBFBSR) at TU Delft is an allothermal model with a similar heat transfer configuration to the Biomass Heat pipe Reformer (Figure 6b). However, this gasifier locates two combustion chambers at the top and bottom of the equipment to supply heat to the gasification chamber at atmospheric pressure. Additionally, the IHBFBSR has an air feeding point for each chamber to increase the temperature and minimize the feedstock consumption in the combustion chambers. The primary air stream enters into the combustion chambers to burn a portion of the feedstock (currently burns natural gas) as an autothermal gasifier; meanwhile, the secondary air stream enters above the bed zone in the gasification chamber to promote the tar cracking reactions [27] [6].

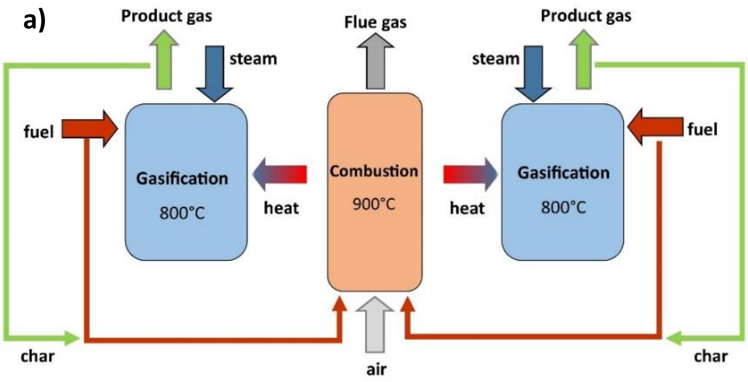

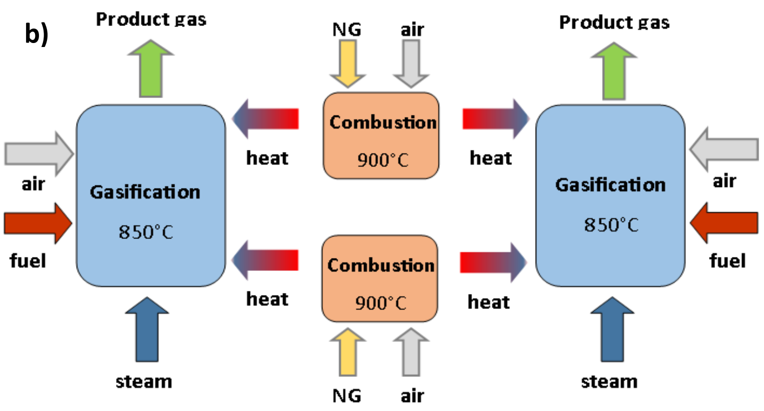

Figure 6. Sketch of the Indirectly heated fluidized bed gasifiers: Biomass heat pipe reformer [25] (a), and the Indirectly Heated Bubbling Fluidized Bed Steam Reformer (IHBFBSR) (b) [63].

2.1.2 Feedstock properties

Plastics, biomass, and coal do not describe a unique material, each of them is a family of carbonaceous compounds with similar composition and heating value classified by the van Krevelen diagram [28]. In this diagram, the polyolefins, plastics of interest in this study, have a high H/C ratio and low O/C ratio appearing at the top left of Figure 7.

The H/C and O/C ratios help to predict the range of the operating parameters. For instance, the high H/C ratio of polyolefins is associated with a low fixed carbon content whilst the volatile content, mainly composed by tar fraction, is elevated, indicating that the operating temperature must be lower than in biomass or coal processes [14]. On the other hand, the low O/C ratio originates from the moisture adhered to plastic samples, narrowing down the type of compounds formed to oxygenates from the primary tar [16]. However, as temperature and residence time increase, the formation of secondary and tertiary tar increase too, then the CGE reduces despite having a high CCE [14].

The polyolefins waste (PW) gasification has not been widely studied, most of the available data comes from studies based on gasifying virgin polyolefins and the comparisons made with biomass and coal. One of the biggest challenges of gasification (including PW) is related to the varying composition of the mixture of the components mixture (HDPE, LDPE, PS, PET, PVC with non-plastics materials as composites, laminates, organics waste) [3] [29].

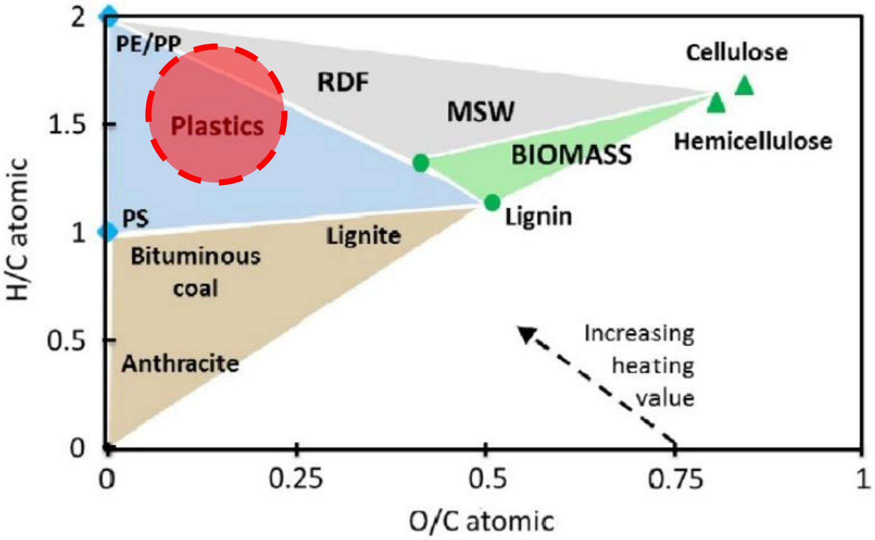

Figure 7. Van Krevelen diagram taken from [30]. The polyolefins waste region is marked by the red circle.

Due to the scarce literature on PW gasification, the findings from co-gasification of virgin polyolefins with other plastics and other carbonaceous materials serve to predict its performance. For instance, Wilk and Hoffbauer [31] studied the steam gasification of different PE mixtures in the presence of olivine, identifying a reduction in the LHV after mixing PE with any of the other polymers. Besides, they got a higher H_2 and CO content in PE+PP and PE+PS mixtures than gasifying virgin PE. Furthermore, they observed essential changes in the distribution of tar compounds between the different PE mixtures. Table 3 gives the composition of the lumped tar compounds from PE mixtures gasification determined by gas chromatography with a mass spectrometer (GCMS) whilst lumped tar compounds from coal or biomass gasification are mainly benzene, phenol, toluene and naphthalene, the lumped tar compounds for PE mixtures are naphthalene and polynucleic aromatic hydrocarbons (PAHs).

Table 3. Lumped tar compounds from steam gasification of PE mixtures taken from [31].

Compound	**PE (100) %w**	**PE+PET (20/80) %w**	**PE+PS (40/60) %w**	**PE+PP (50/50) %w**
Styrene (C_8H_8)	7	9	4	19
Naphthalene ($C_{10}H_8$)	40	26	41	30
Acenaphthylene ($C_{12}H_8$)	15	8	12	11
Anthracene ($C_{14}H_{10}$)	14	19	22	20
Biphenyl ($C_{12}H_{10}$)	3	20	5	2

Moreover, Wilk and Hoffbauer [32] studied the co-gasification of different types of plastic mixtures (virgin PE, recyclate PE, and MSW) with wood pellets (WP) using steam and olivine as the gasifying agent and bed material, respectively. They observed a nonlinear increase of the H_2 and tar content whilst CO and CO_2 content reduces. Also, the tar composition shifted from phenols and furans to naphthalene, anthracene and acenaphthylene. Similarly, Ahmed et al. [33] studied the co-gasification of different polyethylene (PE)-wood chips (WC) ratios using steam as gasifying agent, they got a higher H_2 content in a PE-WC mixture (80/20) than gasifying individually PE or WC, confirming the benefit of gasifying a mixture of different carbonaceous materials over pure biomass or polymer.

Finally, Raj et al. [34] summarize the nonlinear operating benefits related to polyolefins and woody biomass co-gasification, there is a higher H_2 content while the char content reduces in comparison to pure biomass gasification. Meanwhile, the sticky nature of polyolefins is mitigated by adding biomass, reducing the risk of clogging pipelines or the appearance of hot spots inside the gasifier by forming an insulation layer.

In this study, the PW mixture feed to the gasifier, including the major packaging polyolefins (HDPE, LDPE, PP, PS) and their blends, is defined by the international waste management agency Deutsche Gesellschaft für Kunststoff-Recycling (DKR) as "mixed plastics" and classified inside the specification 350 [2] [18].

The DKR 350 specification states the maximum allowed content of some impurities as organic waste or metals, helping to create an overall idea of the polymeric content of the mixture. For instance, Table 4 shows the polymeric composition of the polyolefins waste sample identified in the study done by TNO after applying the criteria of the DKR 350 specification [10].

Moreover, the DKR 350 specification emphasizes on the maximum allowed content of PVC in the mixed plastics due to the corrosive atmosphere propitiated by the chlorine atoms, which are harmful to the process equipment and/or can poison the catalyst used for tar cracking [35]. On the other hand, the PET content specified relates to the PET packaging that did not accomplish previous sorting specifications. However, for PET, its presence is beneficial for the gasification reactions due to its oxygen content serving as an additional source of the gasifying agent, reducing the demand for external O_2 [15].

2.1.3 Particle diameter and particle size distribution

The other two parameters that control the gasification are the particle diameter (dp) and particle size distribution (PSD) of the feedstock and/or bed material, though the latter is considered monodisperse in most of the cases. It is well-known that reducing dp increases the product gas yield because the heat and mass transfer limitations become negligibl~~e~~. However, it has not been possible to go further in the effect of PSD due to the difficulty of effectively measuring the hydrodynamic behavior inside the bed zone [28].

Nowadays, the improvements in computational fluid dynamics (CFD) techniques provide a good insight into the hydrodynamic behavior through the gasifier showing the effect of varying the dp and PSD in the product gas yield. For instance, Zhou et al. [36] studied the effect of enlarging the PSD width of a 3D BFB gasifier model applying the multi-phase particle in cell (MP-PIC) method. They achieved a higher CCE, H2 and CO content inside the bed zone due to the increase of the reaction rates of biomass devolatilization, char steam reforming and Boudoard reactions, then the bed zone is entirely governed by the kinetics describing a more uniform temperature profile along the gasifier as soon as the PSD increases.

Table 4. Adjusted composition after applying the classification criteria in the DKR 350 specification [37] [10].

DKR 350 Specification			
Group	**Plastic waste component** [a)]	**DKR 350 criteria (%w)**	**Composition after applying criteria (%w)** [10]
Plastic 90%	PE film	-	34
	PE bags	-	10
	PP film	-	7
	PET/PVC film	-	2
	PET bottle	<4	4
	PE bottle	-	7
	PP bottle	-	15
	residual plastics [b)]	-	7
	laminates	-	5
Impurities 10%	organic residue [c)]	<3	3
	paper/ carboard	<5	5
	metal/glass	<2	1
	PVC/PS	<0.5	1

Notes:

a) The polymeric composition of each plastic waste component is free of residues. The overall residue content is included in the organic residue category.

b) the composition of the unknown residual plastics stream has been assumed as a uniform distribution of the 5 packaging plastics (HDPE, LDPE, PP, PET, PS).

c) The polymeric composition only considers the most common packaging polymers, any other polymer found in the fraction was put in the residue column together with the organic waste.

Moreover, Du et al. [38] got similar results after varying the PSD width of the biomass particles in the air gasification of woody biomass of a 3D BFB gasifier model applying the MP-PIC method. However, the effects of these parameters have not been verified in experimental works yet.

2.1.4 Gasifying agents

Typically, there are four types of gasifying agent: air, O_2, steam, and CO_2. Each of them has different technical and economic advantages/disadvantages that must be weighted according to the process requirements and feedstock type. Table 5 compares the impact of each gasifying agent in the product gas composition and the LHV. Air is used as the baseline case. The last column includes the main operating characteristics of each gasifying agent.

Air is the most widely studied gasifying agent for gasification because of its availability, notwithstanding its negative impact on the LHV. The air flow required for gasification is calculated by the equivalence ratio (ER) described by equation (6). Several studies for plastic feedstock used ER values in the range of 0.3-0.4 to get a high temperature to enhance the tar cracking reactions without considerably affecting the LHV [16].

$$ER = \frac{\left(A/_F\right)}{\left(A/_F\right)_{sto}} \tag{6}$$

Notes:
$A/F =$ Air to feedstock mass flow ratio (dimensionless)
$(A/F)_{sto}$ =stochiometric air to feedstock mass flow ratio (dimensionless)

The second most studied option is steam because it increases the H_2 content besides the content of methane (CH_4) and ethylene (C_2H_4), the PE monomer, so it is a most attractive option despite the high tar content generated and the elevated operating costs from steam generation [16]. The quantity of steam required is specified by the steam to feedstock mass ratio (S/F) varying from one feedstock to another. For instance, coal gasification requires an S/F between 0.5-1.5, going up to 2 when the ash content is higher. Meanwhile, biomass gasification requires a S/F ratio between 0.3-0.6 because the biomass moisture becomes an extra steam source after the drying stage [25]. In PW gasification, some authors have been using a S/F ratio between 1-2 for laboratory and pilot tests [16]. The S/F ratio must be evaluated carefully for each feedstock because a steam excess reduces the product gas yield.

The PW oxygasification has not yet been widely studied, though the advantages from coal and biomass processing are well-known [28]. The main advantages are getting a higher LHV and a lower tar content than air gasification, though the H_2 content only increases slightly [39]. The O_2 equivalence ratio (OER) is calculated similarly by equation (6), substituting the air flow by the oxygen flow. Currently, the objective is to overcome the technical and economic challenges related to O_2 production.

Lastly, CO_2 is considered a possible substitute for steam as it does not require a high energy supply. However, the only benefit obtained from CO_2 gasification is the increase of CO content due to a higher displacement of the Boudoard equilibrium to the products, although it does not have the same relevance for PW as in coal gasification due to the low content of fixed carbon in the plastic feedstock [14]. As far as the author is concerned there are no experimental results available studying this alternative.

Combining two types of gasifying agents at different ratios has been proposed to overcome the operating constraints from single gasifying agents. The first and most widely studied mixture is the air enrichment with O_2 (air- O_2) , with a O_2 continent between 30-45% [40]. For instance, at 46% O_2 content, the product gas LHV increases from 8 to 9.5 MJ/m^3 [17].

The other two alternative mixtures are air-steam and O_2-steam, the former mixture aims to increase CCE and H_2 content against the CO, CH_4, and tar content which decreases due to combustion reactions. The latter mixture combines the benefits of getting a higher temperature due to the high O_2 content and the increase of H_2, C_2H_6, and C_2H_4 content and a higher LHV than the steam gasification. For instance, Meng et al [40] studied the variations in the product gas composition from gasifying sawdust with the three mixtures, they found that the highest H_2 yield is obtained using the O_2-steam mixture followed by air- steam and air-O_2. On the contrary, the highest CO yield was achieved using the air-O_2 mixture followed by O_2-steam and air- steam. Weighting these results, the highest LHV and H_2/CO ratio was obtained using the O_2-steam mixture, although it is the most energetic demanding option.

Table 5. Gasifying agent overview.

Gasifying agent	H_2 yield	CO yield	Tar yield	LHV (MJ/Nm3)	Operating characteristics
Air [16]	Reference	Reference	Reference	Lowest by N_2 dilution (4-6)	• High gasification temperature • Cheapest option • Widely studied in different feedstock types and mixtures
O_2 [40]	Increase	Increase	Lower	Higher (12-13)	• Increases the gasification temperature • Reduces air preheating services • Pure O_2 production is costly and highly energy demanding (cryogenic separation or electrolysis at high pressure). • Suitable for large-scale plant
Steam [25]	Increase	Decrease	Increase	Highest (15-20)	• Decrease CH_4 and heavier hydrocarbons content • Suitable for medium and large-scale plants. • Highly energy intensive, compensated by energy recovery from product gas cooling. • Increases CO_2 content
CO_2 [14]	Decrease	Increase	Not data	Not data	• Suitable for feedstock with high carbon fixed content.

2.1.5 Bed material

Independently of the gasifier model, the bed material selection is based on increasing the CGE either by its thermal or catalytic properties. The CGE can be improved by selecting a bed material with high thermal conductivity. Also, the bed material can provide more active sites for tar cracking reactions or purifying the product gas from impurities as H_2S or NH_3 [41]. Typically, the bed material particles are grouped in four categories in function of their hydrodynamic properties and diameter as follows:

- **Group A**: aeratable particles to provide catalytic sites for tar cracking without allowing bubble formation (dp: 30-100 µm) [42].
- **Group B**: Sand-like particles as heat carriers and promote bubble formation (dp: 100-1000 µm) [42].
- **Group C**: Fine powder material that is non-fluidizable, usually get stacked at the bottom of the gasifier producing fouling troubles (dp <30 µm) [42].
- **Group D**: Dense or large particles that require of high fluidizing velocity (dp> 1000 µm) [42].

The best option for fluidized bed systems belong to group B, being the silica-sand the best option due to its high thermal conductivity and rapid accessibility, while the selection of active particles depends on the feedstock composition, gasifying agent(s) and the end-user specifications of the product gas.

Besides, Group A particles are mostly used in fixed-bed reformers downstream the gasifier and the Groups C includes fine particles that tend to be stuck in the gasifier causing frequent shutdowns [21].

The main challenge in PW gasification is the reduction of tar content in the product gas, then the list of suitable active particles narrows down to the options that decrease the tar content whilst the H_2 content increases.

Dolomite is the most suitable option for tar cracking whether it is used in situ or downstream the gasifier because it can eliminate the tar compounds at high content of calcium oxide (CaO) and magnesium oxide (MgO). However, the dolomite particles suffer attrition and deactivation by coke formation affecting its performance, arising the necessity to find materials with higher mechanical properties and promotes char gasification to avoid the formation of coke deposits [43].

The first substitute for dolomite studied was olivine which has better attrition resistance. Also, the iron atoms onto the surface enhance the catalytic tar cracking reactions and the WGS reaction increasing the H_2 content [44]. Other alternatives with high mechanical resistance are inert Al-based materials such as zeolites and alumina, the zeolites are materials made of aluminosilicates with wide porosity that can be dopped by different active metals as nickel (Ni), iron (Fe) and/or yttrium (Y) to promote tar cracking reactions as well as alkaline metals to enhance char gasification [45].

Meanwhile, the alumina family englobes materials with a high surface area available for deposition of active metals as Ni and a high resistance to thermal oxidation, being corundum (α-Al_2O_3) the most stable configuration [46]. Table 6 summarizes the advantages and disadvantages of the most studied bed materials to increase the content of H_2 and CO using silica sand as reference.

Table 6. Active bed material characteristics.

Property	**Dolomite** [43]	**Olivine** [47]	**Zeolite** [45]	**Alumina** [46], [48]
Advantages	• Least expensive material. • Most popular option for tar elimination (>95% when is calcinated)	• Higher iron oxide content increases tar elimination. • Higher attrition resistance. • Less susceptible to deactivation by coke formation. • Calcination increases activity though is lower than calcinated dolomite	• Disperse pore diameter to enhance cracking reactions of large hydrocarbons chains (primary tar) or MAH (secondary tar). • Low CO_2 content in the product gas • Increase of the LHV	• High mechanical strength • High surface area (mesoporous alumina has a surface area of 307 m2/g). • Highest resistance to thermal oxidation, corundum (α-Al_2O_3) has the highest value.
H_2 yield	• The highest H_2 content among the other active materials	• Lower than silica sand	• Higher than silica sand and olivine but lower than dolomite.	• Lower than dolomite and olivine.
Gasifying agent	• Steam • Air-steam	• Air • Steam	• Air • Steam (ZSM-5)	• Air • Steam
Main active component(s)	• CaO, MgO, CO_2	• MgO, Fe_2O_3	• Na, Y	• Dopped metals: Ni, Fe, Pt, Pd
Drawbacks	• After the first cycle, the calcinated material reduces considerably its activity. • Susceptible to attrition. • Small particles suffer elutriation. • Sites deactivation by coke formation at low temperature and S/F ratio.	• Higher oxygen transport due to iron atoms increasing the H_2 and CO consumption.	• Requires steam to increase the H_2 content • Sites deactivation by coke formation at low temperature and S/F ratio.	• It requires the impregnation of metals to have catalytic properties. • Corundum has a lower surface area than other Alumina materials (10 m^2/g). • Lower reforming properties than dolomite • Vulnerable to poisoning and deactivation by coke formation.

2.2 Gasification modelling in Aspen plus

Nowadays, Aspen plus is the most reliable simulator to describe rating and design problems. The software can describe multiphase systems and includes a large database of transport and thermodynamic properties [49]. It is a computational tool capable to solve numerically the coupled equations of mass, energy, thermodynamic equilibrium, and reaction rates, either in a sequential modular or equation-oriented approach. Despite these qualities, its application on simulating gasification systems has just started to increase in the last decade due to the opportunity to quickly evaluate the main gasification parameters (temperature, gasifying agent ratios and residence time) to optimize the process [50].

2.2.1 Equilibrium modelling

The equilibrium model is the simplest option, assuming the system has reached the equilibrium composition. There are four eligible reactor blocks for this model that differentiate by their stoichiometry approach [51]. The main characteristics of the reactor blocks are described in Appendix Table 28.

If no stoichiometry is specified, the RGibbs block provides the simplest way to run sensitivity analyses of the operating parameters [52] [53]. However, most of the works using this block discard the formation of tar compounds because of the restrictions imposed by the same calculation approach, giving an incorrect composition of the product gas [50]. The strategy followed in these studies divides the gasifier into three blocks. For instance, modelling the gasification of LDPE described in Figure 8, the gasifier was decomposed in three blocks where the drying stage was simulated using an adiabatic RStoic block, the drying temperature is calculated in function of the desired final moisture content. Next, the pyrolysis stage was simulated by a RYield block, assuming the spontaneous decomposition of the NC feedstock into its elemental composition. The elemental composition of the feedstock is given by the ultimate analysis (C, H, O, N, S, ash). Finally, the RGibbs block calculates the equilibrium composition of all the species by minimizing the Gibbs free energy [51].

Generally, the equilibrium model makes the following assumptions [54]:

- Gasification occurs at steady-state conditions.
- Solid phase is only composed of graphite and ashes.
- The product gas is mainly composed of H_2, CO, CO_2, CH_4 and H_2O.
- Ashes are modelled as a nonconventional component, so they do not participate in any reaction.
- The pyrolysis and gasifier blocks are isothermal.
- The hydrodynamic behavior inside the reactor is not considered.
- The formation of tar is not considered.

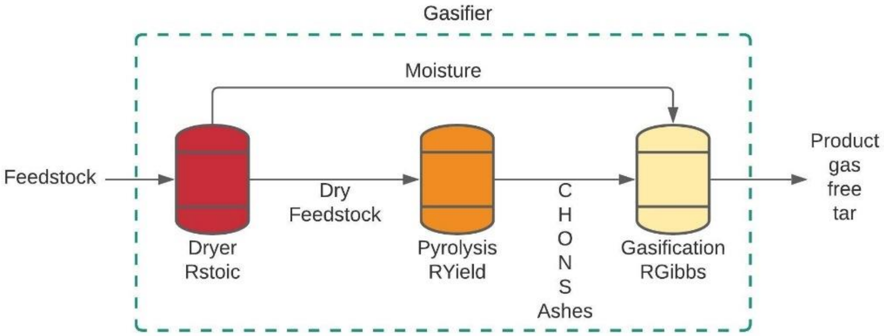

Figure 8. Diagram of a gasifier divided in three-stages using the equilibrium model approach [50].

However, those assumptions have significant drawbacks:

- Due to the absence of tar compounds, it is not possible to specify the configuration of the syngas cleaning train downstream [55].
- The model underestimates the pyrolysis step getting an inaccurate composition of volatiles and char content at the outlet of the system [38].
- Rely on the proximate and ultimate data limits the flexibility of the model to a specific range of feedstock composition [53] [50]
- If only the equilibrium composition is calculated, it is impossible to optimize the product gas composition considering that at lower residence time, the H_2 and CO content are higher whilst the tar content goes down. Also, it is not possible to determine the gasifier dimensions [52].

To overcome these disadvantages, some works [53] [55] [56] include tar formation by specifying the final composition of lumped compounds as toluene, benzene, phenol, and naphthalene, getting a product gas composition close to experimental data. However, it is necessary to have a model capable of calculating the non-equilibrium compositions.

2.2.2 Quasi-equilibrium modeling

This semi-empirical approach considers that the gasifier cannot reach the equilibrium conditions, achieving a product gas composition closer to the experimental data. As in the equilibrium model, the gasifier is decomposed in three reaction blocks (Figure 8) though the RGibbs block applies a temperature lower than the equilibrium temperature [57]. The new temperature is determined after analyzing which gasification reactions cannot reach the equilibrium conditions inside a specific temperature range. For instance, Ngo et al [58] developed a series of empirical expressions to determine the "non-equilibrium factors" of the water gas shift (WGS), steam gasification, Boudoard and methane reactions in function of the gasification temperature, these factors helped to correct the discrepancies of the product gas composition determined by the equilibrium model.

In Aspen plus, the quasi-equilibrium models are quickly developed, enabling the predefined RGibbs block the calculation "option restricted equilibrium approach" (REA). The only requirement is to specify a "degree of approach" (difference between the equilibrium temperature and the "proposed" temperature) for the entire system or per reaction. However, the number of studies applying this modelling approach is limited due to the iterative procedure needed to find the best temperature approach that fits the experimental data [59].

2.2.3 Kinetic modelling

The kinetic model is a more rigorous approach to evaluate or design a gasifier. This modelling considers the reaction rate equations and the residence time as design parameters. The homogeneous gasification reactions follow a power law defined by the Arrhenius expression, equations (7)-(8), where the kinetic constant is calculated by two parameters: pre-exponential factor (ko) and energy of activation (Ea). The kinetic parameters of the homogeneous gasification reactions are given in the Appendix Table 31.

$$r_i = k[A]^{\alpha}[B]^{\beta} \tag{7}$$

$$k = ko * exp\left(\frac{-Ea}{RT}\right) \tag{8}$$

However, the kinetics of the pyrolysis, char gasification and tar reduction reactions is described by more complex expressions. Firstly, the kinetic models for pyrolysis must include the effect of the dp and PSD in the reaction mechanisms, though they are not frequently considered in fluidized systems due to the lack of a trustful rate expression. The pyrolysis rates vary considerably between feedstock types. For instance, coal pyrolysis is up to 10 times faster than woody biomass, and the rate goes up with the increase of moisture and aromatics content, making it impossible to extrapolate data from one feedstock to another [60].

In the case of PW pyrolysis, characterized by the random chain scissoring reaction, it can be modelled by a first-order Arrhenius expression, equation (9), where the kinetic constant Kpy and the carbon fraction Xc must be determined experimentally for each case [56].

$$fuel \overset{k_{py}}{\rightarrow} X_c volatiles + (1 - X_c) char \tag{9}$$

For char gasification, it is reasonable to apply a power law equation to describe it due to the low char formation in PW compared to coal and biomass (<5% weight) [56]. The kinetic parameters for char gasification reactions are included in Appendix Table 32.

On the contrary, for tar is not advisable to include an Arrhenius expression for all the possible compounds as its composition varies from one feedstock to another, increasing the computing time exponentially. The most common strategy is including the kinetic expressions of lumped tar compounds [55]. The kinetic parameters of the lumped tar compounds considered in this study are given in Appendix Table 33.

In Aspen Plus, the kinetic model is defined by the addition/substitution of the RGibbs block in Figure 8 by any of the two kinetic blocks predefined in Aspen plus: continuous stirred tank reactor (CSTR) and plug flow reactor (PFR). Ahmed et al [52] reviewed different simulation works applying the kinetic modelling approach, they noticed a tendency for separating the bed and freeboard zones in two different types of reactor, while a CSTR is used to model the reactions in the bed zone and the RGibbs describes the freeboard zone (See Figure 9). In other works, the RGibbs block for the homogenous reactions in the freeboard was substituted by a series of CSTRs or a PFR [61] [62] [38].

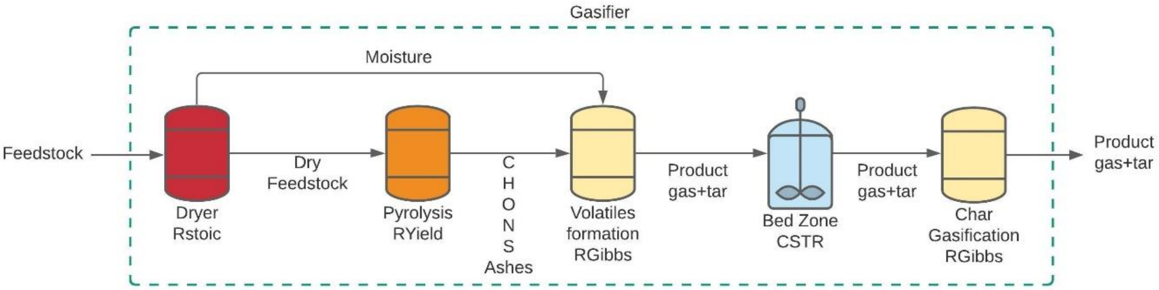

Figure 9. Diagram of the kinetic model to include tar cracking and char gasification reactions [63].

The application of the kinetic blocks allows the monitoring of the tar yield through the gasifier. It is essential to highlight the importance of the lumped tar compounds selected, an incorrect choice can lead to underestimating of the thermodynamic properties. For instance, the dew point of a modeled tar mixture without considering heavy tar compounds has a lower value than the experimental value; eventually, this lower dew point will affect the design of the gas cleaning equipment downstream [52].

The usual strategy to upgrade either the quasi-equilibrium or kinetic models is coupling Fortran subroutines to the simulation. These subroutines are oriented to solve a specific set of equations/instructions separately, to later feed the results into the gasifier model [55]. For instance, Abdelouahed et al. [53] simulated biomass gasification in the TU Wien DFB gasifier using two Fortran subroutines to calculate the gasification products (Figure 10). The first subroutine was coupled to the RYield block, including the pyrolysis correlations and kinetic expressions for char gasification. The pyrolysis correlations decompose the feedstock into gases, tar and char, instead of assuming the elemental decomposition of the feedstock. The second subroutine decomposes the unreacted char into constitutive elements using its ultimate analysis data to model the combustion reactions in a RStoic block. Finally, the freeboard zone is modelled using a PFR block, getting a product gas yield and tar yield in agreement with the operating data.

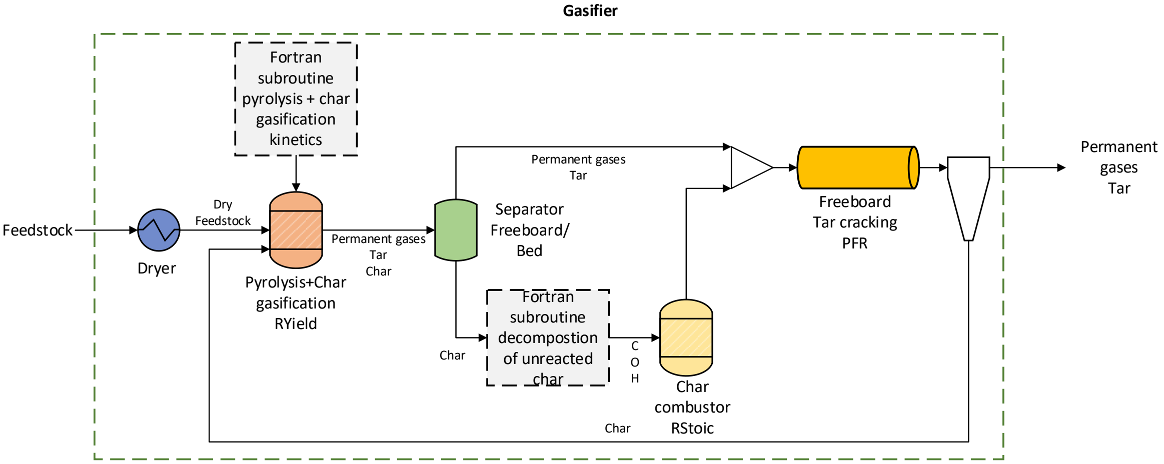

Figure 10. Diagram of the kinetic model including Fortran subroutines to calculate pyrolysis products-char gasification and to calculate the combustion reactions [53].

2.2.4 Hydrodynamic modeling

A robust kinetic model requires the inclusion of the hydrodynamic behavior of the bed and freeboard zones. A detailed description of the fluidized bed hydrodynamics is a complicated task that requires the application of computational fluid dynamics (CFD) techniques distinguished by their calculation approach to solving the momentum, energy and mass equations of the gas and solid phases: Eulerian-Eulerian framework for continuous phases and Eulerian-Lagrangian framework for tracking the solid particles [56].

However, there are few models based on semi-empirical correlations as a good alternative to describe the bed hydrodynamics. These models have been mainly developed for BFB gasifiers assuming that the freeboard is free of solids, operating at a steady-state and without radial dispersion, the most widely used is the two-phase model (TPM), which divides the bed zone into two phases, the emulsion at minimum fluidization conditions is a well-mixed solid-gas system, while the excess gas forms bubbles of constant diameter with a negligible presence of solids, also the bubble phase describes a plug flow through the bed and keeps a continuous exchange of heat and mass with the emulsion phase [56].

The classical two-phase model proposed by Toomey and Johnstone [64] in 1952 has been subjected of modifications regarding the geometry and operating conditions of the gasifier, the most important corrections are a higher fluidization conditions of the emulsion phase than the minimum fluidization, varying diameter of the bubbles along the bed and the presence of solids in the bubble phase [56] [65].

Usually, the correlations of the two-phase model are integrated in Aspen plus with a Fortran subroutine. For instance, Rafati et al. [66] developed a BFB gasifier model dividing the bed zone into several sections of CSTR-PFR pairs for the emulsion and bubble phase, respectively. The freeboard zone was modeled by a PFR block as in other works [38]. The user model determines the flow for each phase solving simultaneously a pair of emulsion and bubbling blocks together with correlations for the bed hydrodynamics and mass transfer between phases, Figure 11.

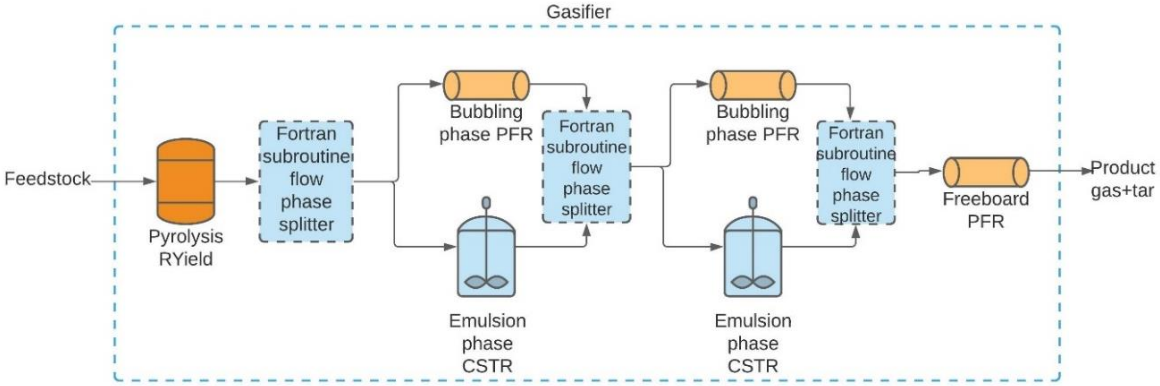

Figure 11. Diagram of the kinetic model including the two-phase model to describe the bed hydrodynamics [66].

3 Methodology

This chapter describes the methodology used to develop a detailed model for the gasification of a PW mixture according to the DKR350 specification (PW-DKR350) in Aspen plus. The model will be an auxiliary tool to evaluate the most important operating parameters (temperature, gasifying agent flow and ratio) to reduce the experimental work in the future (Figure 12). The IHBFBSR model must be aligned with the requirements from the project: increase the value of the indicators CGE/CCE/GY whilst the TY is minimized. Due to the absence of experimental data about the gasification of the PW-DKR350 mixture, the model will be developed based on the results from previous experiences using the IHBFBSR for biomass gasification together with the Literature Study findings related to the gasification principles and modelling approaches.

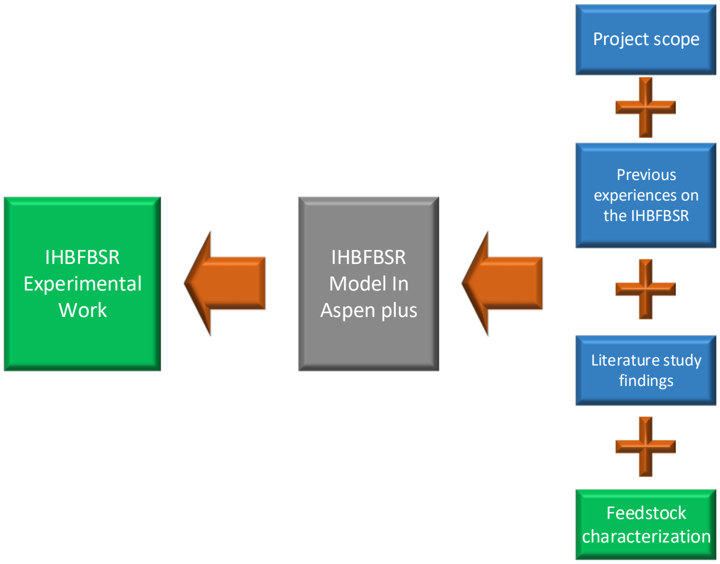

Figure 12. Methodology followed to develop the IHBFBSR model.

The strategy followed in the coming sections includes the Literature Study findings to determine a series of specifications and assumptions to develop the IHBFBSR model; meanwhile, the characterization of the feedstock and the data from previous experiences on the IHBFBSR serves to propose the baseline case.

The general specifications to determine the IHBFBSR model are:

- Thermodynamic state: isothermal.
- Transport phenomena: only at the bed zone.
- Temporal dimension: steady
- Spatial dimensions:
  - Zero dimension: solve the mass and energy balances of the whole system.
  - One dimension: solve the homogenous and heterogenous reactions.
  - Two dimensions: simplified by semi-empirical correlations to solve the bed hydrodynamics.
- Solution method:
  - Semi-empirical: application of semi-empirical correlations to calculate pyrolysis compositions and describe the bed hydrodynamics.

- Numerical: iterative solution of the mass, energy, equilibrium, transport and reaction rates equations following the sequential modular approach.

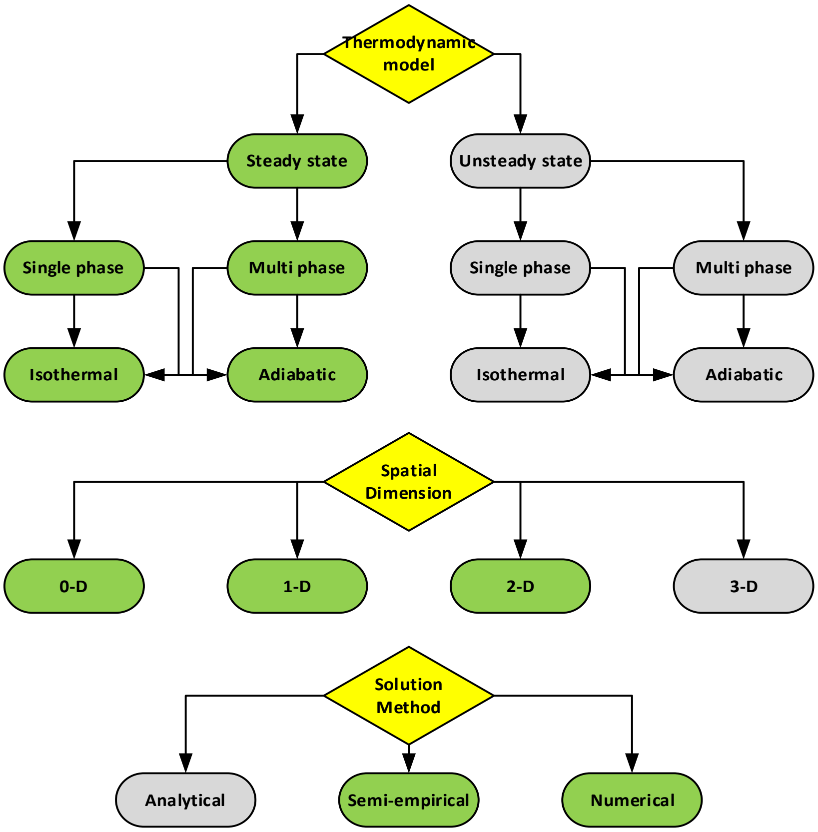

Figure 13. Criteria for the specifications of the modeling approach. The blocks in green refer to the general specifications included in the model [49].

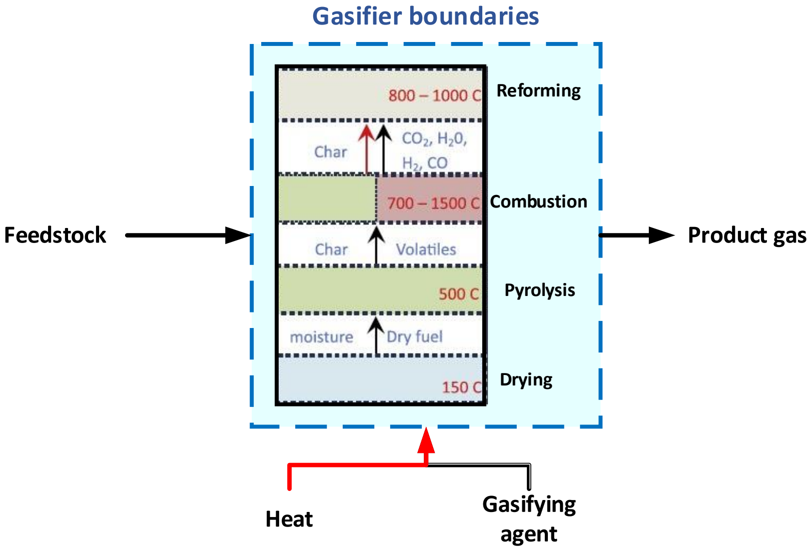

Figure 14. Boundaries of the study.

The summary of the modelling specifications is shown in Figure 13. Next, the boundaries of this study delimited in the Introduction chapter (Figure 3) are drawn in Figure 14 to identify the different inputs and outputs of the IHBFBSR model.

3.1 Implementation of the IHBFBSR model

Before running a simulation in Aspen plus, it is necessary to select a suitable thermodynamic package to calculate the properties of the compounds and specify the modelling approach. The feedstock is modelled as a nonconventional compound (NC); thus, it does not participate in thermodynamic equilibrium calculations. The NC is described by the component attributes enthalpy and density, needing to feed the composition data from the proximate, ultimate and sulfur analyses in the nonconventional models HCOALGEN and DCOALIGT, respectively [50]. Whereas the thermodynamic properties of the conventional compounds are calculated using a cubic equation of state, the Soave-Redlich-Kwong with the Boston Mathias correction for the acentric factor (SRK-BM) is the most used option in gasification simulations [53]. Whereas the thermodynamic properties of the conventional compounds are calculated using a cubic equation of state, the Soave-Redlich-Kwong with the Boston Mathias correction for the acentric factor (SRK-BM) is the most used option in gasification simulations [54] [62] [66]. Finally, the water-steam properties are taken from steam tables [67].

Afterward, the following assumptions and general specifications are applied to develop the IHBFBSR model:

1. The feedstock is described as a NC compound in Aspen Plus using the data from the proximate and ultimate analyses. The enthalpy and density models set as HCOALGEN and DNSTYGEN, respectively. For the HCOALGEN model was enabled the option to specify the High Heating Value (HHV) of the feedstock using the Channiwala correlation [68] which considers the effect of the ashes in the enthalpy of the solids, equation (10).

Table 7. Proximate and ultimate analysis of the PW-DKR350 mixture.

Proximate Analysis Wet Basis (%)				**Ultimate Analysis Dry Basis (%)**							**HHV (MJ/kg)**	**LHV (MJ/kg)**
Moisture	**Fixed Carbon[a]**	**Volatile Matter**	**Ash**	**Ash**	**C**	**H**	**N**	**Cl**	**S**	**O**		
0.38	8.97	84.56	6.09	6.11	74.17	11.27	0.38	0.00	0.00	8.07	38.20	38.06

a) The fixed carbon is determined by difference.

$$HHV\ (MJ/kg) = 0.3491C\ 1.1783H + 0.1005S - 0.1034O - 0.0151N - 0.0211A \tag{10}$$

2. The product gas composition includes the following compounds:

Permanent Gases
- Hydrogen (H_2)
- Carbon Dioxide (CO_2)
- Carbon monoxide (CO)
- Methane (CH_4)

Light Hydrocarbons
- Ethane (C_2H_6)
- Ethylene (C_2H_4)
- Propane (C_3H_8)
- Propylene (C_3H_6)
- C4 and C5 compounds

Others
- Steam (H_2O)
- Inorganic impurities
- Lumped tar.

3. The selection process of the following lumped tar compounds is given below in section 3.1.4:

Single Ring	**Double Ring**	**Triple Ring**
• Benzene (C_6H_6)	• Naphthalene ($C_{10}H_8$)	• Acenaphthylene ($C_{12}H_8$)
• Toluene (C_7H_8)		• Anthracene ($C_{14}H_{10}$)
• Styrene (C_8H_8)		

4. The inorganic impurities are set as inert compounds and are the following:
   - Hydrogen Chloride (HCl)
   - Hydrogen Sulfide (H_2S)
   - Ammonia (NH_3)

5. The char is assumed to be only composed by graphite, being modelled as a conventional solid.

6. The ashes are specified as a nonconventional compound.

7. The pyrolysis step is always fast and completed.

8. The bed material is corundum, an inert material with good thermal conductivity and high resistance to attrition, its main characteristics are shown in Table 6.

Following the findings of the Literature Study, the IHBFBSR is decomposed by subprocesses: drying, pyrolysis, homogenous/heterogenous reactions. Later, the IHBFBSR model will be sequentially upgraded, going from an equilibrium model to a kinetic model including the bed hydrodynamics according to the two-phase theory.

Table 8. Summary of the strategies followed to upgrade the IHBFBSR model.

Strategy	**Drying**	**Pyrolysis**	**Homogenous/Heterogeneous reactions**
I	• Stochiometric process	• Elemental decomposition	• Gibbs free energy minimization • Restricted Equilibrium Approach
II	• Stochiometric process • including PSD	• Elemental decomposition • including PSD	• Gibbs free energy minimization • Restricted Equilibrium Approach • including PSD
III	• Stochiometric process • including PSD	• Mass yield correlations • including PSD	• Gibbs free energy minimization • Restricted Equilibrium Approach • including PSD
IV	• Stochiometric process • including PSD	• Mass yield correlations • including PSD	• Kinetic blocks. • Bed hydrodynamics. • including PSD
V	• Stochiometric process • including PSD	• Mass yield correlations • including PSD	• Kinetic blocks. • Two-phase model • including PSD

After implementing each upgrading strategy in the IHBFBSR model, the changes in the indicators (CGE, CCE, GY and TY) will be analyzed by running sensitivity analyses over the baseline case (Table

9) [27]. Additionally, the yield of the permanent gases (H_2, CO, CO_2 and CH_4) are included as auxiliar indicators.

Table 9. Baseline Process conditions at ER= 0.2.

Parameter	Fuel	Process air	Steam	Nitrogen	Product Gas
Pressure (bar)	1	7	4	11	0.6
Temperature (°C)	25	20	100	20	850
Flow (kg/h)	10	26	10.5	5	25

The varying operating parameters and their respective ranges are:

- Gasification temperature: in the range 500-850°C. The range will be verified by the equilibrium approach model.
- Equivalence ratio (ER): in the range 0.1-0.4. The range will be verified by the equilibrium approach model.
- Steam to fuel ratio (S/F): in the range 1-2. The range will be verified by the equilibrium approach model.

Now, the individual settings for each upgrading strategy to the IHBFBSR model are described in the following subsections

3.1.1 Equilibrium approach

The baseline case applies the equilibrium approach dividing the gasification process into three main blocks: DRYER, PYRO and GASIFIER. The interconnection between blocks is made using the stream class MIXCINC, which includes conventional and nonconventional solids without PSD. The description of the Aspen plus blocks included in the process flow diagram of the equilibrium approach in Figure 15 is given in Table 10.

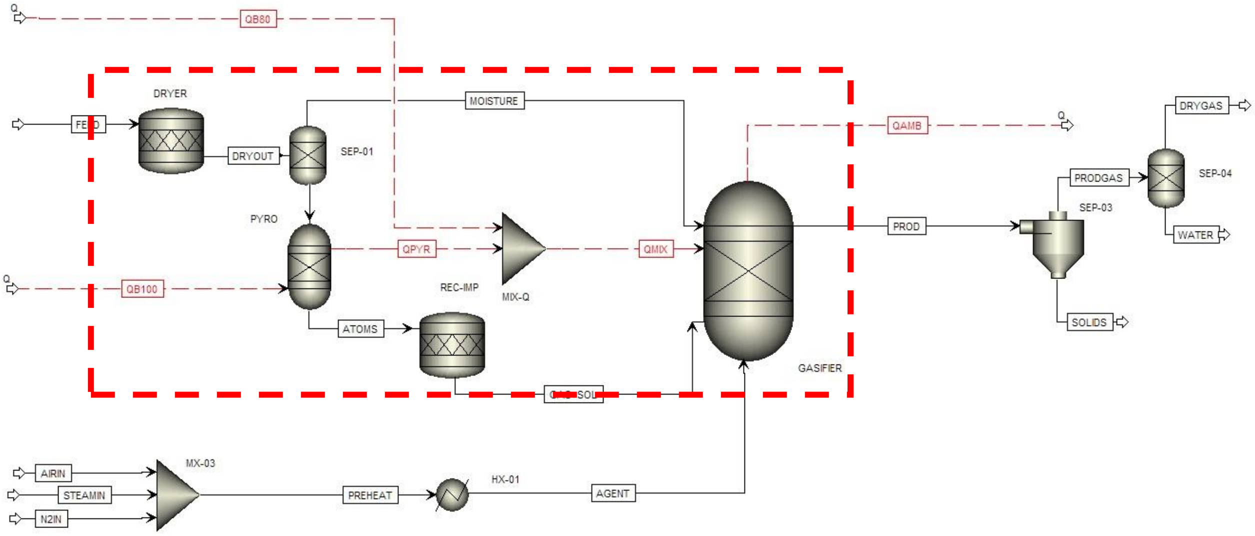

Figure 15. Process Flow Diagram Equilibrium approach. The boundary limits of the real IHBFBSR are drawn by the red dotted line.

Table 10. Description of the Aspen plus blocks used in the equilibrium approach.

Name	Aspen Block	Function	Notes
DRYER	RStoic	Evaporates water by coupling a calculator block with the desired moisture content at the outlet of the Dryer block.	Adiabatic model
PYRO	RYield	Decomposition of nonconventional compound in: • Elements + ashes • Permanent gases + light hydrocarbons + tar + char + ashes	• Isothermal model • Values from the Proximate and Ultimate analysis. • Applying the pyrolysis correlation developed as part of this study.
Rec-Imp	RStoic	Conversion of inorganic elements inside the NC compound into inorganic compounds.	
GASIFIER	RGibbs	Calculate products composition by minimization of Gibbs free energy.	• Isothermal model. • Applies the restricted chemical equilibrium method.
SEP-01	SSplit	Separates the moisture evaporated in the Dryer block from the feedstock stream.	
SEP-03	SSplit	Separates solids from the product gas stream as an ideal cyclone.	
SEP-04	Separator	Separates STEAM from the rest of the product gas stream.	Ideal separation for dry gas calculations.
MIX-Q	Mixer	Combines the heat streams QB80 and QPYR to supply heat to the IHBFBSR.	
HX-01	Heater	Electrical heater to increase the temperature of the gasifying agent mixture to 485°C.	

The IHBFBSR model is solved fulfilling the heat and mass balance, equations (11) and (12).

$$m_{feed} + m_{N_2} + m_{air} + m_{steam} = m_{prodgas} \tag{11}$$

$$m_{feed}h_{feed} + m_{N2}h_{N2} + m_{air}h_{air} + m_{steam}h_{steam} + heat = m_{prod\ gas}h_{prod\ gas} + QAMB \tag{12}$$

Equation (11) describes the IHBFBSR inputs and outputs, the inputs are the PW-DKR350 mixture called “feed”, the two gasifying agents (air and steam), and the nitrogen stream for feeding the PW-DKR350 mixture; meanwhile, the only output of the IHBFBSR is the product gas stream (in this model the solids and gases are leaving the IHBFBSR together because this model does not consider the geometry of the IHBFBSR).

In equation (12), the “heat” term represents the thermal duties delivered by the burners of the IHBFBSR: QB100 and QB80. The duty values are calculated by a design spec coupled to the pyrolyser (QB100), and gasifier (QB80), respectively. The design spec QB100 was kept constant to achieve a pyrolysis temperature of 700°C because at this temperature, based on experimental data from the pyrolysis of each polyolefin, more than 50% of the feedstock has become volatile matter (VM) [69].

Therefore, the only design spec varying in function of the sensitivity parameters was the QB80. The convergence of the design spec is verified by the duty stream “QAMB”.

The gasification reactions in the RGibbs block are solved by applying the chemical equilibrium and restricted equilibrium approach. This block requires specifying the products and inert compounds. The inorganic impurities in the feed stream were defined as inert compounds, otherwise the RGibbs block considers them for the calculation of the equilibrium compositions, returning values close to zero.

3.1.2 Restricted equilibrium approach (REA)

In this strategy, will be identified the degrees of approach for a set of gasification reactions, considering the extensive work needed to identify the degree of approach per reaction without experimental data related to the gasification of the feedstock to adjust the degrees of approach, the implementation of the REA will be done in two parts.

Firstly, different degrees of approach (0°C, -100°C, -200°C, …) will be applied to the baseline case in the temperature range, determined during section 3.1.1, to measure the effect of the degree of approach in the yield of the permanent gases, CCE, CGE and GY.

Secondly, the individual REA option will be enabled to determine the degrees of approach per reaction. Despite there is limited literature dedicated to evaluating this option [59], it is well known that the oxidation reactions cannot be considered for this model because their reaction rates are several orders of magnitude higher than the rest of participating reactions, then the only available options are the WGS, steam and dry reforming reactions. However, the selection of the reactions must accomplish the simulator requirements: “for n possible products, there must be a minimum of n/2 number of chemical reactions specified, including one of the product compounds either as a reactant or product [70]. Then, will be checked the possibility of including an oxidation reaction to accomplish this point.

3.1.3 Equilibrium approach including PSD

This strategy aims to include the effect of particle diameter and particle size distribution of the bed material and feedstock. Firstly, the stream class must be changed to MCINCPSD to enable the particle size distribution (PSD) option. In Aspen plus, each particle type (feedstock, char, ashes) can have its PSD mesh, this option is the most complete when the experimental data of each particle is available. Otherwise, the PSD mesh of the feedstock must be created and populated using user-specified values or a distribution function. In the simulator exits the option to select between two PSD models: keep constant the PSD or the number of particles, the former option applies the uniform conversion model (UCM), the latter the shrinking unreacted particle model (SUPM) [56].

The PSD mesh for the feedstock was defined as an equidistant division of 10 intervals from 1 to 6 mm, an average value of 4 mm and a standard deviation of ±1 mm. The same PSD mesh is used for char and ashes selecting the PSD model “number of particles constant”. The selection of the mesh intervals and average diameter is based on the Literature Study findings, whereas the standard deviation and the PSD model will be reviewed through this strategy [22] [71].

Similarly to section 3.1.1, the RGibbs block will be solved applying the equilibrium approach and REA. The selection of the degree of approach will be based on the findings from the previous approach.

3.1.4 Equilibrium approach including pyrolysis correlations

This strategy is built on the work done by Gungor & Eskin [72], Abdelouahed et al. [53], and Q. Xiong et al [73] to develop semi-empirical correlations as function of the temperature to describe the pyrolysis of coal, wood chips and straw respectively. The steps describing the development of the correlations for a polyolefin waste mixture and its applicability to the feedstock are summarizes in Figure 16.

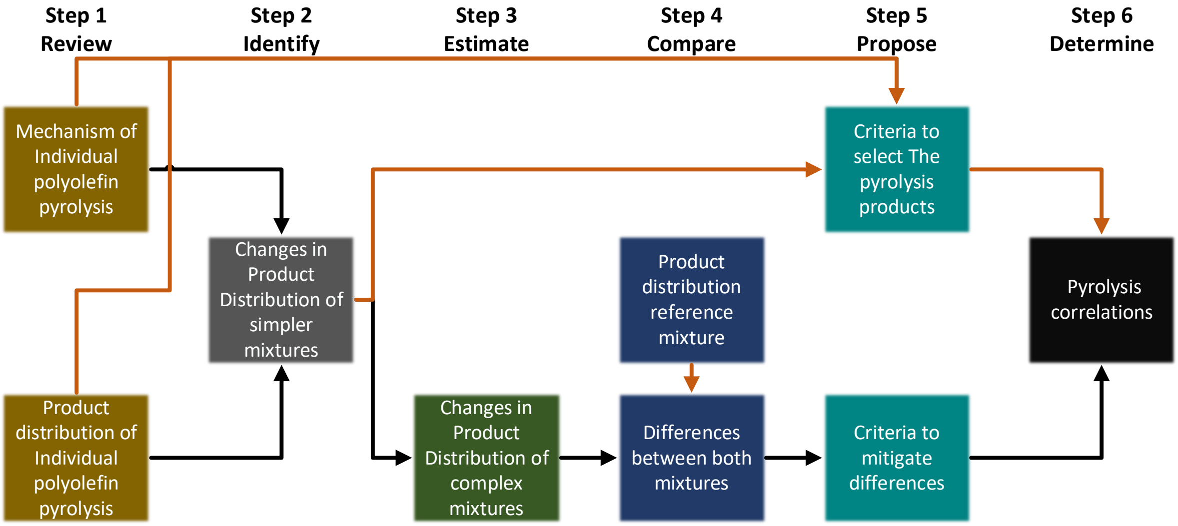

Figure 16. Roadmap for the development of pyrolysis correlations. Black arrows indicate the sequence to mitigate the differences in the mixture composition, orange arrows indicate the sequence to select the pyrolysis products.

1) **Review of the individual pyrolysis mechanism of the polymer**. All the mechanisms are characterized by the random chain scissoring in the double carbon bonds along the polymer backbone deriving in shorter polymeric chains up to forming oligomers [30]. The differences between polymers rely on the secondary reactions forming more stable species [74].

   Table 11 summarizes each pyrolysis mechanism and provides the main pyrolysis products of each polymer. Except for PVC, the main product of all the polymers is their own monomer. The main characteristics and assumptions of each polymer pyrolysis are the following:

   - The main pyrolysis product from PE and PP are their monomers ethylene and propylene respectively [32]. However, at higher temperatures, the ethylene and propylene content get lower whilst the methane content increases [74].
   - The tar compounds formed by PE and PP are only single and double rings compounds [75].
   - Benzene is the most abundant single ring compound formed by PE, PP and PVC pyrolysis [16].

Table 11. Pyrolysis mechanisms and products of polyolefins [16] and PET [75].

Polymer	Pyrolysis mechanism	Main products [69] [76]	Main tar compounds			
			Single Ring	Double Ring	Triple Ring	Quadruple Ring
PE	• Random chain scissoring. • Recombination vs ring-closure.	Ethylene Methane Propylene	Benzene Toluene	Naphthalene	None	None
PP	• Random chain scissoring. • Recombination vs ring-closure.	Propylene Butylene Methane	Benzene Toluene	Naphthalene	None	None
PS	• Chain scissoring in the methyl group. • Alkyl addition to single ring. • Ring recombining plus dehydrogenation	Ethylene Methane Propylene	Styrene Benzene Toluene	Naphthalene	Fluorene	Chrysene
PET	• Chain scissoring in the C=O bonds. • Deoxygenation. • Ring recombining plus dehydrogenation. • Soot formation	CO CO_2 H_2	Vinyl benzoic acid Benzoic acid	Naphthalene	Phenanthrene	Chrysene
PVC	• Dehydrochlorination • Inner cyclization • Aromatic scissoring • 3 and 4 rings release • Double ring release • Soot formation	HCl H_2 Methane	Benzene Toluene	Naphthalene	Phenanthrene	Chrysene

- Compounds from the benzoic acid family are the most abundant single ring compounds formed by PET pyrolysis. However, their content reduce as the pyrolysis temperature increases because of their decomposition to benzene/toluene plus CO/CO_2 [75].
- PS has the highest tar yield (>90%w) and its monomer is the main pyrolysis product [74].
- Naphthalene is the most abundant double ring compound formed by all the polymers [75].
- Phenanthrene and Chrysene are the most abundant triple and quadruple ring compounds from PS pyrolysis [75].
- PVC has the highest permanent gas yield (>50%w), even after removing HCl from the pyrolysis products [30] [74].

2) **Identify the main role of each polyolefin and PET in the PW mixture.** Based on bibliography research, the role of each polymer is:

   - Due to the similarity between the polymeric chains pf PE and PP, exits a good diffusion of the radicals formed by the chain scissoring of both polymers, deriving in interactions that increases considerably the content of H_2 and single ring tar whilst the content of CO_2 and double ring tar gets lower [3] [31].
   - PS is the highest tar producer [16].
   - The CO and CO_2 content depends directly on the PET content in the mixture because is the only oxygenated polymer.
   - PVC has the highest H_2 yield which has a linear relation to the HCl content. Thus its contribution to the H_2 content can be directly related to the HCl measured in a gasification test [16].

It is out of scope of this study describing the effect of the different nonlinear interactions in the product distribution of the PW mixture. However, it is known that the gas composition of a complex mixture is typically controlled by the polymer(s) with the highest content in the mixture [3] [69]. Thus, as first approach seems reasonable to use experimental data from a PW mixture whose major polymers are like the ones in the feedstock.

3) **Identify the reference mixture.** The selected reference PW mixture was taken from the Kaminsky studied [77] including the pyrolysis products in the temperature range 680-790°C. However, the Kaminsky sample is a real-life mixture of plastic waste, whereas the feedstock studied is a pre-threated mixture according to the DKR350 specification having a minimum content of PVC and PET. There are two remarkable differences between the Kaminsky sample and the feedstock (Table 12):

   - Higher PVC and PS content in the Kaminsky sample than in the feedstock.
   - Higher O_2 content in the feedstock derived from the PET and organic waste content.

Table 12. Polymeric, Proximate and Ultimate content of the PW found in the literature [77] and PW-DKR350 mixture.

Sample	**Polymer content**									
	M	**PE**	**PP**	**PS**	**PVC**	**PET**	**Other plastics**	**Organic waste**	**Paper**	**Ashes**
Kaminsky	0.2	42.75	14.25	19	13.7	0	4.8	0	0	5.3
PW-DKR350	0	51	22	1	1	5	7	3	5	5

Sample	Proximate Analysis (%)				Ultimate Analysis (%)						
	M	FC	VM	A	A	C	H	N	Cl	S	O
Kaminsky	0.2	5	89.5	5.3	5.3	79.1	11	0.5	7.8	0	1.6
PW-DKR350	0.38	8.97	84.56	6.09	6.09	79	12	0.4	0	0	8.6

4) **Mitigate the differences in the composition between both samples.** The following two assumptions were implemented to mitigate the differences in the composition:

   - The chlorine atoms only react with hydrogen atoms to form HCl, thus the excess hydrogen will be considered as molecular H_2.
   - The oxygen atoms derived from PET and organic waste can only produce CO and CO_2. Thus, the excess oxygen will be considered as molecular O_2.

5) **Determine the pyrolysis products**. The selection of the compounds formed during the pyrolysis steps is based on Table 11 and the Literature Study findings [3] [31] [69] [16] [75]:

   - Light HC compounds (C2-C5), including the monomers ethylene and propylene. The alkene content must be higher than the alkane content in a ratio equals to 3:1 or higher [69].
   - Include benzene and styrene between the single ring compounds [16] [31].
   - The double ring compounds are grouped by naphthalene ($C_{10}H_8$) because is the simplest and most abundant double ring compound in any of the polyolefins' pyrolysis [75] [31].
   - The triple ring compounds can be grouped by Phenanthrene ($C_{14}H_{10}$) because is the most abundant tar compound formed by PS and PVC pyrolysis [75] [31].
   - Discard the formation of quadruple-ring compounds considering that PE+PP are the major polymers of the mixture [3] [31].

   The benzoic acid and relatives were discarded from the pyrolysis products because of the minimum content of PET in the feedstock. Also, considering the operating temperature range of the IHBFBSR (700-850°C), is highly probable that benzoic acid decomposes into CO/CO_2 plus a single ring compound [75].

Determine the coefficients of the pyrolysis correlations. The coefficients are determined by applying a second order polynomial regression to the mass fraction of each compound found in the reference mixture. The coefficients obtained from such regressions are shown in Appendix Table 30.

The coefficients of all the pyrolysis correlations are included in a calculator block coupled to the PYRO block. Downstream, the molecular O_2 was converted to CO and CO_2 in the "impurities" reactor block (Figure 15). with a conversion ratio CO_2:CO equals to 0.6:0.4. This correction was included to avoid the inconsistency of forming O_2 after pyrolysis bases on the distribution of this compounds seen in the Kaminsky sample.

Finally, the RGibbs block requires to identify which compounds will be considered inerts to avoid getting the same product gas composition than in section 3.1.1. Besides, the RGibbs block will be solved applying the equilibrium approach, and REA, the selection of the degree of approach will be based on the findings from section 3.1.2.

3.1.5 Kinetic approach using the Fluidbed block

In this strategy, the RGibbs block in Figure 15, is substituted by the Fluidbed block to include the hydrodynamics of the fluidized bed and the kinetics of the gasification reactions. The Fluidbed block is a pre-defined block composed by multiple cells (CSTRs blocks) operating at isothermal conditions, it requires the specification of the hydrodynamic models for the bed, transport disengagement and freeboard zones (Figure 17).

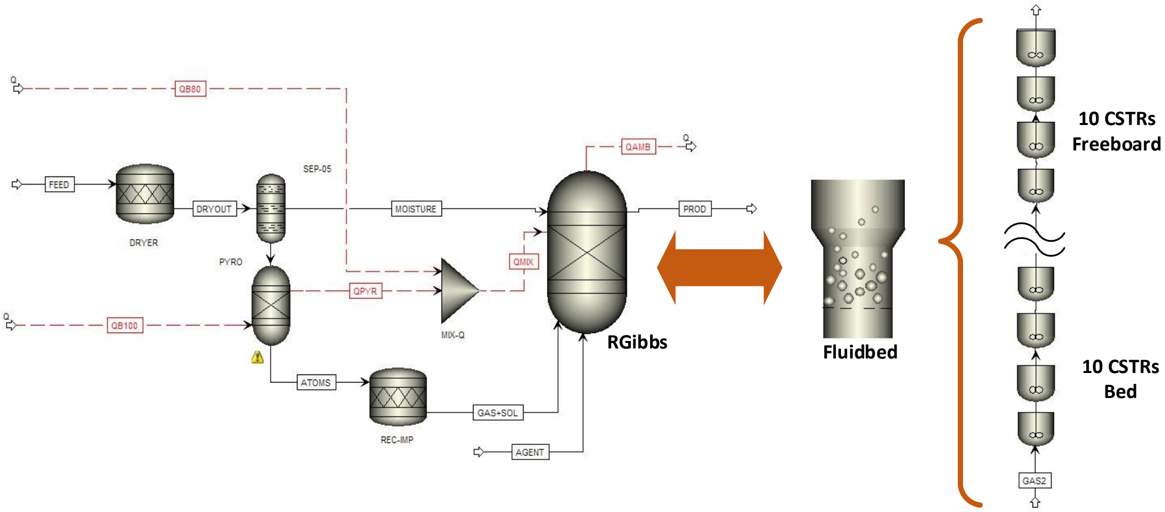

Figure 17. Substitution of the RGibbs by the Fluidbed block in the kinetic approach. The complete description of the process flow diagram is given by Figure 15.

The selection of the hydrodynamic models (Table 14) is determined by the Geldart classification of the bed particles (Geldart B for corundum), IHBFBSR design data and Aspen plus recommendations [78]. Additionally, the bed voidage (ε_{mf}) and velocity (U_{mf}) at minimum fluidization will be determined in a user model coupled to the Fluidbed block according to the bed load (m_{bed}) and particle density (ρ_p) in Table 13.

Table 13. Bed particle properties.

Symbol	Description	Value	Unit
dp	Particle Diameter	5E-04	m
ρp	Particle Density	3950	kg/m^3
m_{bed}	Bed Load	100	kg

Table 14. Settings for the hydrodynamic models of the Fluidbed block.

Section 1	**Specifications**
Bed load:	100 kg
Bed voidage at minimum fluidization conditions (ε_{mf}):	0.45 (initial guess)
Geldart classification:	Geldart B
Velocity at minimum fluidization conditions:	0.1 m/s (initial guess)
Transport disengagement height model:	George and Grace
Maximum dCv/dh:	.001 (recommended by Aspen plus manual) [78]
Elutriation:	Colakyan & Levenspiel
Decay constant (a):	6.4 m^{-1} [79]
Section 2	**Operation**
	Isothermal reactor
Section 3	**Geometry**
	Dimensions, height profile and location of the inlet streams are given in Table 15.
Section 4	**Gas distributor**
Type:	bubble cap plate (IHBFBSR design data)
Number of bubble caps:	50 (IHBFBSR design data)
Number of cap orifices:	2 (IHBFBSR design data)
Cap orifice diameter:	5 mm (IHBFBSR design data)
Cap orifice discharge coefficient:	0.8 (recommended by Aspen plus manual) [78].
Section 5	**Convergence**
Number of cells for the bed zone:	10 (minimum quantity allowed by Aspen) [78].
Number of cells for the freeboard:	10 (minimum quantity allowed by Aspen) [78].

The calculation approach included in the user model for the minimum fluidization conditions is the following:

1. Calculate the superficial velocity of the gasifying agent (U) in m/s.

$$U = \frac{M_g}{AG * \rho_g} \tag{13}$$

Where:
Mg = gasifying agent mass flow (kg/s).
AG = cross sectional area of the IHBFBSR (m^2).

2. Calculate the Archimedes number (Ar) of the bed particle suspended by the gas flow.

$$Ar = \frac{gdp^3 \rho_g (\rho_p - \rho_g)}{\mu_g^2} \tag{14}$$

Where:
g = gravity acceleration (m^2/s).
μg = gasifying agent viscosity (kg/ms)

3. Calculate the Reynolds number at minimum fluidization conditions using the empirical correlation proposed by Wen and Yu [80] for irregular particles on a fluidized bed ($\mathrm{Re_{mf}}$).

$$\mathrm{Re_{mf}} = (33.7^2 + 0.0408\mathrm{Ar})^{0.5} - 33.7 \tag{15}$$

4. Calculate the velocity at minimum fluidization conditions (Umf) [56] in m/s.

$$\mathrm{U_{mf}} = \mathrm{Re_{mf}}\left(\frac{\mu_g}{d_p \rho_g}\right) \tag{16}$$

5. Calculate the bed voidage at minimum fluidization conditions (ε_{mf}) [55] [81].

$$\varepsilon_{mf} = 0.478 * \mathrm{Ar}^{-0.018} \tag{17}$$

$$177 < \mathrm{Ar} < 4030$$

Next, all the reactions, including the water gas shift reaction (WGS), are described as power law expressions. The WGS reaction was divided in the forward and backward reactions, despite most of the modeling studies described it as a reversible reaction [49] [56] [66] [82], aiming to use the optimized kinetic parameters developed by Abdelouahed et al. [53] to achieve a more accurate CO yield.

For the light hydrocarbons and single-ring tar, determined by the pyrolysis correlations in section 3.1.4, without kinetic expressions, its partial oxidation reaction will be included by adapting the empirical kinetic expression for tar, equation (18). The pre-exponential and activation energy determined for each hydrocarbon are included in the Appendix Table 33 [56] [62].

$$r_{tar} = 2.08x10^9 * T * \exp\left(-\frac{164.5}{RT}\right) C_{O_2} C_{tar}^{0.5} \qquad \left(\frac{kg}{m^3 s}\right) \tag{18}$$

Where:
T = Temperature (K)
C_i = mass concentration (kg/ m^3)

Finally, the power law expression for char combustion was modified by a calculator block to calculate the stoichiometric coefficients in function of the IHBFBSR temperature and include the carbon conversion (Xc), the modified kinetic expression is included in the Appendix Table 32.

3.1.6 Kinetic approach using the CSTR-PFR blocks

In this strategy, the Fluidbed block will be substituted by a CSTR and PFR to model the bed and freeboard zones, respectively. The CSTR is an isothermal reactor while the PFR is an adiabatic system, this substitution implies the disappearance of the transport disengagement zone turning the freeboard into a solids-free system (Figure 18), also the hydrodynamic model will be limited to determine the volume of the bed zone and its gas phase.

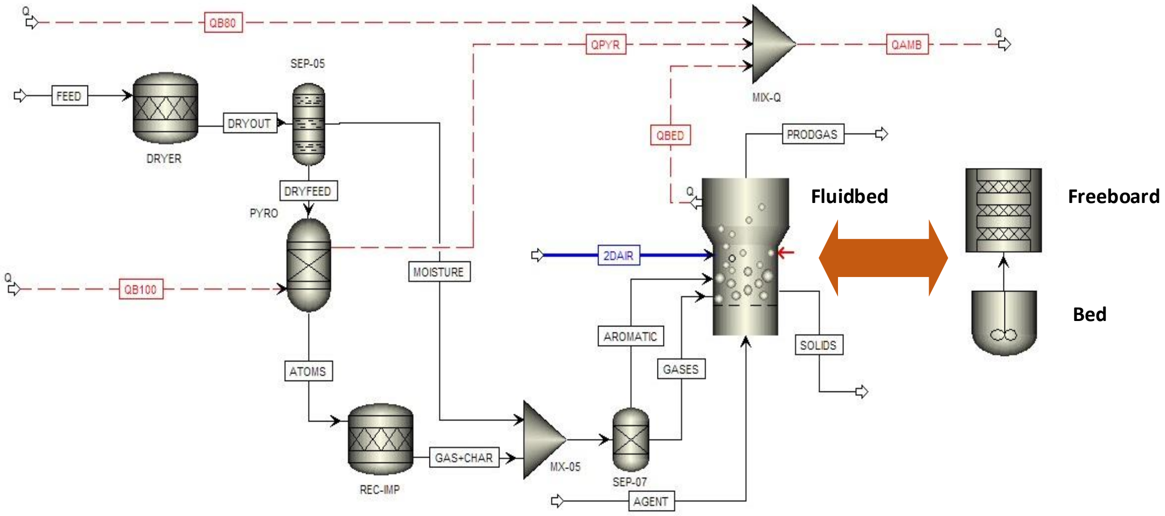

Figure 18. Substitution of the Fluidbed block by the CSTR-PFR configuration. The complete description of the process flow diagram is given by Figure 15.

Also, the kinetic expressions were grouped in six packages to distinguish the reactions happening at each zone.

1. Homogenous reactions in the bed and freeboard blocks (Table 31).
2. Water gas shift (WGS) reaction in the bed and freeboard blocks (Table 31).
3. Heterogenous reactions in the bed block (Table 32).
4. Light hydrocarbons in the bed and freeboard blocks (C2-C5 compounds in Table 33).
5. Single ring tar in the bed and freeboard blocks (C6-C8 compounds in Table 33).
6. Polynucleic atoms in the freeboard block (>C10 compounds in Table 33)

Similarly to the Fluidbed block, the dimensions of the bed and freeboard zones are defined in function of the load of bed particles (m_{bed}), the gasifying agent flow and their properties (Table 9 and Table 13). The calculation of the bed volume (V_{bed}) and its gas volume (V_{gas}) requires a user model coupled to the CSTR block. This user model follows the approach proposed by Pauls et al [83] to calculate the bed height at minimum fluidization (H_{mf}) and bubbling (H_{bed}) conditions.

The first step is to include the equations (13) to (17) from section 3.1.5 together with the following set of equations in the user model:

6. Determine the bed expansion factor (B) proposed by Babu et al. [62].

$$B = 1 + \frac{14.314 * \left(U - U_{mf}\right)^{0.738} dp^{1.006} \rho_p^{0.376}}{\rho_g^{0.126} U_{mf}^{0.937}} \tag{19}$$

Where:
U = superficial gas velocity (m/s)
Umf = minimum fluidization velocity (m/s)
dp = bed particle diameter (m)
ρp = bed particle density (kg/m^3)
ρg = gasifying agent density (kg/m^3)

7. Calculate the bubble voidage (ε_b) [62].

$$\varepsilon_b = 1 - \frac{1}{B} \tag{20}$$

8. Determine the bed voidage (ε_f) according to Kunii and Levenspiel equation [62].

$$\varepsilon_f = \varepsilon_b + (1 - \varepsilon_b)\varepsilon_{mf} \tag{21}$$

9. Calculate the bed height at minimum fluidization conditions (H_{mf}) in m.

$$H_{mf} = \frac{m_{bed}}{AG(1 - \varepsilon_{mf})(\rho_p - \rho_g)} \tag{22}$$

10. Calculate the bed height (H_{bed}) in m.

$$H_{bed} = H_{mf}B \tag{23}$$

11. Calculate the bed volume (V_{bed}) and its gas volume (V_{gas}) in m^3.

$$V_{bed} = H_{bed}AG \tag{24}$$

$$V_{gas} = \varepsilon_f V_{bed} \tag{25}$$

Finally, the freeboard zone is divided in 6 locations wherever there is a change of the cross-sectional area, either by an increase of the vessel diameter or the presence of a burner in function of the height profile shown in Figure 19. The freeboard height (H_{FB}) is calculated like the difference of the IHBFBSR height (H8) minus the bed height (H_{bed}) calculated by equation (23) [27]. The locations (FB1-FB6) in function of the IHBFBSR height, are calculated in a user model coupled to the PFR block, the calculation method is described in Table 15.

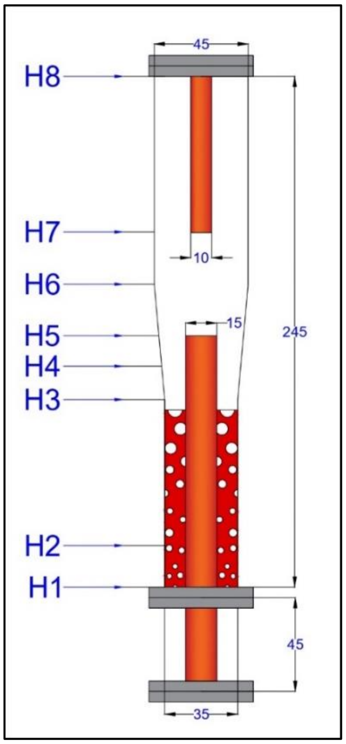

Figure 19. Dimensions of the IHBFBSR in centimeters adapted from [6].

Table 15. Dimensions of the IHBFBSR taken from [6].

Height profile	IHBFBSR Height (m)	Vessel Diameter (m)	Burner Diameter (m)	Cross Sectional area (m2)	Height (m)	Location	Height (%)
H8	2.454	0.447	0.100	0.1491	$H_{FB} = H_8\text{-}H_{bed}$	FB6	1
H7	1.704	0.447	0.100	0.1491		FB5	$(H7 - H_{bed})/H_{FB}$
H6	1.453	0.447	0.000	0.1569		FB4	$(H6 - H_{bed})/H_{FB}$
H5	1.206	0.382	0.150	0.0971		FB3	$(H5 - H_{bed})/H_{FB}$
H4	1.068	0.346	0.150	0.0764		FB2	$(H4 - H_{bed})/H_{FB}$
H3	0.9	0.346	0.150	0.0764	H_{bed}	FB1	0
H2	0.2	0.346	0.150	0.0764			
H1	0	0.346	0.150	0.0764			

The locations values (FB1-FB6) are initially equal to the height profiles (H3-H8), to later be adjusted in function of the H_{bed} calculated by equation (23). If the bed height is higher than a height profile, the location value becomes zero and the rest of locations above are corrected by the user model.

3.1.7 Kinetic approach including the two-phase model.

This strategy integrates the semi-empirical correlations of the two-phase model (TPM) in a user model to describe the bubble and emulsion phase of the bed zone, they are modelled by pairs of PFR and CSTR respectively whose output streams enter another user model which equals the component flow in each phase before starting the next pair (Figure 20) [66]. The following restrictions are considered:

- The radial composition is uniform.
- The emulsion phase conditions are higher than the minimum fluidization conditions.
- There is presence of solids in the bubble phase.
- The heat transfer effects are neglected because the bed zone operates at isothermal conditions.
- Bubble diameter is constant along each CSTR-PFR pair.

Both phases are linked by the mass transfer between them described by equations (26)-(27). In both equations, the first term refers to the inlet/outlet convective mol flow, and the second term is the mass transfer between both phases.

- Mol balance of bubble phase, p_{gb} (kgmol/m^3), F (kgmol/s), V (m^3), ε_b (bubble phase voidage),K_{be} (1/s):

$$\left(F_{Ab(in)} - F_{Ab(out)}\right) - K_{be}\left(Y_{Ab(in)} - Y_{Ae(in)}\right)\rho_{gb}\mathrm{V}_b\varepsilon_b = 0 \tag{26}$$

- Mol balance of emulsion phase, p_{ge} (kgmol/m^3), F (kgmol/s), V (m^3), ε_b(emulsion phase voidage), K_{be} (1/s):

$$\left(F_{Ae(in)} - F_{Ae(out)}\right) + K_{be}\left(Y_{Ab(in)} - Y_{Ae(in)}\right)\rho_{ge}\mathrm{V}_e\varepsilon_e = 0 \tag{27}$$

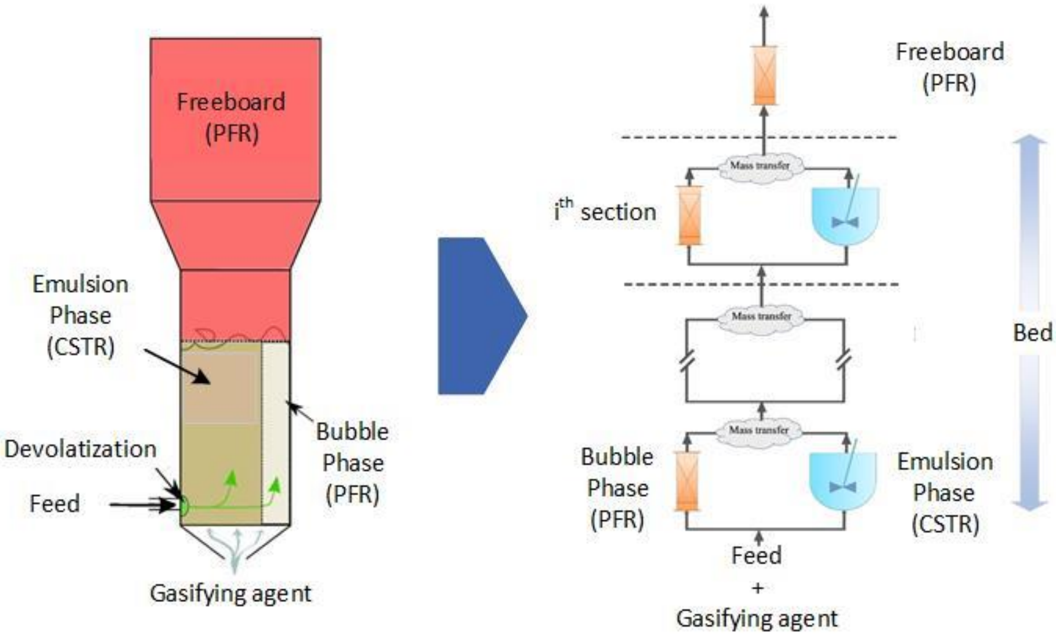

Figure 20. Representation of the two-phase model in Aspen plus. Diagram developed by Rafati et al. [84] [61].

The solution method is based on the approach proposed by Rafati et al [66], the bed volume (V_{bed}) is divided in four PFR-CSTR pairs because this number of pairs has shown a good agreement in previous works [66] [61] [85]. The bubble (Vb) and emulsion (Ve) volumes will be determined using the equations (13)-(17) from sections 3.1.5, equations (19)-(25) from section 3.1.6, and the following set of correlations [66] [61].

12. Divide the bed volume (V_{bed}) by the number of sections (n).

$$V_{(i)} = \frac{V_{bed}}{n} \tag{28}$$

$$n = 4$$

13. Calculate the volume of the PFR block for the bubble volume at section ith (V_{bi}).

$$V_{PFR} = V_{(i)}\sigma \tag{29}$$

14. Calculate the volume of the CSTR block for the emulsion volume at section ith (V_{CSTR}).

$$V_{CSTR} = V_{(i)}(1-\sigma) \tag{30}$$

15. Calculate the bubble volume at section ith (V_{PFR}).

$$V_{b(i)} = V_{PFR}\varepsilon_b \tag{31}$$

16. Calculate the emulsion volume at section ith (V_{ei}).

$$V_{e(i)} = V_{CSTR}\varepsilon_e \tag{32}$$

17. Calculate the emulsion velocity (U_e) [86] in m/s.

$$U_e = \frac{U_{mf}}{\varepsilon_{mf}} \tag{33}$$

18. Calculate the bubble diameter (d_b) in m.

$$d_b = 0.21H_f^{0.8}\left(U - U_{mf}\right)^{0.42} \exp\left(-0.25\left(U - U_{mf}\right)^2 - 0.1\left(U - U_{mf}\right)\right) \tag{34}$$

19. Calculate the bubble rise velocity (U_{br}) in m/s.

$$U_{br} = 0.711\sqrt{gd_b} \tag{35}$$

20. Calculate the bubble velocity (U_b) in m/s.

$$U_b = U - U_e + U_{br} \tag{36}$$

21. Calculate the bubble volumetric fraction (σ).

$$\sigma = 0.534 - 0.534 \exp\left(-\frac{\left(U - U_{mf}\right)}{0.413}\right) \tag{37}$$

22. Calculate the bubble phase voidage (ε_b) [86].

$$\varepsilon_b = 1 - 0.146 \exp\left(-\frac{\left(U - U_{mf}\right)}{4.439}\right) \tag{38}$$

23. Calculate the emulsion phase voidage (ε_e).

$$\varepsilon_e = \varepsilon_{mf} + 0.2 - 0.059 \exp\left(-\frac{\left(U - U_{mf}\right)}{0.429}\right) \tag{39}$$

Next, the overall mass transfer coefficient (K_{be}) in equations (26) and (27) is calculated by including the following semi-empirical correlations [66] [61].

24. Calculate the mass transfer coefficient bubble-cloud (K_{bc}).

$$K_{bc} = 4.5\left(\frac{U_e}{d_b}\right) + 5.85\left(\frac{D_{AB}^{0.5} * g^{0.25}}{d_b^{1.25}}\right) \qquad \text{(40}$$

25. Calculate the mass transfer coefficient cloud-emulsion (K_{bc}).

$$K_{ce} = 6.77\left(\frac{D_{AB} * \varepsilon_e * U_b}{d_b^3}\right)^{0.5} \tag{41}$$

26. Calculate the overall mass transfer coefficient (K_{be}).

$$\frac{1}{K_{be}} = \frac{1}{K_{bc}} + \frac{1}{K_{ce}} \tag{42}$$

For the first PFR-CSTR pair is needed to specify the initial compound distribution between the bubble and emulsion phase. The first compound distribution is the following:

Table 16. Feed distribution at the first section of the bubble-emulsion system.

Group	Compound	Initial phase
Permanent gases	CO, CO_2, H_2, CH_4	Emulsion/ Bubble, splitting in function of the cross-sectional area of bubble and emulsion phase.
Light hydrocarbons	Ethane (C_2H_6) Ethylene (C_2H_4) Propane (C_3H_8) Propylene (C_3H_6) C4 and C5	Emulsion/ Bubble, splitting in function of the cross-sectional area of bubble and emulsion phase.
Tar	Single ring Double ring Triple ring	Emulsion/ Bubble, splitting in function of the cross-sectional area of bubble and emulsion phase.
Char	C	Emulsion
Impurities	Hydrogen Chloride (HCl) Hydrogen Sulfide (H_2S) Ammonia (NH_3)	Bubble
Gasifying agent	Nitrogen Air Steam	Emulsion/ Bubble, splitting in function of the cross-sectional area of bubble and emulsion phase.

The following PFR-CSTR pairs utilize a user model to redistribute the compound flow. If the inlet component flow of the emulsion (F_{Abin}) and bubble (F_{Aein}) phase are positive, then the equations (26) and (27) are rewritten as follows:

$$F_{Ab(out)} = F_{Ab(in)} - K_{be}\left(Y_{Ab(in)} - Y_{Ae(in)}\right)\rho_{gb}\mathrm{V}_b\varepsilon_b \tag{43}$$

$$F_{Ae(out)} = F_{Ae(in)} + K_{be}\left(Y_{Ab(in)} - Y_{Ae(in)}\right)\rho_{ge}\mathrm{V}_e\varepsilon_e \tag{44}$$

Nevertheless, if there is a difference between the outlet flows of the bubble (F_{About}) and emulsion (F_{Aeout}) phase, the user model calculates a split fraction to achieve that both flows are equal. The Fortran script used to distribute the components flow is given in the Appendix section 8.4.

Next, the freeboard zone is modeled again as a PFR block free of solids [55]. The height locations are taken again from Table 15.

Finally, in this strategy the kinetic expressions were redistributed in seven packages because the CO combustion only occurs in the emulsion phase [66].

1. Homogenous reactions in the emulsion, bubble and freeboard blocks (Table 31).

2. CO combustion reaction in the bubble and freeboard blocks (Table 31).
3. Water shift gas (WGS) reaction in the emulsion, bubble and freeboard blocks (Table 31).
4. Heterogenous reactions in the emulsion block (Table 32).
5. Light hydrocarbons in the emulsion, bubble and freeboard blocks (C2-C5 compounds in Table 33).
6. Single ring tar in the bubble and freeboard blocks (C6-C8 compounds in Table 33).
7. Polynucleic atoms in the freeboard block (>C10 compounds in Table 33)

3.2 Validation cases

The last part of this study is the application of the different equilibrium and kinetic models to model two experimental works found during the Literature Study, the objective is to identify the final adjustments needed by the kinetic models to improve their accuracy.

1. “Design and first experimental results of a bubbling fluidized bed for air gasification of plastic waste “by Martinez-Lera et al. [87].
2. “Fluidized-Bed Gasification of Plastic Waste, Wood, and their Blends with Coal” by Zaccariello & Mastellone [88]

4 Results and Discussion

4.1 Equilibrium approach

The results from the equilibrium approach serve to narrow down the possible combinations of ER and SF that accomplish the heat balance condition given by equation (12) inside the temperature range 700-850°C. The key indicators were prioritized to identify the best ER and SF combinations:

$$CCE > CGE > H_2 \text{ yield} > CO \text{ yield} > GY > CH_4 \text{ yield} > CO_2 \text{ yield}$$

The CCE indicator has the highest relevance in this section due to the low fixed carbon content in the PW-DKR350 mixture compared to other carbonaceous feedstocks, thus considering that the major compounds are PE and PP whose individual gasification and co-gasification achieves a complete CCE, the CCE helps to quantify the effect of other polymers and organic waste in the feedstock [31]. Besides, the GY indicator was located between the CO and CO_2 yield regarding that the best combination of ER and SF must increase the content of H_2 and CO over a higher product gas yield which could include undesired products as CO_2 and tar.

Finally, the equilibrium approach tends to underestimate the CH_4 formation and does not consider the formation of heavier hydrocarbons [50], then the CH_4 yield, and tar yield indicators are not considered in this section.

Figure 21 show the indicators: CCE, CGE, H_2 yield, CO yield, CO_2 yield, in the temperature range 700-850°C at different combinations of ER and SF ratios. In the baseline case, the IHBFBSR model accomplished the heat balance condition between the temperature range 700-850°C, at ER values between $0.1 < ER < 0.2$ when $SF > 1$. On the contrary, at $ER < 0.1$, the heat balance condition was only solved in the temperature range 700-780°C because of the maximum duty released by the two burners. Reducing the ER at 0.05, the SF must be reduced at 0.5, while at $ER > 0.2$, the IHBFBSR turned in a non-adiabatic system, failing the heat balance condition. It was necessary to increase the SF ratio to 7.5 to fulfil the heat balance condition along the whole temperature range, which is unrealistic.

From the CCE plot in Figure 21, the combinations with a $SF < 1$ are discarded because they cannot achieve a complete CCE. Moreover, the ER=0.05, SF=0.5 combination has the lowest CCE, CGE and GY. This case highlights the importance of the priority order given to the indicators as the ER=0.05, SF=0.5 case has the highest H_2 yield, which can mislead the rest of the analyses.

Next, the CGE plot in Figure 21 shows that the combinations with an ER=0.1 and $SF > 1$ got a complete CGE. When the ER value was increased from 0.1 to 0.15, the CGE decreased by 5%, and the combination with higher SF values (up to reach 7.5) resulted in lower CGE values. Thus, the combinations with an ER=0.1 are identified as the best for the gasification of the PW-DKR350 with this approach.

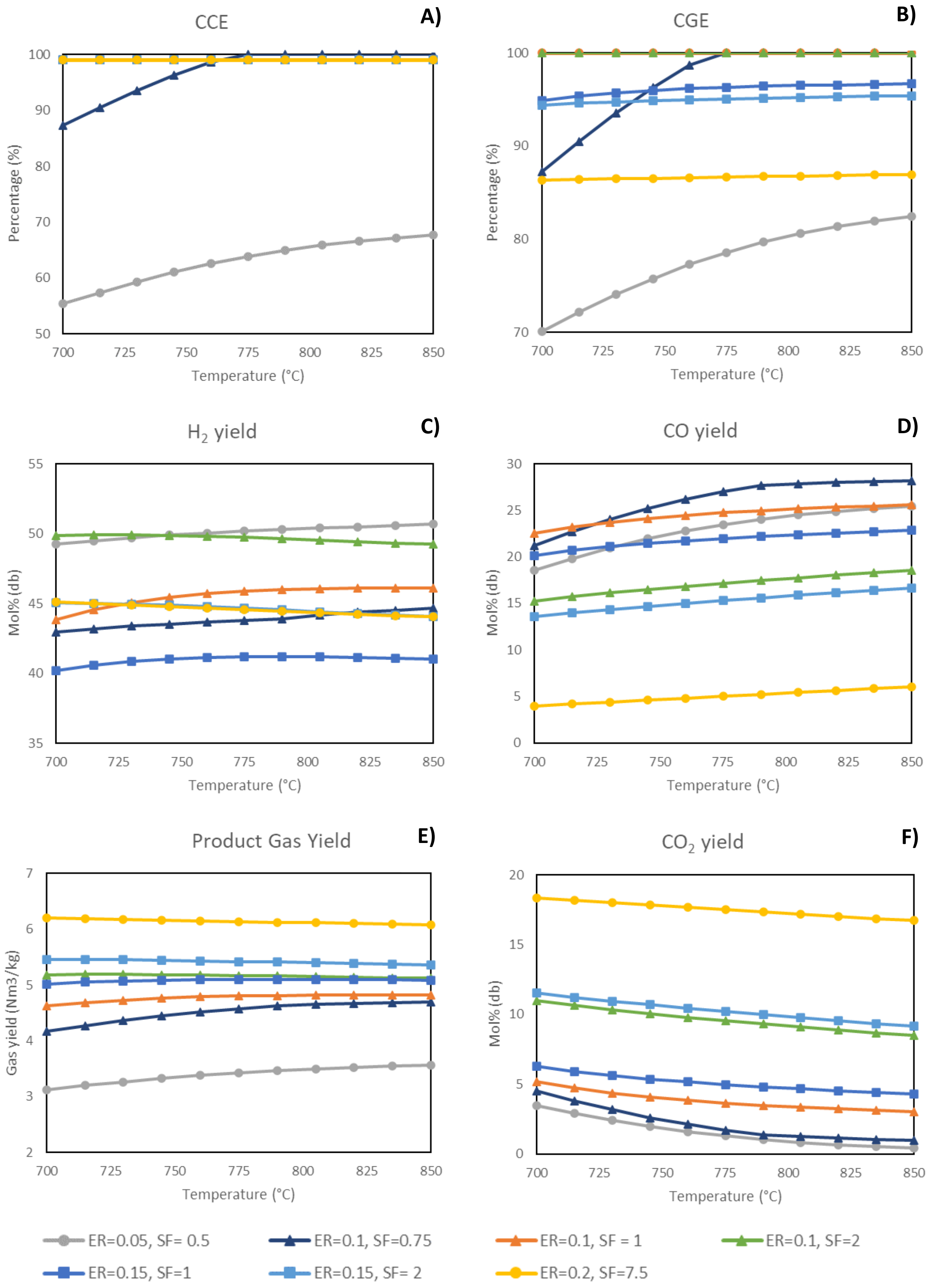

Figure 21. Indicators CCE (A), CGE (B), H_2 yield (C), CO yield (D), product gas yield (E) and CO_2 yield (F) at different combinations of ER and SF ratios applying the equilibrium approach.

The H_2 yield indicator plot in Figure 21, shows that the combinations with the highest yield are the ER=0.1, SF= 2 followed by ER=0.1, SF= 1. Although in the CO yield plot the combination with the highest values (discarding the combination ER=0.1 and SF=0.75) was the ER=0.1 and SF=1 whilst for the combination ER=0.1 and SF=2, the CO content was reduced in 8% through the entire temperature range. Therefore, following the priority order given to the indicators, the combination ER=0.1, SF=2, showing the highest CCE, CGE and H_2 yield, will be used as reference for the further upgrading strategies in this work.

Figure 22 gives the content of H_2, CO, CO_2 and CH_4 in the product gas at ER=0.1 and SF=2. The figure validates the hypothesis that the CH_4 content determined by this approach is zero [52] [53] [54].

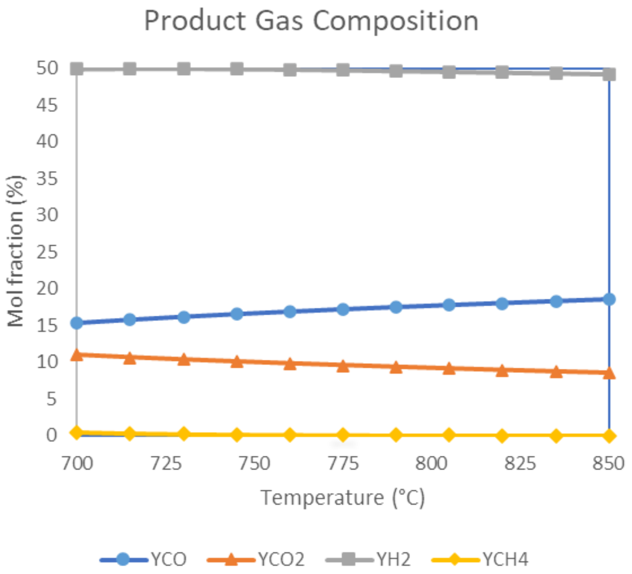

Figure 22. Product gas composition at ER=0.1 and SF=2.

4.2 Overall and individual Restricted equilibrium approach (REA)

In this section were applied the degrees of approach (ΔT): -100°C, -200°C and -300°C using the overall REA to the ER and SF combination identified in section 4.1 with the highest CCE, CGE, H_2 yield: ER=0.1 and SF=2. It was found that independently of the ER and SF combinations, the heat balance condition was accomplished in a shorter temperature range as the ΔT was increased, up to reaching a ΔT = -300°C where none of the combinations accomplished the heat balance condition. Table 17 shows the valid temperature range of each combinations applying the overall REA coded by the following color scale:

- Green cell: accomplishment of the heat balance condition along the entire temperature range.
- Yellow cell: accomplishment of the heat balance condition in a reduced temperature range.
- Red cell: the heat balance condition was not accomplished inside the temperature range.

Table 17. Valid temperature range applying the overall REA.

	Degree of approach (ΔT)		
Combinations	-100°C	-200°C	-300°C
ER= 0.1, SF=2	700-850°C	760-850°C	🟥
ER= 0.1, SF= 1	745-850°C	820-850°C	🟥
ER = 0.15, SF = 2	745-850°C	820-850°C	🟥

The only combination that accomplished the heat balance condition along the entire temperature range was ER=0.1 and SF= 2 at ΔT=-100°C. Figure 23 compares the product gas composition of the equilibrium approach (Figure 22) against the REA applying a ΔT =-100°C for the baseline case.

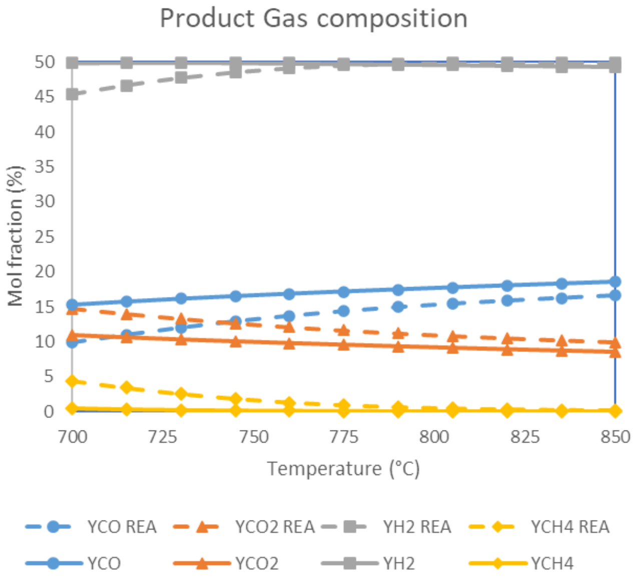

Figure 23. Product gas composition equilibrium approach (solid lines) vs REA ΔT=-100°C (dashed lines) at ER=0.1 and SF=2.

From Figure 23, the behavior of the different product gas composition obtained using the overall REA approach is the following:

- The YH_2 REA is slightly reduced at temperatures below 770°C, though above this temperature the compositions achieved by both approaches was the same.
- The YCH_4 REA content is gradually higher at temperatures below 770°C. The composition starts reducing above this temperature until reaching the equilibrium composition.
- The CO REA and CO_2 REA content were different from the equilibrium approach values through the entire temperature range. The CO REA was lower than the equilibrium approach whilst the CO_2 REA was higher. The tendency showed by both gases along the temperature range indicates that the REA allows the formation of more CO_2 at lower temperatures, though as the temperature increases, the CO and CO_2 shifted to the equilibrium compositions.
- The CCE and CGE were not affected by the REA getting a complete conversion as in the equilibrium approach.

Secondly, the individual REA was applied using only the combination that accomplished the heat balance condition along the temperature range (ER=0.1 and SF=2). The following reactions were considered for the individual REA model:

$$\text{WGS: } CO + H_2O \leftrightarrow CO_2 + H_2$$

$$\text{Methane reforming: } CH_4 + H_2O \rightarrow CO + 3\,H_2$$

$$\text{Char steam reforming: } C + H_2O \rightarrow CO + H_2$$

$$\text{Hydrogen combustion: } H_2 + \frac{1}{2}O_2 \rightarrow H_2O$$

The hydrogen combustion reaction was included in the individual REA to complete the simulator settings, but the reaction always had an individual ΔT=0°C. The rest of the reactions started the analysis with an individual ΔT= -100°C. Initially, the ΔT was applied per reaction. Next, the ΔT was applied in two reactions simultaneously, and finally, it was applied to the three reactions. After finishing the assessment, the ΔT was increased to -200°C, and the evaluation procedure was repeated. Table 18 and Table 19 show the different combinations of reactions applying an individual ΔT=-100°C and ΔT=-200°C, respectively. The green cells indicate the accomplishment of the heat balance condition through the entire temperature range (700-50°C), whereas the yellow cell determine the reduced temperature range where the IHBFBSR model accomplished the heat balance condition.

At ΔT=-100°C, all combinations in Table 18 accomplished the heat balance condition for the entire temperature range, indicating that at this ΔT there is no difference between applying the individual or overall REA for the ER=0.1 and SF=2 case (Table 17). Similarly to the overall REA, in the individual REA at ΔT=-200°C (Table 19), the valid temperature range reduced from 700°C to 745/775°C depending on the combination of reactions, showing that applying the individual REA has an impact of ±15°C compared to the overall REA.

Table 18. Combination of reactions applying the individual REA at ΔT=-100°C, ER=0.1 and SF= 2. The green cells indicate the valid temperature range.

ER=0.1 SF=2 ΔT=-100°C				
None	**WGS**	**Char Steam Reforming**	**Methane Reforming**	**All**
WGS	700-850°C	700-850°C	700-850°C	
Char Steam Reforming	700-850°C	700-850°C	700-850°C	
Methane Reforming	700-850°C	700-850°C	700-850°C	
All				700-850°C

Table 19. Combination of reactions applying the individual REA at ΔT=-200°C, ER=0.1 and SF= 2. The yellow cells indicate the reduced temperature range where the heat balance condition was accomplished.

ER=0.1 SF=2 ΔT=-200°C				
None	**WGS**	**Char Steam Reforming**	**Methane Reforming**	**All**
WGS	700-850°C	745- 850°C	775- 850°C	
Char Steam Reforming	745-850°C	745- 850°C	775-850°C	
Methane Reforming	775-850°C	775-850°C	775-850°C	
All				775-850°C

By only applying the degree of approach to the WGS reaction, the model accomplished the heat balance condition for the whole temperature range. This characteristic can lead to a misuse of the individual REA as it was possible to satisfy the heat balance condition even at unrealistic values as ΔT=-800°C where the CO content is practically zero.

Finally, two different types of degree of approach were applied simultaneously, a ΔT=-100°C for methane and char steam reforming and ΔT=-200°C for the WGS reaction. The following behavior of the product gas composition, CCE and CGE was identified:

- The WGS reaction is the best option to adjust specifically the CO and CO_2 content because of the equilibrium behavior of this reaction. Furthermore, the H_2 and CH_4 content are slightly modified by this reaction. Nevertheless, without experimental data, its manipulation can lead to unrealistic values.
- By combining the WGS with another reaction like CH_4 or char steam reforming, the degree of approach for the second reaction must be lower and keeping a minimum difference of 100°C between both degrees of approach to accomplish the heat balance condition. However, the results from the individual REA assessment, indicates that at ΔT=-200°C, the CH_4 steam reforming reduces the valid temperature range, then the degree of approach for this reaction cannot go away from this value.
- By applying a degree of approach to the three reactions simultaneously, the value cannot be lower than -100°C. At this degree of approach, the change in the product gas composition compared to the equilibrium approach is negligible for H_2 and CH_4, then the feasibility of using this degree of approach either in the overall or individual REA is questionable.

For all the combinations shown in Table 19, the char steam reforming is the only one that affects the CCE. Thus, this reaction can serve to describe systems without a complete CCE as in the case of the PW-DKR350 mixture gasification.

In conclusion, this method is a trial-and-error process that can be useful to fit a simulation to experimental results with the aim to identify which reactions limit each case. Nevertheless, its application in the inverse way to identify suitable operating conditions is not advisable, thus the overall and individual REA were not considered in further sections.

4.3 Equilibrium approach including PSD

The CCE, CGE, H_2 yield, CO yield, GY and CO_2 yield were tested after including the PSD mesh in the Aspen Plus model using the following assumptions for the combination ER=0.1 and SF=2 in the temperature range 700-850°C, the analyses only applied the equilibrium approach:

- feedstock (0-6 mm) average diameter 4 mm, standard deviation 0.5 mm
- Enabling the PSD model "constant number of particles" in the DRYER, PYRO and GASIFIER blocks.

Figure 24 indicates that including a PSD mesh for the feedstock and the PSD model did not affect the product gas composition compared to the equilibrium composition determined in section 4.1. Later, were varied the average particle diameter from 1-5 mm without showing changes either. Finally, the PSD model was changed to "constant PSD" getting the same product gas composition.

During the assessment of the two PSD models, the lower limit of the PSD mesh was modified from 1 to 0 mm regarding that this approach achieves a CCE equals to 100%. As consequence, it was needed to adjust the average particle diameter and standard deviation to 4 mm and 0.5 mm respectively. It was found a direct correlation between the standard deviation and the PSD mesh limits. As the standard deviation increased, the PSD mesh needed to get larger and vice versa to always keep the cumulative weight equals to one. Otherwise, the simulator normalizes the weight fractions through the PSD giving incorrect particle diameters. Nevertheless, the normalization of the weight distribution performed by Aspen Plus did not affect the product gas composition.

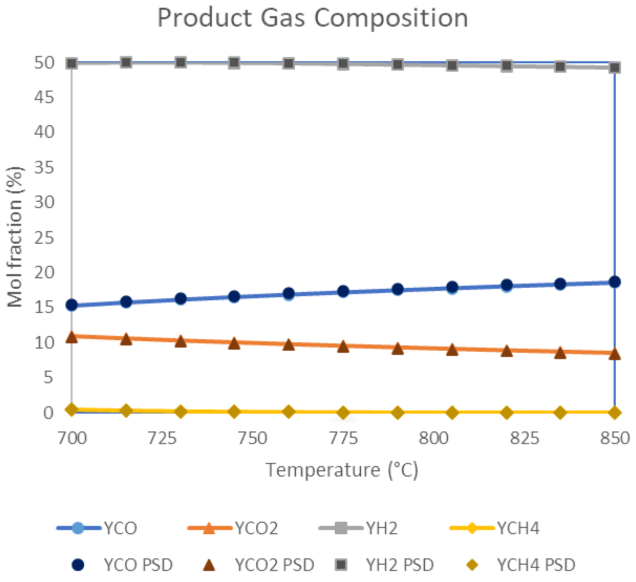

Figure 24. Product gas composition calculated by equilibrium approach without PSD (solid lines) and with PSD model constant number of particles (dark markers).

The PSD model keeping the constant number of particles will be used in further sections because there is not data indicating the presence of channels inside the feedstock particles and no intraparticle phenomena (heat and mass transfer limitations) were included in the IHBFBSR model.

Finally, Figure 25 shows that applying the PSD model constant PSD, the size of the ashes is larger than in the constant number of particles which can lead to an over dimensioning of the separation equipment downstream the IHBFBSR. It will be expected that in kinetic models, the unreacted char particles will follow the same tendency.

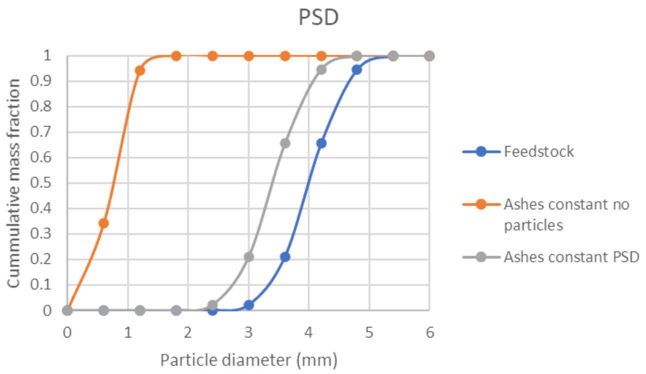

Figure 25. PSD of the feedstock and ashes applying the two PSD models

4.4 Equilibrium approach including pyrolysis correlations

The IHBFBSR model was solved by only applying the equilibrium approach to the combination ER=0.1 and SF=2. The importance of this sections was developing the pyrolysis correlations to enable the analysis of the tar content in the mixture. Therefore, the indicators CCE, CGE and GY are divided in three categories to describe the component distribution of the gasification products:

- Permanent gases (PG): H_2, CO, CO_2, CH_4.
- Light hydrocarbons (LHC):C2-C5.
- Tar: single, double and triple rings.

Secondly, regarding the benefit of using the TY indicator to verify if the chosen ER and SF combination maximizes the CCE, CGE, H_2 and CO content while minimizes the tar content in the product gas. The TY indicator will have a higher priority in the assessment of the IHBFBSR model including the tar compounds as follows:

$$\text{CCE} > \text{CGE} > H_2 \text{ yield} > \text{CO yield} > \text{TY} > \text{GY} > CH_4 \text{ yield} > CO_2 \text{ yield}$$

As was mentioned in the Methodology section, some pyrolysis products must be considered as inerts to avoid achieving the same product gas composition than in the equilibrium approach (section 4.1). Due to the absence of experimental data related to the content of specific compounds, there were proposed two combinations of inert fractions to show the effect of including the pyrolysis correlations in the IHBFBSR model:

A) 100% of the triple ring compounds ($C_{12}H_8$ and $C_{14}H_{10}$). This situation can occur at the maximum operating temperature of the IHBFBSR (<850°C) because of the high stability of their polycyclic configuration [16].
   100% of the triple ring compounds ($C_{12}H_8$ and $C_{14}H_{10}$), 50% of $C_{10}H_8$ and 20% of single ring compounds and the monomers C_2H_4 and C_3H_6. Taking as reference the content of the pyrolysis products determined by the correlations and the gasification products reported by Wilk and Hofbauer [31].

The product gas composition of the two combinations is plotted together with the values from the equilibrium approach in Figure 26. The inert fraction for each compound was adjusted manually to accomplish the heat balance condition along the entire temperature range 700-850°C.

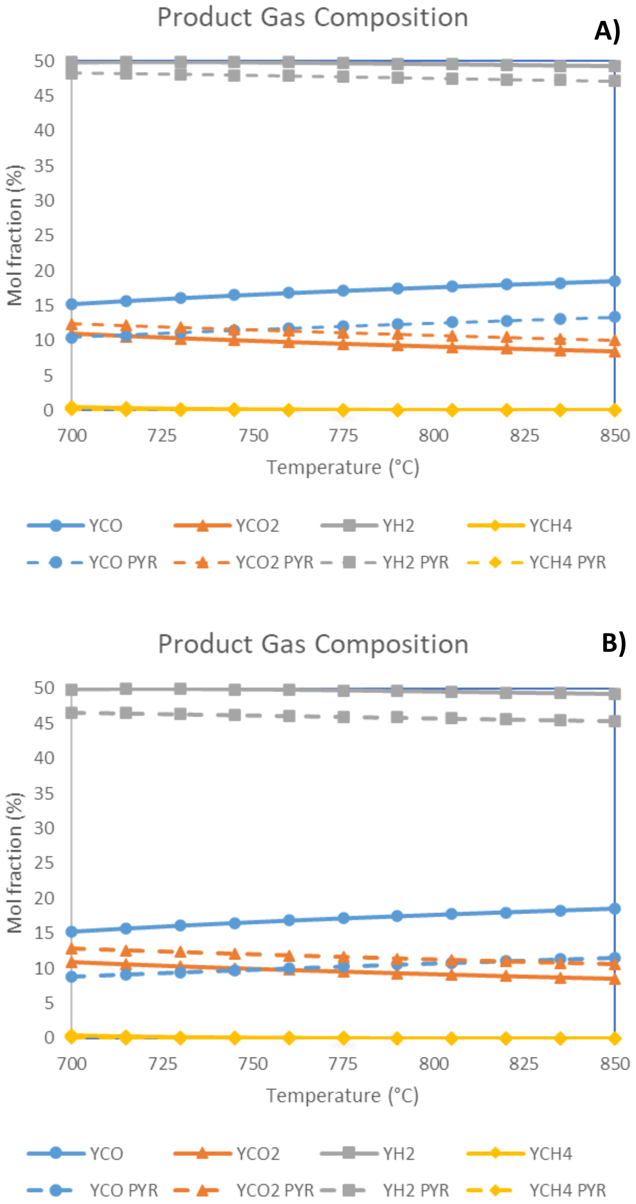

Figure 26. Product gas composition calculated by the equilibrium approach in Figure 22 (solid lines) and product gas composition after including the pyrolysis correlations with the combination A) and B) of inert fractions (dashed lines) at ER=0.1 and SF= 2.

In Figure 26-A, the biggest difference between both product gas composition is the CO PYR content reduced in a 4%, the H_2 PYR and CO_2 PYR content were modified a 2% and the CH_4 PYR was not modified compared to the equilibrium compositions. On the other hand, Figure 26-B shows a lower H_2 PYR and CO PYR content than the equilibrium approach (5% and 6% respectively), while the CO_2 PYR and CH_4 PYR remained equal to Figure 26-A. Nevertheless, after testing different combinations of inert compounds to accomplish the heat balance condition along the temperature range, it was concluded that this trial-and-error procedure leads to the same situation that the overall and individual REA. The equilibrium approach including pyrolysis correlations is an alternative to adjust simulation data to experimental values, tough it must be discarded to determine optimal operating conditions.

4.5 Comparison of equilibrium approach models

Table 20 summarizes the findings of the different upgrading strategies to the IHBFBSR model according to the equilibrium approach:

Table 20. Summary of the equilibrium IHBFBSR models at each phase.

Strategy	Modeling Approach	Advantages	Disadvantages
I	Equilibrium Approach	• Non-stoichiometric approach • Simple settings requirements.	• The CCE and CGE is complete which are unrealistic values. • The H_2 and CO content is overestimate. • The CO_2 and CH_4 content are underestimate. • It does not consider the formation of LHC and tar.
	Restricted Equilibrium Approach (REA)	• The degree of approach can be applied individually to a group of reactions to adjust the simulation to experimental data. • Identify which reactions can limited the whole gasification process.	• The overall REA (below -200°C) does not modify the GY and CCE. • Identifying the participating reactions and their individual degree of approach turn it into an exhaustive trial and error process. • It does not consider the formation of LHC and tar.
II	Including PSD	• Nonvisible advantage	• Same than Equilibrium approach
III	Pyrolysis correlations	• Includes the formation of LHC and tar. • The GY, CCE and CGE values get closer to experimental data. • Inclusion of the TY as an auxiliar tool.	• The pyrolysis correlations are only valid inside a specific range of operating conditions and sample composition. • Risk of overestimate /underestimate the content of a pyrolysis product. • Risk of select incorrectly a lumped tar compound. • Setting inert compounds and their fraction becomes an exhaustive trial and error procedure.

4.6 Kinetic approach using Fluidbed block

This kinetic strategy using the Fluidbed block required the following adjustments to solve the convergence problems:

1) The tar compounds were by-passed from the bed zone, returning to the IHBFBSR at the height of minimum fluidization conditions (H_{mf}) determined by equation (22). This assumption was based on the later formation of these compounds through the IHBFBSR [16].
2) The number of cells was increased up to 40 for the bed and freeboard zones respectively. The number of cells for both zones was increased simultaneously setting the convergence tolerance to $1x10^{-15}$ and 1000 iterations for each one (Figure 27).

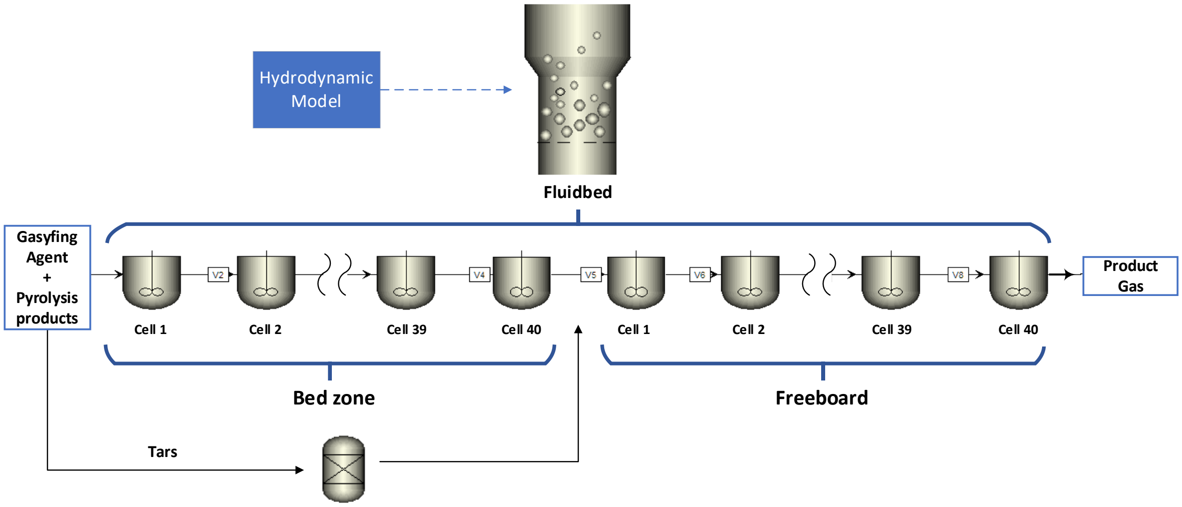

Figure 27. Final configuration of the kinetic model including the Fluidbed block. The blue block indicates the calculator block coupled to determine the minimum fluidization conditions. The tar compounds are bypassed from the bed zone returning to the IHBFBSR at the beginning of the freeboard.

In this section, the number of ER and SF combinations reviewed inside the temperature range 700-850°C was limited to values around the best combination identified by the equilibrium approach in section 4.1 (ER=0.1 and SF=2) that accomplish the heat balance condition to study the effect of varying the ER and SF ratios:

- ER= 0.05, SF = 1
- ER= 0.05, SF = 3
- ER= 0.1, SF = 1
- ER= 0.1, SF = 3
- ER= 0.15, SF = 2
- ER= 0.15, SF = 3

Figure 28 includes the plots of the H_2 yield (A), CO yield (B), TY (C), GY (D), CH_4 yield (E), and CO_2 yield (F) at the different ER and SF combinations. Meanwhile, the CCE and CGE indicators were not used to evaluate the ER and SF combinations because of all of them achieved values above 80% (PG+LHC+TAR) and 40% (PG+LHC) respectively.

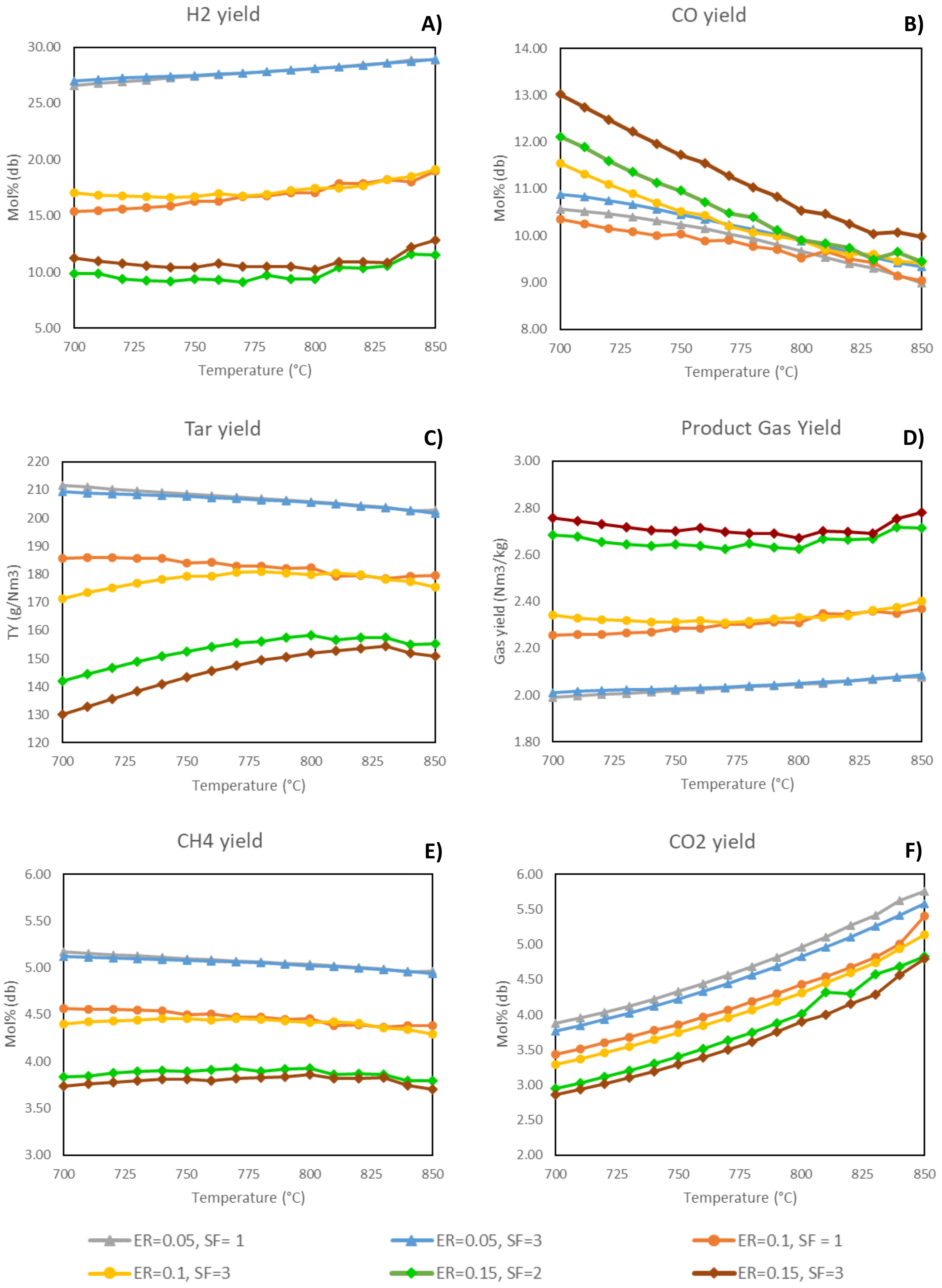

Figure 28. Indicators H_2 yield (A), CO yield (B), TY (C), GY (D), CH_4 yield (E), CO_2 yield (F) at different combinations of ER and SF determined by the kinetic approach using the Fluidbed block.

The plots in Figure 28 show that the ER is the parameter that governs the performance of the six indicators, while the effect of varying the SF parameter only gets visible in combinations using an ER=0.15. Besides, there is a reduction of the 50% (average) for the H_2, CO and CO_2 content after including the kinetic expressions, while the CH_4 content increased to the double (average) in all the combinations compared to the equilibrium compositions (Figure 21). Nevertheless, above 800°C the model showed convergence problems for the combinations using the ER=0.1 and 0.15, highlighting the necessity of using an advanced kinetic model.

In the H_2 yield plot (Figure 28-A), at 850°C, there is a considerable reduction of the H_2 content as soon as the ER increases, going from a 35% at ER=0.05 and SF=3 (Figure 28, blue line) to 17% at ER=0.15 and SF=3 (Figure 28, brown line). The reduction of almost 20% derives from the enhancement of the H_2 combustion reaction over the rest of oxidation reactions. Meanwhile, its generation, controlled by the WGS reaction, is an indirect process that requires of a higher SF ratio to mitigate the fast H_2 consumption [57].

In the Fluidbed model, the indicators CO and CO_2 yield (Figure 28-B and D) are showing an opposite trend to the equilibrium compositions calculated in section 4.1. Whereas in the equilibrium indicators (Figure 21) the CO content increases with the temperature and reduces with the ER, in the Fluidbed block, the CO yield reduces with the temperature. This behavior derives from the CO combustion, which is superimposing to the WGS and partial oxidation reactions of LHC and tar. Therefore, the kinetics of the Fluidbed block is controlled by the enhancement of the H_2 and CO combustion reactions which can lead to underestimate the H_2 and CO content .

Regarding to the TY plot (Figure 28-C), the combinations with ER=0.05 (gray and blue lines) showed the highest TY (average 205 g/ Nm^3) while at ER=0.15 (green and brown lines) the average TY was 140 g/ Nm^3 because at higher ER values, there is enough O_2 in the Fluibed block to enable the partial oxidation reactions of tar at the moment they returned to the IHBFBSR (Figure 27).

4.7 Kinetic approach using the CSTR-PFR blocks

In this strategy, the Fluidbed block was replaced by the CSTR and PFR blocks to describe the bed zone and freeboard. Initially, the bed zone was modeled by one CSTR block based on the findings from previous studies [55] [62]. However, this model showed convergence problems that were solved by dividing the bed zone in 10 CSTRs and modifying the reaction packages included in each block and coupling a calculator block to each CSTR block to determine the hydrodynamic properties, equations (13) to (25) in section 3.1.6, using the properties from the outlet stream of the previous block (Figure 29).

The number of CSTRs was sequentially increased following a trial-and-error procedure once that the CSTR block showed convergence problems after adding a reaction package. The distribution of the reaction packages along the ten CSTRs and the PFR is given in Table 21. Nevertheless, the number of CSTR blocks was limited to ten, taking as a reference the initial configuration of the Fluidbed block, there was no intention to check the effect of adding more CSTRs to the model due to the absence of a reference study to justify further modifications. The convergence tolerance of each CSTR was settled at $1x10^{-15}$ and 1000 iterations, while for the PFR was $1x10^{-6}$ and 200 iterations.

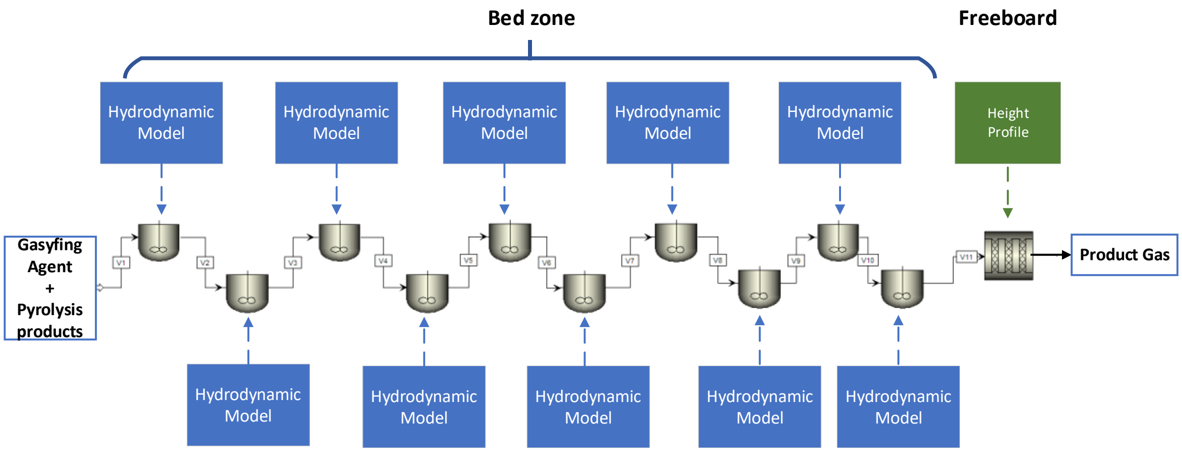

Figure 29. Final configuration of the kinetic model using the CSTR-PFR blocks. The blue blocks indicate the calculator blocks coupled to each CSTR to determine the hydrodynamics, while the green block indicates the calculator block for the change of diameter along the freeboard (Table 15).

Table 21. Distribution of the reaction packages in the CSTRs-PFR model. Green cells indicate the reaction package included in the block.

Configuration	**Heterogenous reactions**	**Homogenous reactions**	**WGS**	**LHC (C2-C5)**	**MAH (C6-C8)**	**PAH (C10)**
CSTR 1 bed	🟩	🟩	🟩	🟩		
CSTR 2 bed	🟩	🟩	🟩	🟩		
CSTR 3 bed	🟩	🟩	🟩	🟩		
CSTR 4 bed	🟩	🟩	🟩	🟩		
CSTR 5 bed	🟩	🟩	🟩	🟩		
CSTR 6 bed	🟩	🟩	🟩	🟩	🟩	🟩
CSTR 7 bed	🟩	🟩	🟩	🟩	🟩	🟩
CSTR 8 bed	🟩	🟩	🟩	🟩	🟩	🟩
CSTR 9 bed	🟩	🟩	🟩	🟩	🟩	🟩
CSTR 10 bed	🟩	🟩	🟩	🟩	🟩	🟩
PFR freeboard		🟩	🟩	🟩	🟩	🟩

Finally, the separator block used for bypassing the tar compounds from the bed zone was removed from this model because it was not more necessary to disable the PAH and MAH reaction packages in the first CSTRs blocks (1-5) of bed zone as in the Fluidbed model.

The sensitivity analyses were done applying the same combinations of ER and SF ratios in the Fluidbed model for comparison reasons. Figure 30 shows the H_2 yield (A), CO yield (B), GY (C), TY (D), CH_4 yield (E) and CO_2 yield (F) inside the temperature range 700-850°C. Besides, the CCE and CGE indicators were not used to evaluate the different combinations of SF and ER because of all of them achieved values above 90% (PPG+LHC+TAR) and 40% (PG+LHC) respectively.

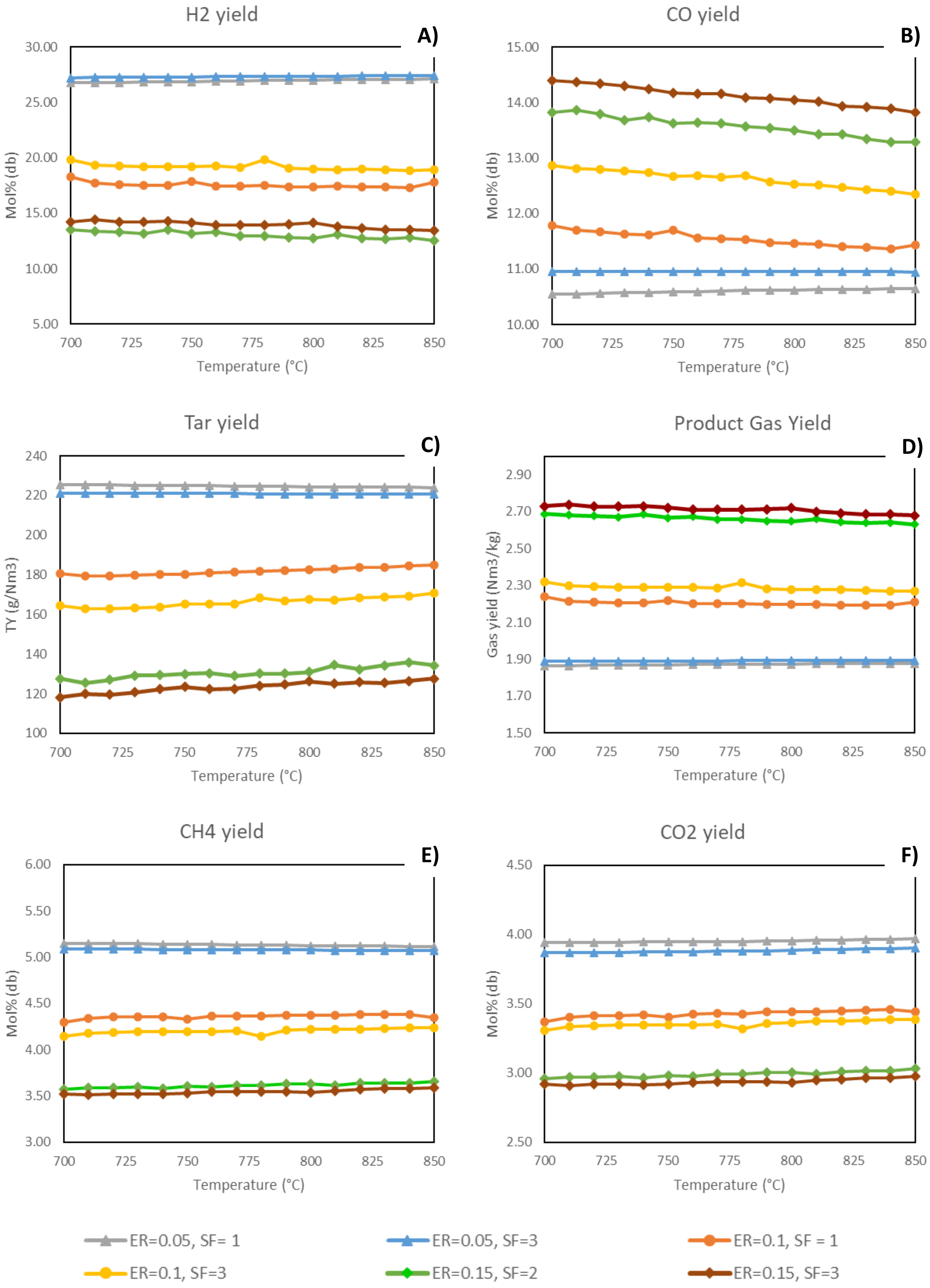

Figure 30. Indicators H_2 yield (A), CO yield (B), TY (C), GY (D), CH_4 yield (E), CO_2 yield (F) at different combinations of ER and SF determined by the kinetic approach using ten CSTR-and one PFR.

Firstly, the six plots in Figure 30 show the advantage of modifying the distribution of the reaction packages along the bed zone as the convergence problems above 800°C were solved. Besides, it is possible to follow the trend of each combination in function of the ER, while the effect of varying the SF ratio is minimum (2% average) along the temperature range.

The H_2 yield plot (Figure 30-A) shows that the H_2 content was increased at ER=0.1 and ER=0.15 (green and brown lines respectively) in a 2% and 4% (average), respectively compared to the Fluidbed model. Derived by enabling the tar cracking reactions at early stages of the bed zone and specifying the freeboard as an adiabatic reactor to enhancing the tar cracking and WGS reactions.

The CO and CO_2 yield plots (Figure 30-B and Figure 30-F) show the most noticeable change in their trend compared to the Fluidbed model. The CSTRs-PFR model determines a smaller slope for the CO and CO_2 content at each ER and SF combination inside the temperature range, thus the CO content was higher in this model for all the ER and SF combinations due to enabling the tar cracking reactions at the middle of the bed zone (6th CSTR).

Finally, the TY plot (Figure 30-C), supported by the increase of the H_2 and CO content, denotes the necessity of increasing the ER from 0.1 to 0.15 to reduce the tar content in a 22% (average), while the SF=2 can be kept it because increasing its value from 2 to 3, the effect on the six indicators was negligible (2% average).

4.8 Kinetic approach using the two-phase model (TPM)

The bed zone is modeled by a reactor network of four CSTR-PFR pairs to describe the emulsion and bubble phase and two calculator blocks, to solve the TPM correlations and redistribute the component flows, described in Figure 31.

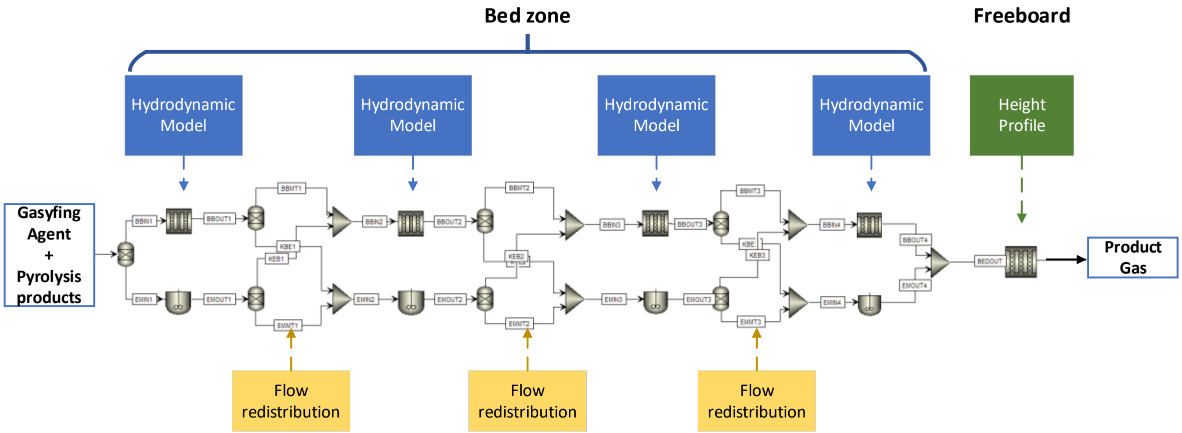

Figure 31. Final configuration of the kinetic model including the two-phase model. The blue blocks indicate the calculator blocks coupled to each pair determine the TPM hydrodynamics, yellow blocks are the calculator blocks for the flow redistribution and the green block indicates the calculator block for the change of diameter along the freeboard (Table 15).

The number of pairs was limited to four, based on the Literature Study findings [89] [66] [86]. Similarly to the CSTRs-PFR model, the TPM model required to modify the distribution of the reaction packages proposed in the Methodology chapter, section 3.1.7, by disabling the MAH and PAH reaction packages in the emulsion phase as is shown in Table 22.

Table 22. Distribution of the reaction packages in the TPM model. Green cells indicate the reaction package included in the block.

Configuration	**Heterogenous reactions**	**CO comb**	**H_2 comb**	**WGS**	**LHC (C2-C5)**	**MAH (C6-C8)**	**PAH (C10)**
CSTR 1 emulsion	🟩		🟩	🟩			
PFR 1 bubble		🟩	🟩	🟩	🟩	🟩	🟩
CSTR 2 emulsion	🟩		🟩	🟩	🟩		
PFR 2 bubble		🟩	🟩	🟩	🟩	🟩	🟩
CSTR 3 emulsion	🟩		🟩	🟩	🟩	🟩	
PFR 3 bubble		🟩	🟩	🟩	🟩	🟩	🟩
CSTR 4 emulsion	🟩		🟩	🟩	🟩	🟩	
PFR 4 bubble		🟩	🟩	🟩	🟩	🟩	🟩
PFR freeboard		🟩	🟩	🟩	🟩	🟩	🟩

Finally, the sensitivity analyses were done repeating the combinations of ER and SF from the sections 4.6 and 4.7. Figure 32 shows the H_2 yield (A), CO yield (B), TY (C), GY (D) CH_4 yield (E), and CO_2 yield (F). The plots from the CCE and CGE indicators were excluded of the assessment because all the combinations achieved values above 93% (PG+LHC+TAR) and 40% (PG+LHC) respectively.

As in the CSTR-PFR model, the TPM model showed a stable trend of the H_2 yield, TY, GY, CH_4 yield indicators. Indeed, the CO and CO_2 yield plots (Figure 32 B and F) are not only showing the stable trend, but also describe the effect of restricting the CO combustion reaction to the bubble phase by getting the highest CO_2 content, while the high CO content comes from enabling the MAH and PAH reactions packages in all the bubble phase reactors. Besides, at ER=0.15 (green and brown lines) the trend of the CO and CO_2 switch to an increasing and decreasing trend with the temperature (respectively) due to the enhancement of the tar cracking reactions over the CO combustion reaction.

The TPM has the highest H_2 yield (Figure 32-A) among the three kinetic models for the combinations using the ER = 0.1 and ER= 0.15 (yellow, orange, green and brown lines) derived by enabling the MAH and PAH reactions packages at the bottom of the IHBFBSR, then the O_2 consumption is not anymore controlled by the H_2 and CO combustion reactions as it was happening in the Fluidbed model. However, as the temperature increase the H_2 yield reduces (2% average) for all the ER combinations due to the enhancement of the H_2 combustion reaction.

Finally, the TY plot (Figure 32-F) is not only showing the lowest values among the three kinetic models, but also that for the ER values 0.05 and 0.1 (gray, blue, yellow and orange lines) the tar content increases with the temperature, because of the enhancement of the CO combustion reaction by the temperature, while at ER=0.15 the trend is stable inside the temperature range(Figure 32-F, brown and green lines). Then this situation supports the statement from section 4.7 about increasing the ER to 0.15.

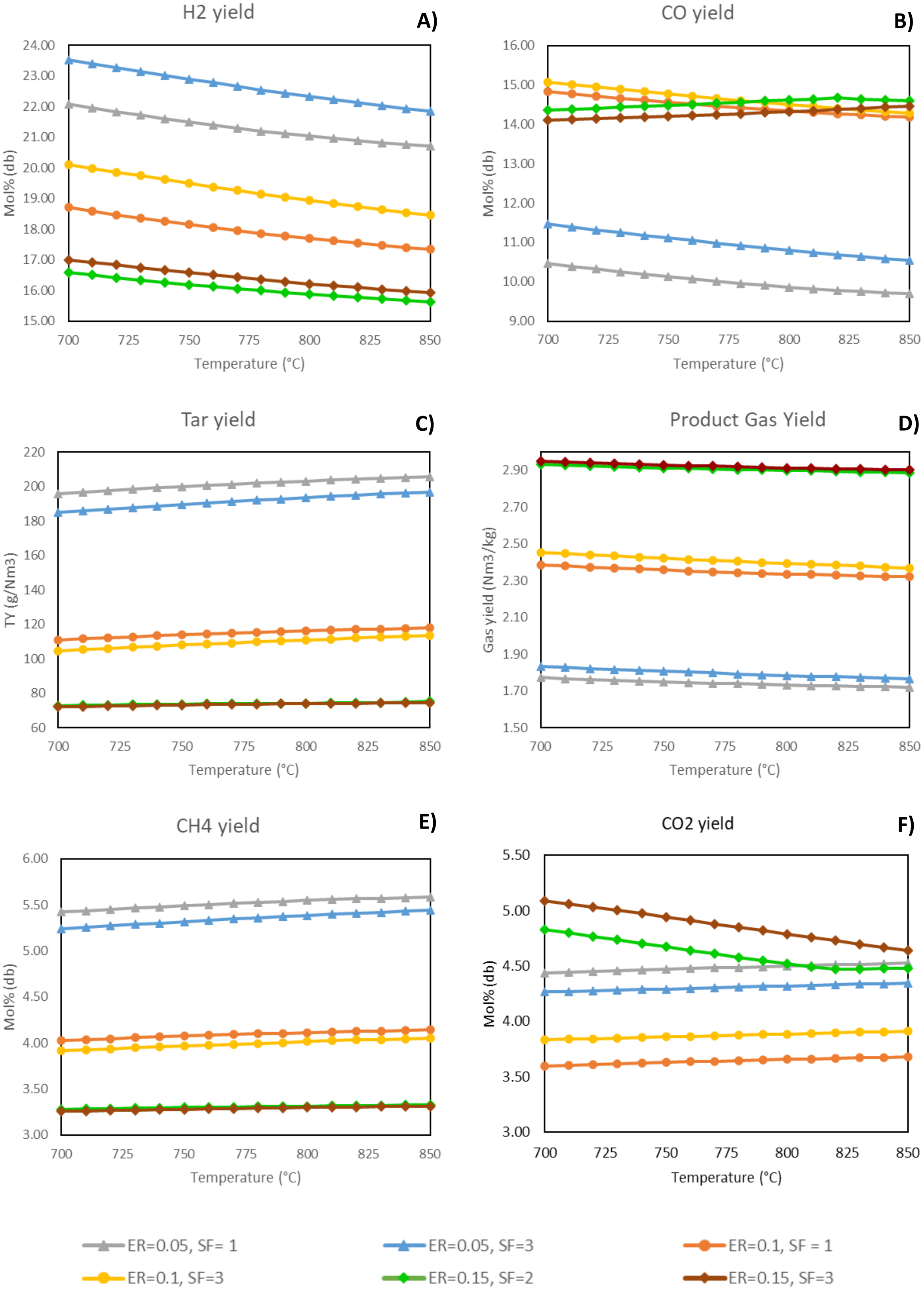

Figure 32. Indicators H_2 yield (A), CO yield (B), TY (C), GY (D), CH_4 yield (E), CO_2 yield (F) at different combinations of ER and SF determined by the kinetic approach using the two-phase model.

4.9 Comparison of the kinetic approach models

This section compares the three kinetic models: Fluidbed, CSTRs-PFR and TPM. The three models are compared in Figure 33 regarding to the O_2 content (A), H_2O content (B), H_2 content (C), CO content (D), CH_4 content (E), CO_2 content (F), and temperature (G) profiles along the IHBFBSR. This comparison aims to analyze the effect of the three hydrodynamic models and the individual settings in the composition of the permanent gases. The assessment is done using the parameters ER=0.15, SF=2 and T = 750°C.

In the previous sections (4.6-4.8), the combination ER=0.15 and SF=2 was identified as the optimal value to reduce the tar content, while the temperature was reduced at 750°C, to achieved a higher H_2 content regarding the trend described by the TPM.

Firstly, the O_2 profile of the Fluidbed block (Figure 33-A, gray line) shows the fastest O_2 consumption reflecting the advantage of using a higher number of blocks to describe the bed zone (40 CSTRs) at difference to the CSTRs-PFR model, which only includes 10 CSTRs and required to disable reaction packages at the first CSTRs blocks (1-6), showing the slowest O_2 consumption (blue line). However, the O_2 consumption in the Fluidbed block was controlled by the H_2 combustion, getting the highest H_2O content and the lowest H_2 content at the outlet of the IHBFBSR (Figure 33-B and C, gray line). On the contrary, the slower O_2 consumption in the CSTRs-PFR model, achieved intermediate values for the H_2, CO, CH_4 and H_2O content among the three kinetic models (Figure 33, blue lines).

The TPM achieved the highest H_2 and CO content (Figure 33-C and D, orange lines), derived by enabling the MAH and PAH reaction packages in the bubble phase and the restriction on the CO combustion only occurring in the bubble phase getting the highest CO_2 content (Figure 33-H, orange line).

Finally, the temperature profiles from the TPM and the CSTRs-PFR model were equal (Figure 33-C and G, blue and orange lines) showing the effect of modeling the freeboard as an adiabatic PFR block, though there is not a clear effect of setting the Freeboard block as adiabatic yet.

Table 23 gives a summary of the three kinetic models developed in section 4.6-4.8 for the IHBFBSR. The criteria are oriented to the differences between the hydrodynamic models and the kinetics of the reactions in the indicators CCE, CGE, H_2 yield, CO yield, TY, GY, CH_4 yield, and CO_2 yield.

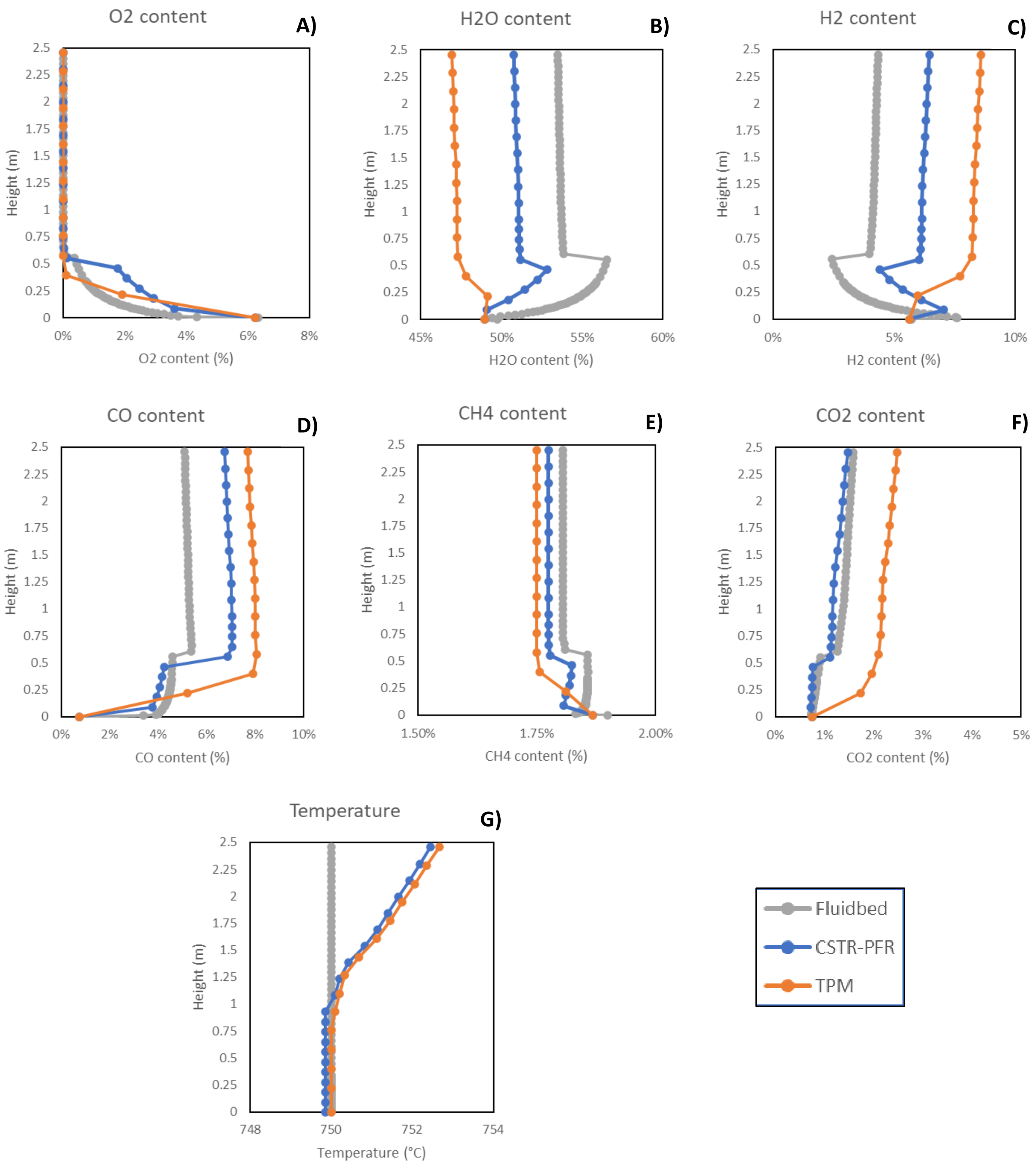

Figure 33. Profiles of the O_2 content (A), H_2O content (B), H_2 content (C), CO content (D), CH_4 content (E), CO2 content (F), temperature (G) along the IHBFBSR determined by the three kinetic models at ER=0.15, SF=2 and Temperature=750°C (wet basis).

Table 23. Summary of the settings for the hydrodynamics models applied for the IHBFBSR.

Characteristic	Fluidbed model	CSTR-PFR model	Two-phase model
IHBFBSR model	• Decomposes the IHBFBSR in the (1) bed zone, (2) transport disengagement and (3) freeboard	• Decomposes the IHBFBSR in the (1) bed zone and (2) freeboard	• Decomposes the IHBFBSR in the (1) bed zone and (2) freeboard. The bed zone is subdivided in the (1A) bubble and (1B) emulsion phases.
Hydrodynamics			
Bed zone model	• The bed zone has a homogenous phase with bubble growth according to Werther model for Geldart B particles.	• The bed zone has a homogenous phase. • The emulsion phase is at minimum fluidization conditions.	• The bed zone is decomposed in bubble and emulsion phase: ○ The velocity and voidage of the emulsion phase is higher than the minimum fluidization conditions. ○ The bubble phase has presence of solids.
Bed expansion	• Applies correlations for Geldart B particles.	• Determined by the Babu expansion coefficient (ref).	• Determined by the Babu expansion coefficient.
Transport disengagement model	• George & Grace model (ref).	• Assumes complete separation of the bed material at the end of the bed zone.	• Assumes complete separation of the bed material at the end of the bed zone.
Elutriation model	• Colakyan & Levenspiel model for Geldart B particles	• Assumes complete separation of the bed material at the end of the bed zone.	• Assumes complete separation of the bed material at the end of the bed zone.
Freeboard model	• Isothermal with presence of solids according to Kuni & Levenspiel model. • The diameter varies with the height.	• Adiabatic and free of solids. • The diameter varies with the height.	• Adiabatic and free of solids. • The diameter varies with the height.

Table 24. Summary of the results from the kinetic models of the IHBFBSR.

Characteristics	**Fluidbed model**	**CSTRs-PFR model**	**Two-phase model**
Kinetics			
Blocks configuration	• One Fluidbed block composed by 40 CSTR blocks for the bed zone and freeboard respectively.	• 10 CSTR blocks for the bed zone. • One PFR block for the freeboard.	• Bed zone described by four pairs of CSTR-PFR blocks for the emulsion and bubble phase, respectively. • One PFR block for the freeboard.
Reaction kinetics	• Consider that all the reactions are happening in each CSTR.	• Distributes the reactions in six packages for the bed zone and freeboard.	• Distributes the reaction in seven packages for the two phases of the bed zone and freeboard.
CCE	• Values above 93% (PG+LHC+TAR) for all the ER and SF combinations.	• Values above 93% (PG+LHC+TAR) for all the ER and SF combinations.	• Values above 93% (PG+LHC+TAR) for all the ER and SF combinations.
CGE	• Values above 38% (PG+LHC) for all the ER and SF combinations.	• Values above 44% (PG+LHC) for all the ER and SF combinations.	• Values above 55% (PG+LHC) for all the ER and SF combinations.
H_2 yield	• Lowest H2 yield for all the ER and SF combinations.	•	• Highest H_2 yield for all the ER and SF combinations.
CO yield	• Lowest CO yield for all the ER and SF combinations.	• -	• Highest CO yield for all the ER and SF combinations.
TY	• -	• Highest TY for all the ER and SF combinations	• Lowest TY for all the ER and SF combinations
GY	•	• Lowest GY for all the ER and SF combinations	• Highest GY for all the ER and SF combinations
CH_4 yield	• Highest CH_4 yield for all the ER and SF combinations	• -	• Lowest CH_4 yield for all the ER and SF combinations
CO_2 yield	•	• Lowest CO_2 yield for all the ER and SF combinations	• Highest CO_2 yield for all the ER and SF combinations.

4.10 Validation cases

In this section, the six gasification models developed through sections 4.1-4.8 are applied to describe two experimental works found during the Literature Study. The six gasification models used for the validation cases are:

- **Equilibrium approach:**
  - Chemical Equilibrium approach (EA).
  - Individual Restrict Chemical Equilibrium approach (INDREA).
  - Chemical Equilibrium approach including pyrolysis correlations (PYRC).
- **Kinetic approach:**
  - Fluidbed model (FBED).
  - CSTRs-PFR model (CSTRs-PFR).
  - Two-phase model (TPM).

The PSD model was not included in this section because it did not show any modification on the key performance indicators respect to the equilibrium model (section 4.3).

At the moment that this study was developed, there is not experimental work about the gasification of a polyolefins waste with a composition that meets the DKR350 specification using an air-steam mixture as gasifying agent. However, it was proposed a selection criterion (Table 25) with the minimum requirements to choose a validation case in the Literature. The adjustments needed per each validation case are described in further subsections.

Table 25. Criteria for the selection of the validation cases

Criterion	Value	
Gasifier type	Bubbling Fluidized Bed	
Heating system	Autothermal/allothermal	
Bed material	Silica sand	
Dimensions	Mandatory: Bed diameter Gasifier height Freeboard diameter	Optional: Distribution plate sizes
Feedstock	PE is the major component	
Gasifying agent	Air and/or steam	
Proximate analysis	Moisture < 5%	Fixed Carbon < 10%
Ultimate analysis	N content < 1% Cl content < 1%	S content < 1% O content < 10%
HHV fuel	> 30 MJ/kg	

The assessment of each gasifier model is based on the relative error determined for each indicator with respect to the experimental data, equation (45).

$$error = \frac{|val_{exp} - val_{calc}|}{val_{exp}} \tag{45}$$

4.10.1 Case 1 Air Gasification of Polyolefins in a BFB

The first validation case comprises the design of a bubbling fluidized bed gasifier for the air gasification of a polyolefin mixture composed only by PE and PP. The gasifier has a total height of 1.2 m, the diameter of the bed zones is 8 cm while the diameter of the freeboard zone, starting at 0.7 m is 13 cm. The complete experimental data was taken from "Design and first experimental results of a bubbling fluidized bed for air gasification of plastic waste "by Martinez-Lera et al. [87], Table 26.

Table 26. Gasification input data for validation case 1.

Criterion	**Value**	
Gasifier type	Bubbling Fluidized Bed	
Heating system	Autothermal	
Bed temperature	750°C	
Bed material	Silica sand Bed inventory: 1.4 kg ρ_p: 2650 kg/m^3 dp: 550 µm	
Dimensions	Mandatory: Bed diameter: 0.08 m Bed height: 0.7 m Freeboard diameter: 0.13 m Freeboard height: 0.5 m	Optional: Distribution plate sizes: Number of nozzles: 12 Inlet Nozzle diameter: 2 mm Outlet nozzle diameter: 0.5 mm Secondary air stream at 0.5 m
Feedstock	Polyolefins (PE+PP) Flow: 0.5- kg/h dp: 1-4 mm	
Gasifying agent	Air ER: 0.2-0.4	
Proximate analysis	Moisture = 0% Ash = 0.1 %	Fixed Carbon = 0.9% Volatile matter = 99%
Ultimate analysis	C = 82.1 % H = 14.2 % S = 0.02 %	N = 2.2 % O = 1.5%
HHV fuel	40.44 MJ/kg	

All the information in Table 26 was available in the work from Martinez Lera et al. [87], except for the proximate analysis data that was taken from Wilk et al. [32], who also studied the gasification of PE+PP mixtures and the temperature of the air preheater, then it was decided to use the same temperature than in the IHBFBSR model (650°C). As consequence the design specs to accomplish the heat balance condition were disabled in the six models.

The sensitivity analyses were done varying the ER parameter at 0.25, 0.3 and 0.35, constant temperature of 750°C. The indicators: CCE (A), CGE (B), H_2 yield (C), CO yield (D), TY (E), GY (F), CH_4 yield (G) and CO_2 yield (H) from each gasifier model were plotted together against the experimental data in Figure 34.

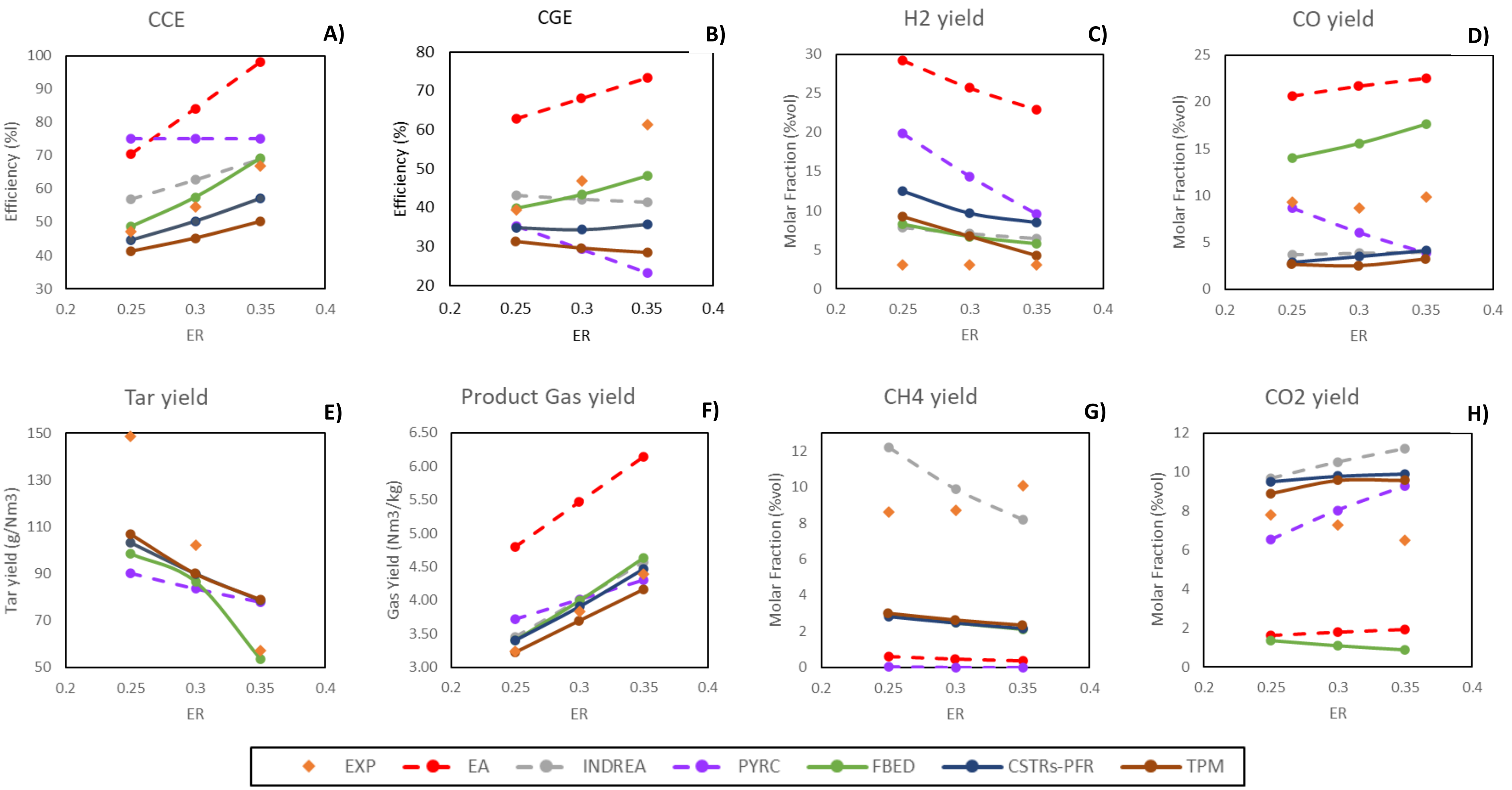

Figure 34. Indicators CCE(A), CGE (B), H_2 yield (C), and CO yield (D), TY (E), GY (F), CH_4 yield (G), and CO_2 yield (H) from the three equilibrium models (dashed lines), three kinetic models (solid lines) and the experimental values (rhomb orange markers) from the validation case [87].

Regarding the Equilibrium approach models, the values determined by the equilibrium model (Figure 34, red lines) show the overestimation of the CCE, CGE, H_2 yield, CO yield and GY, and underestimation of the CH_4 yield and CO_2 yield, being in agreement with the findings from the Literature Study and the evaluation done in section 4.1. Meanwhile, the INDREA model (Figure 34, gray lines) shows the effect of applying the individual REA to mitigate the relative error on the seven indicators, although it was not capable to fit all the values (regarding that the TY cannot be determined by this approach due to the limitations of the calculation method by the RGibbs block). Besides, the INDREA model was the only model (among the equilibrium and kinetic approaches) that determines the lowest error on the CH_4 content (12% average). This was achieved by applying the following combination of degrees of approach:

- Water gas shift: -50°C
- Char steam gasification: -250°C
- Steam methane reforming: -300°C

On the contrary, the PYRC model (Figure 34, purple lines) the only equilibrium approach model including the pyrolysis correlations, was the worst alternative to adjust the calculated parameters to the experimental data. The reason is the specification of inert fractions for specific compounds in the RGibbs block as these values are constant for all the ER values, as seen in the CCE plot (Figure 34-A), where the PYRC model is the only one achieving a constant CCE. This situation leads to unreliable values like the CGE, CO and CO_2 yield plots, which show opposite trends to the rest of indicators (Figure 34-A, D and H).

Among the three kinetic models, the FBED model (Figure 34, green line) shows the best agreement of the CCE and CGE indicators, getting a relative error of 4% (average) and 9% (average), respectively, although the model fails in determining the CO, CO_2 and CH_4 content; especially, the CO_2 plot (Figure 34-H) shows a lower CO_2 content than the equilibrium values (red line) that cannot be possible by the thermodynamics. This situation comes from the application of the pyrolysis correlations, developed in the Methodology section 3.1.4, to describe the PW mixture of the validation case, which has a higher C content and an absence of Cl atoms, proving the limitations of the correlations by the feedstock composition, also the Fluidbed block cannot describe correctly the H_2 and CO kinetics because as the ER increases, the kinetics of the partial oxidation reactions of LHC and tar do it too, imposing to the H_2 and CO combustion (differing from the discussion in section 4.9), leading to overestimate the H_2 and CO content for every ER value.

Meanwhile, the CSTRs-PFR (blue lines) and TPM (brown lines) models, which are also using the same pyrolysis correlations than the FBED model, showed a higher error for the CCE of 9% and 18% (respectively), getting more notorious at ER=0.35 (Figure 34-A). Furthermore, the CGE trends of each model (Figure 34-B, blue and brown lines) are not increasing in function of the ER as the experimental data, they instead behaved constant for the three ER values. This situation is related to the kinetic expressions included for the tar compounds which are not enough to describe the experimental TY values (Figure 34-E).

Furthermore, it was necessary to redistribute the reaction packages of the CSTRs-PFR and TPM models in the bed zone, proposed in Table 34 and Table 35 (sections 4.7 and 4.8), to solve the convergence problems and reduce the relative error of the eight indicators, turning this situation into a trial-error procedure to adjust both models to the experimental data. However, none of the models was capable of describing accurately the experimental data (below 10% of relative error). The new distribution of the reaction packages for both models is included in Appendix section 8.5.

After modifying the reaction packages in the CSTRs-PFR and TPM models, they showed similar values for the CO yield, CO_2 yield, TY and GY indicators and inside the limits of the EA values (red lines) meaning that both models mitigated the error introduced by the pyrolysis correlations. The difference between them relies on the H_2 yield plot (Figure 34-C), being the TPM determined who determined the lowest error among the six indicators (though still is doubling the H_2 content). Nevertheless, the plots in Figure 34 show up the advantage of having developed two easy adjustable models to describe the behave of the eight indicators, although they still require an improvement on their tar kinetics models, additionally to reviewing the applicability of the pyrolysis correlations for a specific case.

4.10.2 Case 2 Air Gasification of Recycled Plastic in a BFB

In this validation case was modeled the air gasification of recycled plastic, composed mainly by PE and PP, in a bubbling fluidized bed gasifier of constant diameter (10 cm) and total height of 2.5 m. The experimental data was taken from "Fluidized-Bed Gasification of Plastic Waste, Wood, and their Blends with Coal" by Zaccariello & Mastellone [88], Table 27.

Table 27. Gasification input data for validation case 2.

Criterion	Value	
Gasifier type	Bubbling Fluidized Bed	
Heating system	Autothermal	
Bed temperature	877°C	
Bed material	Silica sand Bed inventory: 3.2 kg ρ_p: 2600 kg/m^3 dp: 250 µm	
Dimensions	Mandatory: Bed diameter: 0.1 m Gasifier height: 1.2 m	Optional: Distribution plate sizes: Number of nozzles: 3 Inlet Nozzle diameter: 5 mm Outlet nozzle diameter: Secondary air stream at 0.9 m height
Feedstock	Recycled plastic (PE + PP + others) Flow= 1.08 kg/h dp= 15-20 mm	
Gasifying agent	Air ER= 0.25 T_{inlet}=790°C	
N_2	F_{N2} = 0.32 kg/h	
Proximate analysis	Moisture = 0.67% Ash = 1.94 %	Fixed Carbon = 2.89% Volatile matter = 94.5%
Ultimate analysis	C = 79.54 % H = 13.06 % S = 0.08 %	N = 0.18 % O = 4.53 %
HHV fuel	42.69 MJ/kg	

In this validation case was enabled the two design specs to accomplish the heat balance condition. Besides, this case was chosen because its proximate and ultimate analyses are similar to the PW-DKR350 mixture, although there was not enough information to run the sensitivity analyses. Figure

35 summarizes the relative error of each gasifier model against the experimental data of the eight indicators (CCE, CGE, H_2 yield, CO yield, TY, GY, CH_4 yield, and CO_2 yield) at ER=0.25 and T=877°C.

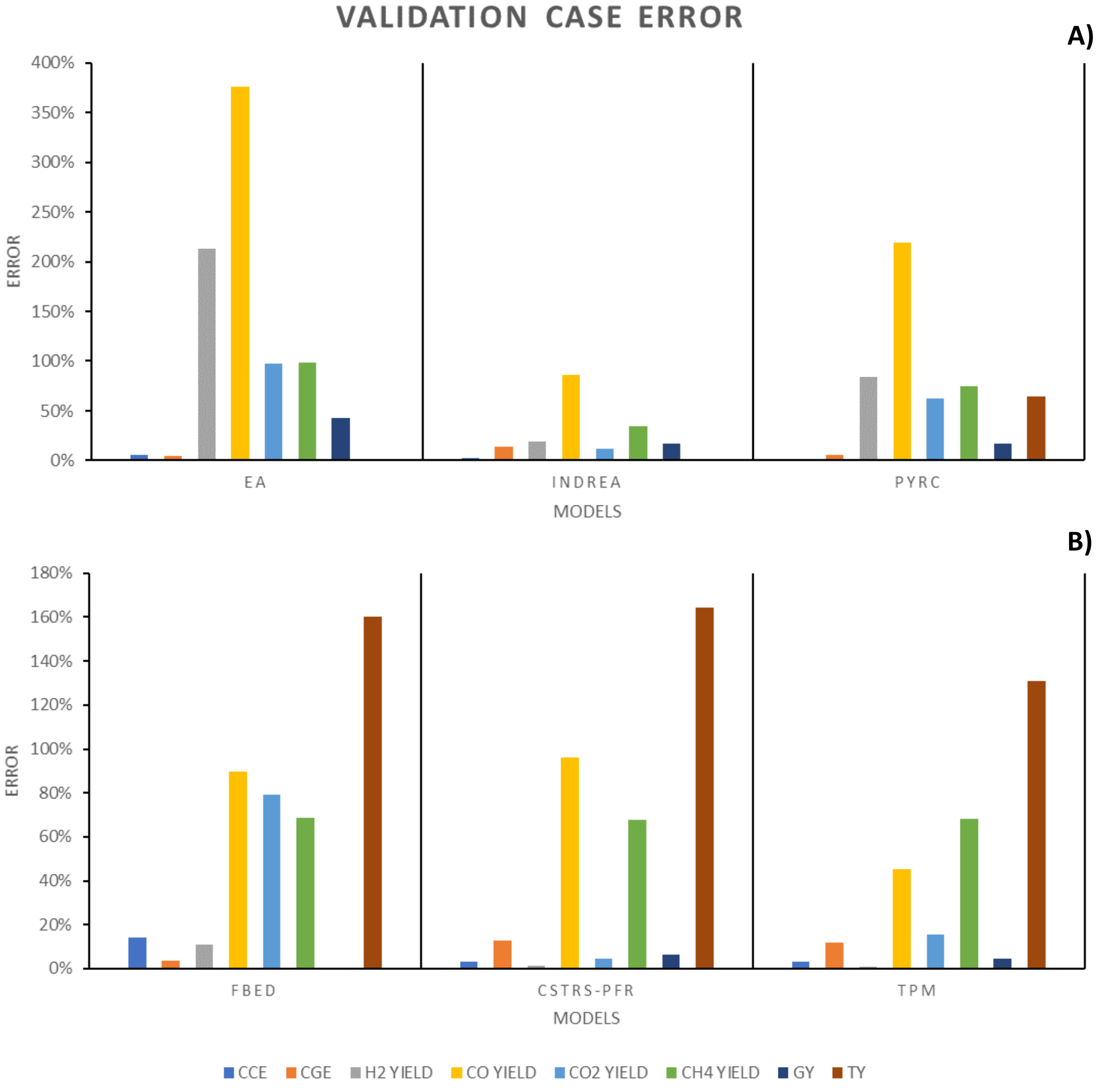

Figure 35. Summary of the relative error of the equilibrium models (A) and the kientic models (B) at ER=0.25 and T=877°C.

The similarities in the feedstock composition of both mixtures are visible in the error achieved in the CCE and CGE indicators for the six gasifier models (below 10% and 15%, respectively), especially for the kinetic models supporting the use of the pyrolysis correlations in this case to describe the feedstock. (Figure 35, blue and orange bar, respectively) Besides, in the case of the CGE error (orange bar), it was expected a better agreement to the experimental data because the expression to calculate the HHV of the feedstock (equation (10)) was taken from this work, although in the validation case the LHV of all the permanent gases and light hydrocarbons were estimated by equation (10) whilst in the gasifier models the LHVs were taken from the Aspen plus database, the difference is not attributed to the calculation method but to the error in the CO, CH_4 and tar content of the PYRC, FBED, CSTRs-PFR, and TPM models (Figure 35, green and brown bars).

As in the previous validation case, any of the six models could fit the eight indicators to the experimental data (Figure 35). Nevertheless, the outcome from this assessment was the reduction of the error in the eight indicators from the EA model, which overestimates the H_2 content (200%), CO content (370%) and GY (43%) to the TPM with a lower error in the H_2 content (1%), CO content (45%), and GY (5%).

For the equilibrium approach models (INDREA and PYRC), they achieved a lower error compared to the EA model, although the reduction required to applying different degrees of approach (INDREA) and inert fractions (PYRC model) than in the previous validation case, remarking the exhaustive trial-and-error procedure to follow in both modeling approaches without adjusting accurately the experimental data. One more time, the INDREA looks like a better alternative to adapt an equilibrium model to experimental data, despite it does not consider the formation of heavier hydrocarbons (LHC and tar compounds). Meanwhile, the PYRC model got the lowest error in the TY among all the models (including the kinetics). Besides, the inert fractions proposed to solve this model are limited to a specific temperature and ER, it was identified that aiming to reduce the TY error, the error in the H_2, CO and CO_2 content was increased due to the solution method applied by the RGibbs (Figure 35-A).

In the kinetic approach models, only the CSTRs-PFR model required to modify the distribution of the reaction packages to reduce the error in the eight indicators. The redistribution consisted of enabling more reaction packages in the first CSTR blocks (1-6). Meanwhile, the TPM showed the lowest error among the six gasifier models for the eight indicators (Figure 35-B), using the same distribution proposed in the validation case 1. Besides, the TPM got the lowest error on the CO content (45%) due to the constrain on the CO combustion reaction in the bed zone. The distribution of the reaction packages for this validation case is shown in Appendix Table 35.

Nevertheless, this validation case confirms the necessity of enlarging the list of reactions to describe the formation of CH_4 and other light hydrocarbons (C2-C5) from the reforming of tar compounds, because eve after solving the convergence problems through the kinetic approach, the CH_4 content determined by the TPM is still underestimated, while the tar content is almost two times the experimental data.

5 Conclusions

This thesis describes the development of a detailed model in Aspen plus to simulate the gasification of a polyolefins waste mixture, representative of the packaging sector in agreement to the DKR 350 specification (PW-DKR350). This model comprises the gasification kinetics and bed hydrodynamics using the two-phase theory (TPM), of a novel Indirectly Heated Bubbling Fluidized Bed Steam Reformer (IHBFBSR). The IHBFBSR was designed, built and commissioned by the Dutch company Petrogas-Gas Systems in collaboration with the Process and Energy Department of the Delft University of Technology [6]. The TPM-IHBFBSR model developed in this work will serve as an auxiliar tool to validate the experimental work developed as part of the project "Towards improved circularity of polyolefin-based packaging" and narrow down the number of tests by identifying the gasification parameters (temperature, ER, SF ratios) that optimize the key performance indicators (KPI): CCE, CGE, GY and TY [5].

The development of the TPM-IHBFBSR model followed a three-stages process. A literature review of the most-used modeling approaches and identification of the reference data to propose a baseline model. Next, the implementation of the upgrading strategies in the model according to the equilibrium and kinetic approaches, evaluating each upgrading strategy (focus on solving the convergence problems). Finally, the evaluation of the TPM-IHBFBSR model and previous versions, using two validation cases found in the literature, to identify the advantages and limitations of the model.

The identification of the gasification parameters that optimizes the KPIs required to divide the main research question to address the role of each gasification parameter and feedstock characteristics.

1) What is the optimal gasification temperature to maximize the CCE, CGE, and GY with the lowest TY?

   The results of the IHBFBSR model indicate that increasing the temperature of the gasifier has a negative effect on the H_2 content of 2% (average) for all the ER and SF combinations. Whereas for other indicators like CCE, CO content, GY and TY, the benefit was negligible (below 1%). Considering that H_2 is the most valuable compound in the product gas, the gasification temperature should be below 800°C (50 degrees below the maximum operating temperature) to minimize the reduction of the H_2 content. On the contrary, the minimum gasification temperature required by the model is 680°C (20 degrees below the minimum temperature reviewed) due to the valid temperature range of the pyrolysis correlations developed in section 3.1.4.

2) What is the optimal ratio of the gasifying agents to maximize the CCE, CGE, GY with the lowest TY?

   Using the equilibrium model was identified that the ER ratio controls the performance of the IHBFBSR and is key on computing the final value of the KPIs. On the other hand, the increase of the SF ratio serves to increase the H_2 content despite a reduction of the CO content, being the SF=1 and SF=2 values which achieved the highest H_2 content, 45% and 50% (average), inside the temperature range 700-850°C. Nevertheless, the equilibrium approach does not consider the tar content, overestimating the H_2 and CO content, then the combination ER=0.1 and SF=2 was identified as the combination which achieved the highest CCE, CGE, GY and H_2 content and served as the setpoint to evaluate the kinetic models.

During the assessment of the kinetic models (Fluidbed, CSTRs-PFR and TPM) was identified the necessity of increasing the ER value to 0.15, keeping SF=2 to reduce the average tar content in 22% inside the temperature range 700-850°C, despite reducing the H_2 and CO content due to the enhancement of the H_2 and CO combustion reactions at the bottom of the IHBFBSR.

3) What is the optimal particle diameter and size distribution of the feedstock to maximize the CCE, CGE, GY, with the lowest TY?

   One of the limitations identified during the development of the equilibrium and kinetic IHBFBSR models, was the negligible effect of the particle diameter and size distribution (PSD) of the feedstock and solids products (char and ashes) on the CCE, CGE, GY, and TY, inside the particle diameter range proposed, 1-6 mm. Nevertheless, the PSD option remained enabled in the models because of the future integration of the model with the downstream separation equipment section, which requires this information.

4) What is the effect of the feedstock composition on the CCE, CGE, GY, and TY?

   During the development of the pyrolysis correlations in section 3.1.4, was reviewed the major effect of each polymeric component in the pyrolysis products, these findings can be addressed to the KPIs as follows:

   - A higher content of PE and PP in the PW mixture, increases the CCE, CGE and GY, reducing the TY.
   - A higher content of PS in the PW mixture increases the TY, reducing the CGE and GY.
   - A higher content of PET in the PW mixture, reduces the CCE and increase the TY.
   - A higher content of PVC in the PW mixture reduces the CCE and increase the TY.
   - A higher content of organic waste or metals reduces the CCE.

   Indeed, the differences in the content of the impurities (PET, PVC, organic waste/metals), arises the necessity of proposing a series of strategies to mitigate the differences in the composition between the reference PW mixture [77] and the PW-DKR350, limiting the application of the pyrolysis correlations to other PW mixtures. For instance, during the first validation case (section 4.10.1) was shown how these differences in the feedstock composition lead to unreliable values of the KPIs.

6 Recommendations

A computational program is never finished, it is closer to be replaced by a faster and/or more accurate software before achieved the ultimate version dreamed by its original developer. The developed of the TPM-IHBFBSR model to assess the KPIs of gasification is the final product of this Thesis. Nevertheless, the identification of the upgrading strategies during these months are the most valuable outcome to continue improving the program. The list of most important tasks to complete in the future is given below (based on the author believes):

- Compare the TPM-IHBFBSR model results against the experimental data from the gasification of the PW-DKR350 mixture. Quantifying the differences between the KPIs of the model and the experimental work will allow to evaluate the modelling strategy proposed in this Thesis and proposed further improvements.
- Use the pyroprobes data to develop a new set of correlations for the permanent gases, light hydrocarbons and tar, implement them into the pyrolyser script of the TPM-IHBFBSR model and verify their influence in the overall results of the model.
- Include the experimental data of the particle size distribution from the feedstock, char and ashes. This information is crucial for the selection and design of the separation equipment downstream.
- Enlarge the list of reactions with their kinetic expressions for the cracking and reforming of larger hydrocarbons to form CH_4 and other lighter hydrocarbons.
- Evaluate the effect of increasing the number of CSTR-PFR pairs of the TPM-IHBFBSR model in the reduction of the relative error after including the new set of pyrolysis correlations and larger set ok kinetic expressions

7 Bibliography

[1] Dutch Government, "A Circular Economy in the Netherlands by 2050," The Ministry of Infrastructure and the Environment and the Ministry of Economic Affairs, The Hague, 2016.

[2] Netherlands Institute for Sustainable Packaging , "Chemical recycling of plastic packaging materials, Analysis and Opportunities," The Hague, 2018.

[3] O. Dogu, M. Pelucchi and R. V. d. Vijver, "The chemistry of chemical recycling of solid plastic waste via pyrolysis and gasification: State-of-the-art, challenges, and future directions," *Progress in Energy and Combustion Science,* vol. 84, 2021.

[4] Plastics Europe, "Plastics – the Facts 2019 An analysis of European plastics production, demand and waste data," Brussels, 2019.

[5] Institute for Sustainable Process Technology, "Towards improved circularity of polyolefin-based packaging," 2020.

[6] C. Tsekos, M. d. Grosso and W. d. Jong, "Gasification of woody biomass in a novel indirectly heated bubbling fluidized bed steam reformer," *Fuel Process Technology,* vol. 224, 2021.

[7] Plastics Europe, "Plastics 2030 - Voluntary Commitment," Brussels, 2018.

[8] Ministry of Infrastructure and Water Management, "From Waste to Resources," 2017. [Online]. Available: https://rwsenvironment.eu/subjects/from-waste-resources/. [Accessed 2020].

[9] J. Woidasky, "Plastics Recycling," in *Ullman's Encyclopedia of Industrial Chemistry*, Germany, Wiey Sons, 2020.

[10] Plastics Europe Netherlands, "Roadmap towards increasing the sustainability of plastics packaging," The Hague, 2018.

[11] S. Ghosh, "Gas Cleaning and Tar Conversion in Biomass Gasification," in *Coal and Biomass Gasification*, Singapore, Springer, 2018.

[12] R. Thomson, P. Kwong and E. Ahmad, "Clean syngas from small commercial biomass gasifiers; a review of gasifier development, recent advances and performance evaluation," *International Journal of hydrogen energy,* vol. 45, pp. 21087-21111, 2020.

[13] S. Kersten and W. d. Jong, "Thermochemical conversion: (co)gasification and hydrothermal gasification," in *Biomass as a Sustainable Energy Source for the Future*, Wiley Sons, 2015, pp. 298-358.

[14] S.A.Salaudeen, P.Arku and A. Dutta, "Gasification of Plastic Solid Waste and Competitive Technologies," in *Plastics to Energy*, William Andrew Applied Science Publishers, 2019, pp. 269-293.

[15] P. Kannan, A. A. Shoaibi and C. Srinivasakannan, "Energy recovery from co-gasification of waste polyethylene and polyethylene terephthalate blends," *Computers & Fluids,* vol. 88, pp. 38-42, 2013.

[16] G. Lopez, M. Artetxe and M. Amutio, "Recent advances in the gasification of waste plastics. A critical overview," *Renewable and Sustainable Energy Reviews,* vol. 82, pp. 576-596, 2018.

[17] C. Liu, Y. Huang and M. Niu, "Influences of equivalence ratio, oxygen concentration and fluidization velocity on the characteristics of oxygen-enriched gasification products from biomass in a pilot-scale fluidized bed," *International Journal of Hydrogen Energy,* vol. 43, no. 31, pp. 14214-14225, 2018.

[18] CE Delft, "Exploration of chemical recycling- update 2019," Delft, 2019.

[19] S. You, Y. S. Ok and D. C. W. Tsang, "Towards practical application of gasification: a critical review from syngas and biochar perspectives," *Critical Reviews in Environmental Science and Technology,* vol. 48, no. 22-24, pp. 1165-1213, 2018.

[20] T. B. Vilches, J. Marinkovic and M. Seemann, "Comparing Active Bed Materials in a Dual Fluidized Bed Biomass Gasifier: Olivine, Bauxite, Quartz-Sand, and Ilmenite," *Energy Fuels,* vol. 30, no. 6, pp. 4848-4857, 2016.

[21] S. Bhaskaran, S. Gupta and S. De, "Dual Fluidized Bed Gasification of Solid Fuels," in *Coal and Biomass Gasification*, Singapore, Springer, 2017, pp. 425-454.

[22] P. Basu, "Design of Biomass Gasifiers," in *Biomass Gasification, Pyrolysis and Torrefaction*, Academic Press, 2013, pp. 249-313.

[23] H. V. C.M. van der Meijden, "Scale-up of the biomass gasification technology," energy Research Center of the Netherlands, Petten, 2009.

[24] CORDIS European Comission, "Biomass heatpipe reformer (BioHPR)," July 2005. [Online]. Available: https://cordis.europa.eu/project/id/ENK5-CT-2000-00311. [Accessed 01 december 2020].

[25] J. Karl and T. Pröll, "Steam gasification of biomass in dual fluidized bed gasifiers: A review," *Renewable and Sustainable Energy Reviews ,* vol. 98, pp. 64-78, 2018.

[26] J. Bermudez and B. Fidalgo, "Production of bio-syngas and bio-hydrogen via gasification," in *Handbook of Biofuels Production*, Woodhead Publishing, 2016, pp. 431-494.

[27] M. Kwakkenbos, Kinetic Modelling of Biomass Gasification in an Indirectly Heated Bubbling Fluidized Bed Steam Reformer, Delft: TU Delft, 2020.

[28] B. R. Reddy and R. Vinu, "Feedstock Characterization for Pyrolysis and Gasification," in *Coal and Biomass Gasification*, Singapur, Springer, 2018, pp. 3-36.

[29] M. Roosen, N. Mys and M. Kusenberg, "Detailed Analysis of the Composition of Selected Plastic Packaging Waste Products and Its Implications for Mechanical and Thermochemical Recycling," *Enviromental Science and Technology,* vol. 54, pp. 13282-13293, 2020.

[30] E.Ranzi, T.Faravelli and F.Manenti, "Pyrolysis, Gasification, and Combustion of Solid Fuels," in *Advances in Chemical Engineering*, vol. 49, London, American Press, 2016, pp. 1-94.

[31] V.Wilk and H.Hofbauer, "Conversion of mixed plastic wastes in a dual fluidized bed steam gasifier," *Fuel,* vol. 107, pp. 787-799, 2013.

[32] V. Wilk and H. Hofbauer, "Co-gasification of Plastics and Biomass in a Dual Fluidized-Bed Steam Gasifier: Possible Interactions of Fuels," *Energy and Fuels,* vol. 27, no. 6, pp. 3261-3273, 2013.

[33] I. Ahmed, N. Nipattummakul and A. Gupta, "Characteristics of syngas from co-gasification of polyethylene and woodchips," *Applied Energy,* vol. 88, no. 1, pp. 165-174, 2011.

[34] K. R. G. Burra and A. K. Gupta, "Nonlinear Synergistic Effects in Thermochemical Co-processing of Wastes for Sustainable Energy," in *Innovations in Sustainable Energy and Cleaner Environment*, Singapore, Springer, 2020, pp. 117-148.

[35] M.-H. Cho, Y.-K. Choi and J.-S. Kim, "Air gasification of PVC (polyvinyl chloride)-containing plastic waste in a two-stage gasifier using Ca-based additives and Ni-loaded activated carbon for the production of clean and hydrogen-rich producer gas," *Energy,* vol. 87, pp. 586-593, 2015.

[36] S. Y. Tao Zhou and Y. Wei, "Impact of wide particle size distribution on the gasification," *Renewable Energy,* vol. 148, pp. 534-547, 2020.

[37] DKR-Der Grüne Punkt, "Product Specification 04/2009- Mixed Plastics," Deutsche Gesellschaft für Kunststoff-Recycling mbH , Köln, 2009.

[38] Y. Du, H. Liu and W. Ren, "Numerical Investigations of a Fluidized Bed Biomass Gasifier Coupling Detailed Tar Generation and Conversion Kinetics with Particle-Scale Hydrodynamics," *energy and Fuels,* vol. 34, pp. 8440-8451, 2020.

[39] R. Moreira, R. Vaz and A. Portugal, "Gasification of Charcoal in Air, Oxygen, and Steam Mixtures over a γ-Al2O3 Fluidized Bed," *energy and fuels,* vol. 32, pp. 406-415, 2018.

[40] F. Menga, Q. Maa and H. Wanga, "Effect of gasifying agents on sawdust gasification in a novel pilot scale bubbling fluidized bed system," *Fuel,* vol. 249, pp. 112-118, 2019.

[41] M. K. Karmakar, C. Loha and S. De, "Hydrodynamics of Circulating Fludized Bed Systems," in *Coal and Biomass Gasification*, Singapore, Springer , 2018, pp. 92-114.

[42] D. Geldart, "Types of gas fluidization," *Powder Technology,* vol. 7, pp. 285-292, 1973.

[43] M. W. Islam, "A review of dolomite catalyst for biomass gasification tar removal," *Fuel,* vol. 267, 2020.

[44] A. Soomro, S. Chen and S. Ma, "Catalytic activities of nickel, dolomite, and olivine for tar removal and H2-enriched gas production in biomass gasification process," *energy and Environment,* vol. 29, no. 6, pp. 839-867, 2018.

[45] H. L. Zhub, Y. S. Zhanga and M. Materazzia, "Co-gasification of beech-wood and polyethylene in a fluidized-bed reactor," *Fuel Processing Technology,* vol. 190, pp. 29-37, 2019.

[46] A. Farooq, H. Song and Y.-K. Park, "Effects of different Al2O3 support on HDPE gasification for enhanced hydrogen generation using Ni-based catalysts," *International Journal of Hydrogen Energy,* 2020.

[47] K.Göransson, U.Söderlind and P.Engstrand, "An experimental study on catalytic bed materials in a biomass dual fluidised bed gasifier," *Renewable Energy ,* vol. 81, pp. 251-261, 2015.

[48] E. Kumar, A. Bhatnagar and W. Hogland, "Interaction of anionic pollutants with Al-based adsorbents in aqueous media – A review," *Chemical Engineering Journal ,* vol. 241, pp. 443-456, 2014.

[49] A. K. Verma, Process Modelling and Simulation in Chemical, Biochemical and Environmental Engineering, Florida: CRC Press, 2015.

[50] O. C. Mutlu and T. Zeng, "Challenges and Opportunities of Modeling Biomass Gasification in Aspen Plus: a review," *Chemical engineering and Technology,* vol. 43, no. 9, pp. 1674-1689, 2020.

[51] P. Kannan, A. A. Shoaibi and C. Srinivasakannan, "Optimization of Waste Plastics Gasification Process Using Aspen plus," in *Gasification for practical applications*, Rijeka, Intech, 2012, pp. 278-296.

[52] A. Ahmed and A. Salmiaton, "Review of kinetic and equilibrium concepts for biomass tar modeling by using Aspen Plus," *Renewable and Sustainable Energy Reviews,* vol. 52, pp. 1623-1644, 2015.

[53] L. Abdelouahed, O. Authier and G. Mauviel, "Detailed Modeling of Biomass Gasification in Dual Fluidized Bed Reactors under Aspen Plus," *energy and fuels,* vol. 26, pp. 3840-3855, 2012.

[54] N. Deng, D. LI and Q. Zhang, "Simulation analysis of municipal solid waste pyrolysis and gasification based on Aspen plus," *Frontiers in Energy,* vol. 13, pp. 64-70, 2019.

[55] P. Kaushal and R. Tyagi, "Advanced simulation of biomass gasification in a fluidized bed reactor using aspen plus," *Renewable Energy,* vol. 101, pp. 629-636, 2017.

[56] A. Gomez-Barea and B. Leckner, "Modeling of biomass gasification in fluidized bed," *Progress in Energy and Combustion Science,* vol. 36, pp. 444-509, 2010.

[57] D. Mallick, B. Buragohain and P. Mahanta, "Gasification of Mixed Biomass: Analysis Using Equilibrium, Semi-equilibrium, and Kinetic Models," in *Coal and biomass gasification* , Singapur, Springer, 2020, pp. 223-241.

[58] S. I. Ngo, T. D.B.Nguyen and Y.-I. Lim., "Performance evaluation for dual circulating fluidized-bed steam gasifier of biomass using quasi-equilibrium three-stage gasification model," *Applied Energy,* vol. 88, no. 12, pp. 5208-5220, 2011.

[59] G. Mirmoshtaghi, H. Li, E. Thorin and E. Dahlquist, "Evaluation of different biomass gasification modeling approaches for fluidized bed gasifiers," *Biomass and Bioenergy,* vol. 91, pp. 69-82, 2016.

[60] S. Gupta, S. Bhaskaran and S. De, "Numerical Modelling of Fluidized Bed Gasification: An Overview," in *Coal and Biomass gasifciation Recent Advances and Future Challenges*, Singapur, Springer, 2018, pp. 243-280.

[61] H. Asadi-Saghandi, A. Sheikhi and R. Sotudeh-Gharebagh, "Sequence-based Process Modeling of Fluidized Bed Biomass Gasification," *Sustainable Chemistry and Engineering,* vol. 3, pp. 2640-2651, 2015.

[62] S. Behesti, H. Ghassemi and R. Shahsavan-Markadeh, "Process simulation of biomass gasification in a bubbling fluidized bed reactor," *Energy conversion and management ,* vol. 94, pp. 345-352, 2015.

[63] Th.Damartzis, S.Michailos and A.Zabaniotou, "Energetic assessment of a combined heat and power integrated biomass gasification–internal combustion engine system by using Aspen Plus," *Fuel Process Technology,* vol. 95, pp. 37-44, 2012.

[64] R. Toomey and H. Johnstone, "Gaseous fluidization of solid particles," *Chemical Engineering Progress ,* vol. 48, pp. 220-226, 1952.

[65] S. A. Khraibet, G. Mazloom and F. Banisharif, "Comparative Study of Different Two-Phase Models for the Propane Oxidative Dehydrogenation in a Bubbling Fluidized Bed Containing the VOx/γ-Al2O3 Catalyst," *Ind. Eng. Chem. Res,* vol. 60, pp. 9729-9738, 2021.

[66] M. Rafati, A. Hashemisohi and L. Wang, "Sequential Modular Simulation of Hydrodynamics and Reaction Kinetics in a Biomass Bubbling Fluidized-Bed Gasifier Using Aspen plus," *energy and fuels,* vol. 29, pp. 8261-8272, 2015.

[67] I. Kamal and Al-Malah, Aspen plus: chemical engineering applications, Hoboken: John Wiley and sons, 2017.

[68] S. Channiwala and P. Parikh, "A unified correlation for estimating HHV of solid, liquid and gaseous fuels," *Fuel,* vol. 81, pp. 1051-1063, 2002.

[69] S. Honus, S. Kumagaic and G. Fedorkod, "Pyrolysis gases produced from individual and mixed PE, PP, PS, PVC, and PET—Part I: Production and physical properties," *Fuel,* vol. 2221, pp. 346-360, 2018.

[70] Aspen Technology, aspen plus 11.1 user guide, Cambridge: Aspentech, 2001.

[71] A. Ramos, E. Monteirob and V. Silvac, "Co-gasification and recent developments on waste-to-energy conversion: A review," *Renewable and Sustainable Energy Reviews,* vol. 81, pp. 380-398, 2018.

[72] A. Gungor and N. Eskin, "Two dimensional coal combustion modeling of CFB," *International Journal of Thermal Sciences,* vol. 47, pp. 157-174, 2008.

[73] Q. Xiong, M. M. Yeganeh and E. Yaghoubi, "Parametric investigation on biomass gasification in a fluidized bed gasifier and conceptual design of gasifier," *Chemical Engineering & Processing: Process Intensification,* vol. 127, pp. 271-291, 2018.

[74] S. R. Horton, J. Woeckener and R. Mohr, "Molecular-Level Kinetic Modeling of the Gasification of Common Plastics," *Energy and fuels,* vol. 30, pp. 1662-1674, 2015.

[75] H. Zhou, C. Wub and J. A. Onwudili, "Polycyclic aromatic hydrocarbons (PAH) formation from the pyrolysis of different municipal solid waste fractions," *Waste Management,* vol. 36, pp. 136-146, 2015.

[76] X. Zhou, L. J. Broadbelt and R. Vinu, "Mechanistic understanding f thermochemical conversion of polymers and lignocellulosic biomass," in *Advances in Chemical Engineering Thermochemical Process Engineering* , Elsevier Science and Technology , 2016.

[77] W. Kaminsky, "Chemical Recycling of Mixed Plastics by Pyrolysis," *Advances in Polymer Technology,* pp. 337-344, 1995.

[78] Aspen tech, "Reaction in Fluidized Beds, Guide to the Fluidized Bed Reactor Demo," Aspen Technology, Burlington, Massachusetts, 2013.

[79] G.Löffler, S.Kaiser and K.Bosch, "Hydrodynamics of a dual fluidized-bed gasifier—Part I: simulation of a riser with gas injection and diffuser," *Chemical Engineering Science,* vol. 58, no. 18, pp. 4197-4213, 2003.

[80] C. Wen and Y. Yu, "A generalized method for predicting the minimum fluidization conditions," *AIChe Journal,* vol. 12, pp. 610-612, 1966.

[81] Q. Dang, X. Zhang, Y. Zhou and X. Jia, "Prediction and optimization of syngas production from a kinetic-based biomass gasification process model," *Fuel Processing Technology,* vol. 212, 2021.

[82] Q. Miao, J. Zhu and S. Barghi, "Modeling biomass gasification in circulating fluidized beds," *Renewable Energy,* vol. 50, pp. 665-661, 2013.

[83] J. H. Pauls, N. Mahinpey and E. Mostafavi, "Simulation of air-steam gasification of woody biomass in a bubbling fluidized bed using Aspen Plus: A comprehensive model including pyrolysis, hydrodynamics and tar production," *Biomass and Bionergy,* vol. 95, pp. 157-166, 2016.

[84] A. K.Stark, ChristosAltantzis, R. B.Bates and A. F.Ghoniemb, "Towards an advanced reactor network modeling framework for fluidized bed biomass gasification: Incorporating information from detailed CFD simulations," *Chemical Engineering Journal,* vol. 303, pp. 409-424, 2016.

[85] A. Eslami, A. H. Sohi and A. Sheikhi, "Sequential Modeling of Coal Volatile Combustion in Fluidized Bed Reactors," *Energy and fuels,* vol. 26, pp. 5199-5209, 2012.

[86] R. Porrazzo, G. White and R. Ocone, "Aspen Plus simulations of fluidised beds for chemical looping combustion," *Fuel,* vol. 136, pp. 46-56, 2014.

[87] S. Martınez-Lera, J. Torrico, J. Pallare and A. Gil, "Design and first experimental results of a bubbling fluidized bed for air gasification of plastic waste," *Material Cycles and Waste Management,* vol. 15, pp. 370-380, 2013.

[88] L. Zaccariello and M. L. Mastellone, "Fluidized-Bed Gasification of Plastic Waste, Wood, and Their Blends with Coal," *Energies,* vol. 8, pp. 8052-8068, 2015.

[89] L. Yan, C. J. Lim and G. Yue, "One-dimensional modeling of a dual fluidized bed for biomass steam gasification," *energy Conversion and Management,* vol. 127, pp. 612-622, 2016.

[90] B. Hejazi, J. R. Grace and X. Bi, "Kinetic Model of Steam Gasification of Biomass in a Bubbling Fluidized Bed Reactor," *energy and fuels,* vol. 31, pp. 1702-1711, 2017.

[91] S. Martínez-Lera and J. P. Ranz, "On the development of a polyolefin gasification modelling approach," *Fuel,* vol. 197, pp. 518-527, 2017.

[92] Y. Du, H. Liu and W. Ren, "Numerical Investigations of a Fluidized Bed Biomass Gasifier Coupling Detailed Tar Generation and Conversion Kinetics with Particle-Scale Hydrodynamics," *Energy and fuels,* vol. 34, pp. 8440-8451, 2020.

[93] G. Lopez, M. Artetxe and M. Amutio, "Recent advances in the gasification of waste plastics. A critical overview," *Renewable and Sustainable Energy Reviews,* vol. 82, pp. 576-596, 2018.

[94] O. C. Mutlu and T. Zeng, "Challenges and Opportunities of Modeling Biomass Gasification in Aspen Plus: a review," *Chemical Engieering & Technology,* vol. 43, no. 9, pp. 1674-1689, 2020.

[95] O. C. Mutlu and T. Zeng, "Challenges and Opportunities of Modeling Biomass Gasification in Aspen Plus: a review," *Chemical engineering and Technology,* vol. 43, no. 9, pp. 1674-1689, 2020.

8 Appendix

8.1 Types of reactor blocks in Aspen plus.

Table 28 Reactor blocks for equilibrium model in Aspen plus extracted from [67].

Block	Description	Use
RStoic	Stoichiometric reactor	• The stoichiometric is given. • The reaction kinetics is unknown/irrelevant
RYield	Yield reactor	• The stoichiometric and reaction kinetics are unknown/irrelevant. • The equilibrium composition is given.
RGibbs	Equilibrium reactor	• The stoichiometric and kinetics are not required as the model assumes the equilibrium composition is reached.

Table 29 Reactor blocks for the kinetic model in Aspen plus extracted from [67]

Block	Description	Use
CSTR	Kinetic reactor	• Modeling multiphase reactions considering presence of catalytic particles. The block solves the set of kinetic reactions at constant temperature or thermal duty. • The volume is defined by the user
PFR	Kinetic reactor	• Modeling gas phase reactions considering presence of catalytic reactions. The block solves the set of kinetic reactions at constant temperature or thermal duty (requiring of heat transfer data). • The diameter and length are defined by the user. Besides, the diameter of the block can vary along the length.
Fluidbed	Fluidized bed model	• Predefined block in Aspen plus to model the three sections of a fluidized bed reactor (dense bed, TDH and freeboard zones). • Requires of operation data, reactor geometry, and fluidization model.

8.2 Coefficients of the pyrolysis correlations.

Table 30 Coefficients of pyrolysis correlations for the reference PW mixture.

Polynomial Expression [a] $Y_i = AT^2+BT+C$					**Dry basis**
Family	Compound	A	B	C	Yi (%w)
Permanent Gases	H_2 [c]	4.30E-05	-5.86E-02	20.20	
	CO	-5.85E-05	8.59E-02	-29.82	
	CO_2	-1.37E-04	2.00E-01	-69.59	
	CH_4	2.12E-04	-1.96E-01	40.66	
Light HC	C_2H_6	-1.36E-04	1.99E-01	-69.60	
	C_2H_4	-6.81E-04	1.04E+00	-387.65	
	C_3H_8	-3.17E-05	4.42E-02	-14.95	
	C_3H_6	-3.17E-04	4.42E-01	-149.49	
	C_4H_{10}	5.52E-04	-8.70E-01	343.29	
	C_4H_8	-1.11E-04	1.60E-01	-56.54	
	C_5H_{10}	1.41E-03	-2.15E+00	818.82	
Single ring	C_6H_6	-6.12E-04	9.85E-01	-382.70	
	C_7H_8	1.49E-04	-1.85E-01	58.61	
	C_8H_8	-5.85E-04	7.98E-01	-261.54	
Double ring	$C_{10}H_8$	1.45E-04	-1.67E-01	48.31	
Triple ring	$C_{14}H_{10}$	8.71E-04	-1.38E+00	559.58	
	$C_{12}H_8$	-7.73E-04	1.10E+00	-387.92	
	Total				
Water [d]					
Ashes [e]					
Char [b]					
Nitrogen [e]					
Sulfur [e]					
Chlorine [e]					
Oxygen [f]					

Notes:

a) Valid pyrolysis temperature range: 680-790°C
b) Char is calculated as the difference of the carbon content in the ultimate analysis (Table 7) minus the carbon in the CHO compounds.
c) The total H_2 yield is calculated as the difference of the hydrogen content in the ultimate analysis (Table 7) minus the hydrogen in the CHO compounds. Later, the difference is added to the H_2 yield determined by the pyrolysis correlation.
d) The water content comes is equals to the moisture content at the inlet of the pyrolyser block.
e) Values from the ultimate analysis (Table 7).
f) The total O_2 yield is calculated as the difference of the oxygen content in the ultimate analysis (Table 7) minus the oxygen in the CHO compounds.

8.3 Kinetic expressions.

Table 31 Kinetic parameters of homogenous gasification reactions.

Rxn	Reactions	Rate Equation (kgmol/m³s)	α	β	γ	Ko (s⁻¹)	Ea (kJ/mol)
1 [56]	$H_2 + 0.5\,O_2 \rightarrow H_2O$	$R_{H_2} = Koexp\left(\frac{-Ea}{RT}\right) C_{H_2}^{\alpha} C_{O_2}^{\beta}$	1	1		2.2x10^{9}	109
2 [56]	$CO + 0.5\,O_2 \rightarrow CO_2$	$R_{CO} = Koexp\left(\frac{-Ea}{RT}\right) C_{CO}^{\alpha} C_{O_2}^{\beta} C_{H_2O}^{\gamma}$	1	0.25	0.5	2.32x10^{12}	167
3 [90]	$CH_4 + H_2O \rightarrow CO + 3\,H_2$	$R_{CH_4} = Koexp\left(\frac{-Ea}{RT}\right) C_{CH_4}^{\alpha} C_{H_2O}^{\beta}$	1	1		3.00x10^{2}	125
4 [73]	$CH_4 + 1.5\,O_2 \rightarrow CO + 2\,H_2O$	$R_{CH_4} = Koexp\left(\frac{-Ea}{RT}\right) C_{CH_4}^{\alpha} C_{O_2}^{\beta}$	0.7	0.8		1.59x10^{7}	200
6 [53]	$CO + H_2O \rightarrow CO_2 + H_2$	$R_{forward} = Koexp\left(\frac{-Ea}{RT}\right) C_{H_2O}^{\alpha} C_{CO}^{\alpha}$	1			5.2x10^{5}	102.4
7 [53]	$CO_2 + H_2 \rightarrow CO + H_2O$	$R_{reverse} = Koexp\left(\frac{-Ea}{RT}\right) C_{H_2}^{\alpha} C_{CO_2}^{\beta}$	0.5	1		1.2x10^{10}	318

Table 32 kinetic parameters for rate equations of heterogenous reactions, adapted from [90].

Rxn	Reaction	Rate Equation (kgmol/m³s)	α	Ko (s⁻¹)	Ea (kJ/mol)	Notes
1	$C + \left(\frac{\beta + 2}{2\,(\beta + 1)}\right) O_2 \rightarrow \left(\frac{\beta}{\beta + 1}\right) CO + \left(\frac{1}{\beta + 1}\right) CO_2$	$R_c = \frac{Ko}{T}\ exp\left(\frac{-Ea}{RT}\right)\ C_{O_2} C_C (Xc)^{\alpha}$ $\beta = K_1\ exp\left(\frac{-Ea_1}{RT}\right)$	1.2	Ko= 1.83x10^{7} K$_1$= 3x10^{8}	Ea=108.73 Ea$_1$= 250	Xc= FC from proximate analysis β =CO/ CO$_2$ ratio [82]
2	$C + H_2O \rightarrow CO + H_2$	$R_C = \frac{Ko}{T^{\alpha}} exp\left(\frac{-Ea}{RT}\right)\ C_{H_2O}^{\alpha}$	0.57	1.09x10^{9}	237	
3	$C + CO_2 \rightarrow 2\,CO$	$R_C = \frac{Ko}{T^{\alpha}}\ exp\left(\frac{-Ea}{RT}\right)\ C_{CO_2}^{\alpha}$	0.38	8.0189x10^{6}	215	
4	$C + 2H_2 \rightarrow CH_4$	$R_C = \frac{Ko}{T^{\alpha}}\ exp\left(\frac{-Ea}{RT}\right)\ C_{H_2}^{\alpha}$	0.93	1.4289x10^{3}	94.8	

Table 33 Kinetic parameters and reaction rates equations of light hydrocarbons and lumped tar compounds.

Tar compound	**Reactions**	**Rate Equation (kgmol/m^{3}s)**	**α**	**β**	**γ**	**Ko (s^{-1})**	**Ea (kJ/mol)**
Ethylene [91]	$C_2H_4 + 2\,O_2 \rightarrow 2\,CO + 2\,H_2O$	$R_{C_2H_4} = Ko\ exp\left(\frac{-Ea}{RT}\right)\ C^{\alpha}_{C_2H_4}C^{\beta}_{O_2}$	0.7	0.8		1.58×10^{10}	201.20
Propylene [91]	$C_3H_6 + 3\,O_2 \rightarrow 3\,CO + 3\,H_2O$	$R_{C_3H_6} = Ko\ exp\left(\frac{-Ea}{RT}\right)\ C^{\alpha}_{C_3H_6}C^{\beta}_{O_2}$	0.5	1.1		1.09×10^{10}	162.96
Butylene [91]	$C_4H_8 + 4\,O_2 \rightarrow 4\,CO + 4\,H_2O$	$R_{C_4H_8} = Ko\ exp\left(\frac{-Ea}{RT}\right)\ C^{\alpha}_{C_4H_8}C^{\beta}_{O_2}$	0.25	1.5		6.04×10^{9}	124.71
Butene a) [66]	$C_4H_{10} + 2\,O_2 \rightarrow 4\,CO + 5\,H_2$	$R_{C_4H_{10}} = KoT\ exp\left(\frac{-Ea}{RT}\right)\ C^{\alpha}_{C_4H_{10}}C^{\beta}_{O_2}$	0.5	1		2.73×10^{8}	164.5
Pentene a) [66]	$C_5H_{10} + 2.5\,O_2 \rightarrow 5\,CO + 5\,H_2$	$R_{C_5H_{10}} = KoT\ exp\left(\frac{-Ea}{RT}\right)\ C^{\alpha}_{C_5H_{10}}C^{\beta}_{O_2}$	0.5	1		2.48×10^{8}	164.5
Benzene [53]	$C_6H_6 + H_2O \rightarrow 3C + 2\,CH_4 + CO$	$R_{C_6H_6} = Ko\ exp\left(\frac{-Ea}{RT}\right)\ C^{\alpha}_{C_6H_6}C^{\beta}_{H_2}C^{\gamma}_{H_2O}$	1.3	-0.4	0.2	4×10^{16}	443
Benzene [38]	$C_6H_6 + 4.5\,O_2 \rightarrow 6\,CO + 3\,H_2O$	$R_{C_6H_6} = Ko\ exp\left(\frac{-Ea}{RT}\right)\ C^{\alpha}_{C_6H_6}C^{\beta}_{O_2}$	-0.1	1.85		2.4×10^{11}	125
Benzene [56]	$C_6H_6 + 7.5\,O_2 \rightarrow 6\,CO_2 + 3\,H_2O$	$R_{C_6H_6} = Ko\ exp\left(\frac{-Ea}{RT}\right)\ C^{\alpha}_{C_6H_6}C^{\beta}_{O_2}$	-0.1	1.85		9.55×10^{8}	125
Toluene [53]	$C_7H_8 + H_2 \rightarrow C_6H_6 + CH_4$	$R_{C_7H_8} = Ko\ exp\left(\frac{-Ea}{RT}\right)\ C^{\alpha}_{C_7H_8}C^{\beta}_{H_2}$	1	0.5		1.04×10^{12}	247
Toluene [38]	$C_7H_8 + 10.5\,H_2O \rightarrow 3.5\,CO + 3.5\,CO_2 + 14.5\,H_2$	$R_{C_7H_8} = Ko\ exp\left(\frac{-Ea}{RT}\right)\ C^{\alpha}_{C_7H_8}$	1			1.00×10^{8}	100
Toluene [62]	$3C_7H_8 + H_2 \rightarrow C_{10}H_8 + 3\,CH_4 + C_2H_6 + 6\,C$	$R_{C_7H_8} = Ko\ exp\left(\frac{-Ea}{RT}\right)\ C^{\alpha}_{C_7H_8}C^{\beta}_{H_2}$	1	0.5		3.3×10^{7}	247
Naphthalene [53]	$C_{10}H_8 \rightarrow 9C + \frac{1}{6}\,C_6H_6 + \frac{7}{2}H_2$	$R_{C_{10}H_8} = Ko\ exp\left(\frac{-Ea}{RT}\right)\ C^{\alpha}_{C_{10}H_8}C^{\beta}_{H_2}$	1.6	-0.5		3.4×10^{14}	350
Naphthalene [38]	$C_{10}H_8 +\ 5\,O_2 \rightarrow\ 10\,CO +\ 4\,H_2$	$R_{C_{10}H_8} = Ko\ exp\left(\frac{-Ea}{RT}\right)\ C^{\alpha}_{C_{10}H_8}C^{\beta}_{O_2}$	0.5	1		2.08×10^{9}	164.5
Naphthalene [66]	$C_{10}H_8 +\ 7\,O_2 \rightarrow\ 10\,CO +\ 4\,H_2O$	$R_{C_{10}H_8} = KoT\ exp\left(\frac{-Ea}{RT}\right)\ C^{\alpha}_{C_{10}H_8}C^{\beta}_{O_2}$	0.5	1		6.57×10^{5}	80.23
Naphthalene [62]	$C_{10}H_8 +\ 2\,H_2O \rightarrow 3\,CH_4 +\ 2\,CO +\ 5\,C$	$R_{C_{10}H_8} = Ko\ exp\left(\frac{-Ea}{RT}\right)\ C^{\alpha}_{C_{10}H_8}C^{\beta}_{H_2}$	1.6	-0.5		1.7×10^{11}	350

Notes:

a) Kinetic expressions adapted from equation (18).

8.4 Scripts for kinetic models.

8.4.1 Pyrolysis correlations

```
C SCRIPT TO CALCULATE THE PYROLYSIS COMPOSITION
C BASED ON KAMINSKY WORK
C SPECIFY VARIABLES TYPE
      REAL*8 YH2,YCO,YCO2,YCH4,YC2H6,YC2H4,YC3H8,YC3H6
      REAL*8 YC4H10,YC4H8,YC5H12
      REAL*8 YAB,YBEN,YTOL,YSTI,YNAP,YANT, YACE
      REAL*8 ASH, WAT, CARB,CHAR,N2,CL2,SULF,O2,TP
      REAL*8 MW1,MW2,MW3,MW4,MW5,MW6
      REAL*8 MW7,MW8,MW9,MW10,MW11,MW12,MW13,MW14,MW15
      REAL*8 MW16,MW17,MW18
      REAL*8 C,H,O
      REAL*8 RESC,RESH,RESO, PYRC, PYRH, PYRO
C MASS YIELD IN FUNCTION OF THE TEMPERATURE
C POLYNOMIALS EXPRESSION FORM AT^2+BT+C
      YH2 = ABS(4.2975E-05*TP**2 -5.8628E-02*TP +20.1954)
      YCO = ABS(-5.8512E-05*TP**2 +8.5904E-02*TP -29.8227)
      YCO2 = ABS(-1.3653E-04*TP**2 +2.0044E-01*TP -69.5862)
      YCH4 = ABS(2.1157E-04*TP**2 -1.9646E-01*TP +40.6646)
      YC2H6 = ABS(-1.3554E-04*TP**2 +1.9888E-01*TP -69.6033)
      YC2H4 = ABS(-6.8099E-04*TP**2 +1.0411*TP -387.6488)
      YC3H8 = ABS(-3.173E-05*TP**2 +4.416E-02*TP -14.9485)
      YC3H6 = ABS(-3.1736E-04*TP**2 +4.416E-01*TP -149.4851)
      YC4H10 = ABS(5.5207E-04*TP**2 -8.7026E-01*TP +343.2945)
      YC4H8 = ABS(-1.1074E-04*TP**2 +1.5961E-01*TP -56.5379)
      YC5H10 = ABS(1.4099E-03*TP**2 -2.1503*TP +818.8221)
      YBEN = ABS(-6.1157E-04*TP**2 +9.8501E-01*TP -382.6955)
      YTOL = ABS(1.4876E-04*TP**2 -1.8468E-01*TP +58.6140)
      YSTI = ABS(-5.8512E-04*TP**2 +7.9795E-01*TP -261.545)
      YNAP = ABS(1.4545E-04*TP**2 -1.6745E-01*TP +48.3109)
      YANT = ABS(8.7107E-04*TP**2 -1.3869*TP +559.5802)
      YACE = ABS(-7.7355E-04*TP**2 +1.1055*TP -387.9203)
C MOELCULAR WEIGHT OF CARBON, HYDROGEN AND OXYGEN
      C = 12.0107
      H = 1.0078
      O = 15.999
C DETERMINE THE MASS FRACTION PER ELEMENT NOTATION
C  YIJ WHERE I=1,2,3 ... 1=C 2=H 3=O. AND J=1,2,3,... COMPOUND ID
      Y11 = 0*YH2
      Y21 = (2*H/MW1)*YH2
      Y31 = 0*YH2
      Y12 = (C/MW2)*YCO
      Y22 = 0*YCO
      Y32 = (O/MW2)*YCO
      Y13 = (C/MW3)*YCO2
```

```
      Y23 = 0*YCO2
      Y33 = (2*O/MW3)*YCO2
      Y14 = (C/MW4)*YCH4
      Y24 = (4*H/MW4)*YCH4
      Y34 = 0*YCH4
      Y15 = (2*C/MW5)*YC2H6
      Y25 = (6*H/MW5)*YC2H6
      Y35 = 0*YC2H6
      Y16 = (2*C/MW6)*YC2H4
      Y26 = (4*H/MW6)*YC2H4
      Y36 = 0*YC2H4
      Y17 = (3*C/MW7)*YC3H8
      Y27 = (8*H/MW7)*YC3H8
      Y37 = 0*YC3H8
      Y18 = (3*C/MW8)*YC3H6
      Y28 = (6*H/MW8)*YC3H6
      Y38 = 0*YC3H6
      Y19 = (4*C/MW9)*YC4H10
      Y29 = (10*H/MW9)*YC4H10
      Y39 = 0*YC4H10
      Y110 = (4*C/MW10)*YC4H8
      Y210 = (8*H/MW10)*YC4H8
      Y310 = 0*YC4H8
      Y111 = (5*C/MW11)*YC5H10
      Y211 = (10*H/MW11)*YC5H10
      Y311 = 0*YC5H10
      Y113 = (6*C/MW13)*YBEN
      Y213 = (6*H/MW13)*YBEN
      Y313 = 0*YBEN
      Y114 = (7*C/MW14)*YTOL
      Y214 = (8*H/MW14)*YTOL
      Y314 = 0*YTOL
      Y115 = (8*C/MW15)*YSTI
      Y215 = (8*H/MW15)*YSTI
      Y315 = 0*YSTI
      Y116 = (10*C/MW16)*YNAP
      Y216 = (8*H/MW16)*YNAP
      Y316 = 0*YNAP
      Y117 = (14*C/MW17)*YANT
      Y217 = (10*H/MW17)*YANT
      Y317 = 0*YANT
      Y118 = (12*C/MW18)*YACE
      Y218 = (8*H/MW18)*YACE
      Y318 = 0*YACE
C SUM THE MASS FRACTIONS OF CARBON (C), HYDROGEN (H), OXYGEN (O)
      PYRC=Y11 +Y12 +Y13 +Y14 +Y15 +Y16 +Y17 +Y18 +Y19 +Y110 +
     +Y111 +Y113 +Y114 +Y115 +Y116 +Y117 +Y118
```

```
      PYRH = Y21 +Y22 +Y23 +Y24 +Y25 +Y26 +Y27 +Y28 +Y29 +Y210 +
     +Y211 +Y213 +Y214 +Y215 +Y216 +Y217 +Y218
      PYRO = Y31 +Y32 +Y33 +Y34 +Y35 +Y36 +Y37 +Y38 +Y39 +Y310 +
     +Y311 +Y313 +Y314 +Y315 +Y316 +Y317 +Y318
C IMPORT THE DATA FROM THE ULTIMATE ANALYSIS.
C UNITS ARE IN MASS PERCENTAGE
      YH2O = WAT
      ASH = ULT(1)
      CARB = ULT(2)
      H2 = ULT(3)
      YN2 = ULT(4)
      YCL2 = ULT(5)
      YSULF = ULT(6)
      O2 = ULT(7)
C MAKE THE CORRECTIONS FOR FREE CARBON WHICH BECOMES CHAR
C THE HYDROGEN AND OXYGEN ARE CONSIDER AS H2 AND O2 RESPECTIVELY
      RESH = H2 - PYRH
      YHYDRO = YH2 + RESH
      RESO = O2 - PYRO
      IF (O2 .GT. PYRO) THEN
          YO2 = RESO
          CHAR = CARB - PYRC
      ELSE IF (PYRO .GT. O2) THEN
          YO2 = O2
          YCO = 0
          YCO2 = 0
          CHAR = CARB - PYRC + Y12 + Y13
      END IF
```

8.4.2 Hydrodynamic models

```
C CALCULATE THE BED HYDRODYNAMICS IN 1-D
C USING A CALCULATOR BLOCK FOR THE FLUIDBED, CSTRS-PFR ABD TPM MODEL
C BASED ON THE WORK DEVELOPED BY BEHESHTI ET GHASSEMI FOR BED EXPANSION
C AND BY RATI ET AL FOR THE TWO-PHASE CORRELATIONS.
C 1) DEFINE VARIABLES BED ZONE,
      REAL*8 MG, RHOG, RHOP, VR, MBED
      REAL*8 MUG, VGAS, REMF, AR
      REAL*8 EPMF, EPB, EPF, DP, AG, G, DB
      REAL*8 UT, MUGEXP, DPEXP, VAL, REMF, UMF, UBR, UB, UE
      REAL*8 BN, BD, B, EPMF, EPB, EPE, EPF
      REAL*8 HMF, HBED, VR, VGAS, VCSTR, VPFR
C 1) DEFINE VARIABLES BED ZONE
C AG, CROSS SECTIONAL AREA OF THE GASIFIER (M2)
C MG, MASS FLOW GASIFYING AGENT (KG/S)
C MUG, GAS VISCOSITY FROM GASIFYING AGENT (KG/M/S)
C RHOG, GAS DENSITY OF THE GASIFYING AGENT (KG/M3)
C RHOP, PARTICLE DENSITY IMPORT FROM ASPEN PLUS (KG/M3)
```

```
C MBED, LOAD OF BED PARTICLES (KG)
C 2)CALCULATE THE SUPERFICIAL VELOCTIY OF THE GASIFYING AGENT
      UT = MG/(AG*RHOG)
C 3)ARCHIMEDES NUMBER IS THE RATIO OF GRAVITATIONAL TO VISCOUS
C FORCES
      MUGEXP = MUG**2.
      DPEXP = DP**3.
      AR = G*(DPEXP)*RHOG*(RHOP-RHOG)/(MUGEXP)
      VAL = (33.7**2.) + 0.0408*AR
      REMF = (VAL)**0.5 - 33.7
C 5) CALCULATE MINIMUM FLUIDIZATION VELOCITY UMF
      UMF = (REMF*MUG)/(DP*RHOG)
```

END OF THE
FLUIDBED MODEL

```
C 6) BED EXPANSION COEFFICIENT (B)
      BN = 14.314*((UT - UMF)**0.738)*(DP**1.006)*(RHOP**0.376)
      BD = (RHOG**0.126)*(UMF**0.937)
      B = 1 + BN/BD
C 8) ESTIMATE BED VOIDAGE AT MINIMUM FLUDIZATION CONDITIONS
      EPMF = 0.48/(AR**0.018)
C 8) VOLUME FRACTION OF BED OCCUPIED BY BUBBLE EPB
C      EPB = 1 - 1/B
C 9) BED VOID FRACTION
C      EPF = EPB + (1-EPB)*EPMF
C 10) MINIMUM HEIGHT HMF
      HMF = MBED/(AG*(1-EPMF)*(RHOP-RHOG))
C 11) CALCULATE BED HEIGHT
      HBED = B*HMF
C 12) REACTOR VOLUME
      VR = HBED*AG
C 13) GAS PHASE VOLUME
C      VGAS = EPF*VR
```

END OF THE
CSTRS-PFR MODEL

```
C 14) number of pairs
C      NP = 1
C 15) Volume per pair
C      VP = VR/NP
C 16) bubble diameter
      ARG = (-0.25*(UT-UMF)**2)-0.1*(UT-UMF)
      DB = 0.21*(HBED**0.8)*((UT-UMF)**0.42)*EXP(ARG)
C 17) Calculate bubble rise velocity
      UBR = 0.711*(G*DB)**0.5
C 20) EMULSION VELOCITY
      UE = UMF/EPMF
C 18) BUBBLE VELOCITY
      UB = UT - UE + UBR
C 19) BUBBLE PHASE VOIDAGE
      EPB = 1-0.146*EXP(-(UT-UMF)/4.439)
```

```
C 21) EMULSION PHASE VOIDAGE
      EPE = EPMF +0.2-0.059*EXP(-(UT-UMF)/0.429)
C 22) CALCULATE THE BED VOIDAGE
      SIG = 0.534-0.534*exp*((UT-UMF)/0.413)
      EPF = SIG*EPB+(1-SIG)*EPE
C 23) BUBBLE PHASE VOLUME
      VBB = VR*SIG
C 25) VOLUME OF PFR BLOCK
      VPFR = VBB
      VBG = VPFR*EPB
      APFR = VPFR/HBED
      DPFR = (4*APFR/3.1416)**0.5
C 24) VOLUME OF THE CSTR BLOCK
      VCSTR = VR*(1-SIG)
      ACSTR = VCSTR/HBED
C 26) VOLUME OF THE EMULSION PHASE
      VEM = VCSTR*EPE
```

END OF THE TPM

8.4.3 Mass Transfer conditional

```
C SCRIPT TO CALCULATE THE MASS TRANSFER COEFFICIENT BASED
C ON RAFITI WORK
C MASS TRANSFER COEFFICIENT
      DBE = (DBE1+DBE2)/2
C CALCULATE THE MASS TRANSFER COEFFICIENT BUBBLE-CLOUD
      KBC = 4.5*(UE/DB)+5.85*((DBE**0.5)*(G**0.25)/DB**1.25)
C CALCULATE THE MASS TRANSFER COEFFICIENT CLOUD-EMULSION
      KCE = 6.77*((DBE*EPE*UB)/DB**3.)**0.5
C CALCULATE THE MASS TRANSFER COEFFICIENT BUBBLE-EMULSION
      KBE = 1/((1/KBC)+(1/KCE))
C CONDITIONAL FOR SPLIT FRACTION
C H2
       IF (F1BO .GT. F1EO) THEN
        DIF1 = (F1BO-F1EO)/F1BO
        SF1B = DIF1/2
        SF1E = 0
      ELSE IF (F1EO .GT. F1BO) THEN
        DIF1 = (F1EO-F1BO)/F1EO
        SF1B = 0
        SF1E = DIF1/2
      END IF
      END IF
C THE CONDITION IS APPLIED FOR EVERY COMPOUND
```

8.5 Redistribution of the reaction packages in the validation cases.

Table 34. Distribution of the reaction packages in the kinetic models CSTRs-PFR and TPM for the validation case 1. Green cells indicate the reaction package enabled in each block.

Configuration	**Heterogenous reactions**	**CO comb**	**Homogenous reactions**	**WGS**	**LHC (C2-C5)**	**MAH (C6-C8)**	**PAH (C10)**
CSTRs-PFR							
CSTR 1	🟩	🟩	🟩	🟩			
CSTR 2	🟩	🟩	🟩	🟩			
CSTR 3	🟩	🟩	🟩	🟩	🟩		
CSTR 4	🟩	🟩	🟩	🟩	🟩		
CSTR 5	🟩	🟩	🟩	🟩	🟩		
CSTR 6	🟩	🟩	🟩	🟩	🟩	🟩	
CSTR 7	🟩	🟩	🟩	🟩	🟩	🟩	🟩
CSTR 8	🟩	🟩	🟩	🟩	🟩	🟩	🟩
CSTR 9	🟩	🟩	🟩	🟩	🟩	🟩	🟩
CSTR 10	🟩	🟩	🟩	🟩	🟩	🟩	🟩
PFR freeboard	🟩	🟩	🟩	🟩	🟩	🟩	🟩
TPM							
CSTR 1 emulsion	🟩		🟩	🟩			
PFR 1 bubble		🟩	🟩	🟩	🟩	🟩	🟩
CSTR 2 emulsion	🟩		🟩	🟩	🟩		
PFR 2 bubble		🟩	🟩	🟩	🟩	🟩	🟩
CSTR 3 emulsion	🟩		🟩	🟩	🟩	🟩	🟩
PFR 3 bubble		🟩	🟩	🟩	🟩	🟩	🟩
CSTR 4 emulsion	🟩		🟩	🟩	🟩	🟩	🟩
PFR 4 bubble		🟩	🟩	🟩	🟩	🟩	🟩
PFR freeboard		🟩	🟩	🟩	🟩	🟩	🟩

Table 35. Distribution of the reaction packages in the kinetic models CSTRs-PFR and TPM in the validation case 2. Green cells indicate the reaction package enabled in each block.

Configuration	**Heterogenous reactions**	**CO comb**	**Homogenous reactions**	**WGS**	**LHC (C2-C5)**	**MAH (C6-C8)**	**PAH (C10)**
	CSTR-PFR model						
CSTR 1	🟩	🟩	🟩	🟩	🟩		
CSTR 2	🟩	🟩	🟩	🟩	🟩		
CSTR 3	🟩	🟩	🟩	🟩	🟩	🟩	
CSTR 4	🟩	🟩	🟩	🟩	🟩	🟩	
CSTR 5	🟩	🟩	🟩	🟩	🟩	🟩	
CSTR 6	🟩	🟩	🟩	🟩	🟩	🟩	🟩
CSTR 7	🟩	🟩	🟩	🟩	🟩	🟩	🟩
CSTR 8	🟩	🟩	🟩	🟩	🟩	🟩	🟩
CSTR 9	🟩	🟩	🟩	🟩	🟩	🟩	🟩
CSTR 10	🟩	🟩	🟩	🟩	🟩	🟩	🟩
PFR freeboard	🟩	🟩	🟩	🟩	🟩	🟩	🟩
	TPM						
CSTR 1 emulsion	🟩		🟩	🟩			
PFR 1 bubble		🟩	🟩	🟩	🟩	🟩	🟩
CSTR 2 emulsion	🟩		🟩	🟩	🟩		
PFR 2 bubble		🟩	🟩	🟩	🟩	🟩	🟩
CSTR 3 emulsion	🟩		🟩	🟩	🟩	🟩	🟩
PFR 3 bubble		🟩	🟩	🟩	🟩	🟩	🟩
CSTR 4 emulsion	🟩		🟩	🟩	🟩	🟩	🟩
PFR 4 bubble		🟩	🟩	🟩	🟩	🟩	🟩
PFR freeboard		🟩	🟩	🟩	🟩	🟩	🟩